Measuring the Pion Substructure with Radiative Positronic Pion Decays
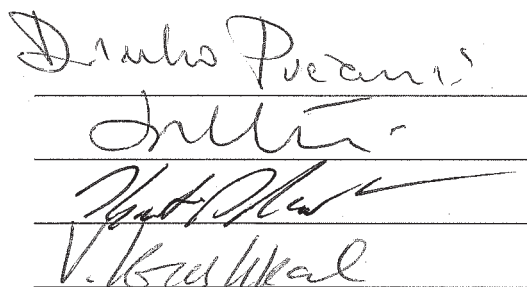
Loreto Peter Alonzi III
Wilmette, IL

B.S., The College of William & Mary in Virginia, 2005
M.A., The University of Virginia, 2007

A Dissertation presented to the Graduate Faculty
of the University of Virginia in Candidacy for the Degree of
Doctor of Philosophy

Department of Physics

University of Virginia
May, 2012

Abstract

This dissertation presents an analysis of the PEN data from 2008 searching for the rare decay $\pi^+ \rightarrow e^+ \nu \gamma$. The region of phase space was $E_\gamma > 10\,\text{MeV}$ and an opening angle of $\theta_{e\gamma} > 40°$. The goal was to measure the form factors of the pion, F_A and F_V. From an observation of 3,884 events we evaluated values of $F_A = 0.0193 \pm 0.008$ and $F_V = 0.0191 \pm 0.008$. For historical comparison the value of $\gamma \equiv F_A/F_V$ was also calculated assuming the Conserved Vector Current hypothesis from the standard model. That produced a result of $\gamma = 0.459 \pm 0.057$. Both of these results agree with the world experimental average and the standard model within $1\,\sigma$. The analysis procedure is described in this dissertation along with an in depth treatment of the simulation software produced for the determination of the system acceptance.

Contents

List of Figures

List of Tables

Acknowledgements

First I want to thank my dear friend Anthony Palladino. No one has spent more time setting me straight about the PEN experiment. I can say with absolute certainty I would not have been able to do the work that I did without him. The PEN collaboration also had several members to whom I am forever grateful. They are our co-spokesmen Dinko Počanić and Andries van der Schaaf. Many thanks to Max Bychkov for all the late night help and Emil Frlež for all the early morning discussions. I also had the pleasure of working with Martin Lehman as he joined our team. I wish I had spent more time with Martin but I am confident that he will continue to do great work for our collaboration. There are several experts on our team that I want to thank: Peter Robmann, Kolya Khomutov, Vladimir Baranov, and Tadek Kozlowski. Many thanks to Willi Bertl; our discussions on the topic of MWPC simulation were invaluable. I also want to thank the members of my dissertation committee: Dinko Počanić, Kent Paschke, Simonetta Liuti, and Slava Krushkal.

Finally I want to thank all of my friends and family. I am fortunate to have so many that I cannot list everyone here. So I will simply say, in the words of Bilbo (more or less): I wish I had spent more time with you, and you all mean more to me than I ever let on.

Chapter 1

The Theory of Pion Decay

At an altitude of 9,100 m in the autumn of 1946 an RAF plane soared through the sky carrying a scientific payload. The mission was to record microscopic tracks in photographic emulsions left behind by cosmic rays. The motivation for this endeavor came from work by Yukawa predicting a massive and short lived particle which mediated the nuclear binding force [10]. Unlike elementary particles already discovered[1], this new particle must be short lived. It would have to be observed mere billionths of a second after creation. Hopefully the cosmic rays would interact with the atmosphere of the earth producing these previously unseen particles. Fortunately the theories were correct and the mission succeeded, and as with most scientific endeavors more questions arose. New emulsions were prepared and carried to mountain tops in the Pyrenees and the Andes. As the data sample grew the results started to fit together like puzzle pieces. These discoveries were so exciting that Nobel Laureate Cecil Powell[2] reflected, "It was as if, suddenly, we had broken into a walled orchard, where protected trees flourished and all kinds of exotic fruits had ripened into great profusion"[11].

The emulsions showed direct evidence of this particle which today we call the pion

---

[1]Electrons (1897), protons (1919), and the photon (1900-1914).
[2]1950: For development of the emulsions and study of the mesons capture therein.

(π). Early measurements of the pion mass were $125\,\mathrm{MeV}/c^2$ with an average decay time of about $10^{-8}\,\mathrm{s}$ [12][3]. This decay time was much longer than expected; all previously observed interactions between sub-atomic particles occurred more than one billion times faster. The time scale of these phenomena indicated the presence of a previously unseen fundamental interaction responsible for the decay of the pion. Experimentalists and theorists jumped at the problem.

Finally a breakthrough occured with a magnificent paper published in 1958. Richard Feynman and Murray Gell-Mann worked out in beautiful detail the consequences of the so-called Fermi interaction for the pion [13]. At the time their results contradicted experiments leading them to remark, "The authors have no idea on how it can be resolved." Further experimentation was the answer. New accelerators produced pions en masse. These intense beams enabled precision measurements and experimentally the interaction could be studied. The results of these experiments showed that Feynman and Gell-Mann were correct, and the theory is now known as the Weak Force and that the fundamental nature was $V - A$[4].

Today the importance of the pion is as great as when it was first discovered. Measuring rare decay modes of the pion tests some of the most precise theoretical predictions of the weak force in the standard model [14]. Precision measurement of this sector is critical. Testing the model constrains new physics and gives clues to what physics exist as higher and higher energy scales. Two collaborations, PIENU and PEN[5], exist to continue the study of pion decay. They have undertaken the most sensitive tests of lepton universality to date. The results from these experiments are crucial to confirming or extending the standard model.

---

[3]Today we know these values to be about $139\,\mathrm{MeV}/c^2$ and $26\,\mathrm{ns}$. Additionally it should be noted that all figures regarding characteristics of particles are taken from the Particle Data Group unless otherwise specified (http://pdg.lbl.gov/).

[4]Much, much, much more to come on this topic.

[5]The work covered in this dissertation was conduced as part of the PEN experiment program.

1.1   Phenomenology of the Pion

The pion is a composite object consisting of two quarks[6]. For the purposes of this work the quarks are point-like particles and indivisible, what the ancient Greeks would call *atoms*. What binds them together to form the pion? Why can this binding only keep the pion together for a few nanoseconds? The standard model answers these questions by stating that particles interact fundamentally via a quantum explination in one of three ways. There is also the additional interaction of gravity that is negligible on the scale of this experiment. If the behavior of the pion cannot be explained through these three forces then new physics has been discovered. Figure 1.1 shows a cartoon of the pion. This picture contains an up (u) and an anti-down ($\bar{\mathrm{d}}$) quark. Together they are known as the π^+, represented by the grey circle[7]. The connectors between the two quarks represents the fundamental interactions between the quarks. The next subsections describe the behavior of each interaction in the standard model.

1.1.1   Electric Charge

The π^+ possesses one unit of the electric charge. The up and anti-down quark constituents of the pion carry $+2/3$ and $+1/3$ units of the fundamental electric charge. Both constituent quarks have electric charge and therefore interact through the electromagnetic force. Charges of same sign repel, therefore electromagentic interactions cannot explain the binding of the quarks. It is also not responsible for the decay of the chared pions. The observed final state of a pion decay includes a lone neutrino. The neutrino (ν) is elusive because it lacks electric charge. The electromagnetic force only

---

[6]This statement is made as if it were fact, but of course it is just our best theory. Some may also wish the word "valence" to be used in describing the quarks. However I would point out that distinction is not germane to the description necessary at this time.

[7]Theoretically the decay of the π^- is identical to that of the π^+ but that matter will not be addressed here. Additionally there is a third sibling, the π^0.
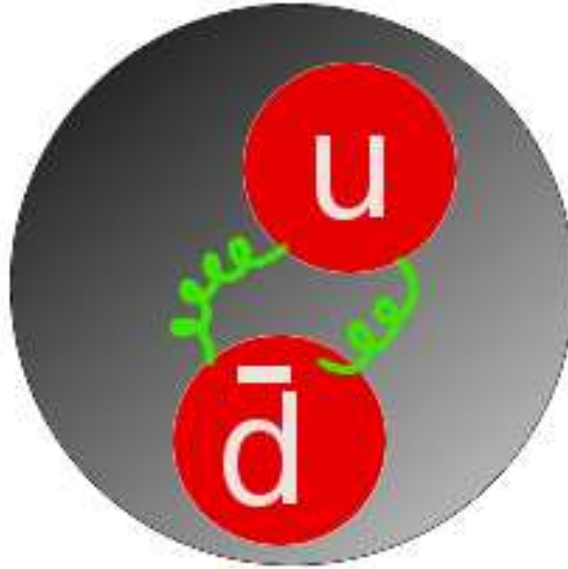
Figure 1.1: A cartoon of the π^+.

interacts with particles that have charge, therefore it cannot mediate the interaction which produces the neutrino and ultimately cannot explain the disintegration of the pion.

However the electromagnetic force is still useful in studying the pion. Hadrons have a substructure and to probe that structure the electromagnetic force is the best tool for the job. The components of the pion have electric charge, therefore when the pion decays it can emit a photon. While this photon is not responsible for the disintegration of the pion it can give insight into the spatial organization of the pion's charged constituents. Decays of this type are called radiative and their study leads to form factors of the pion, called F_V and F_A. The dominant force in the structure of the pion is the force responsible for the binding.

1.1.2   Color Charge

The quarks posses another kind of charge given the whimsical name *color*. Unlike the electric charge which comes in one flavor color charge comes in three flavors[8]. Only two kinds of particles carry this charge, quarks and gluons. The gluons themselves mediate the color interaction and their possession of the color charge makes the force behave in a way much different from all other forces. When a quark emits a gluon it is entirely possible for the gluon to couple to another gluon and so on, producing a web. If two quarks are far apart this gluon web will grow and in fact strengthen as the distance increases. Eventually this force will become so large that the quarks cannot be separated [15]. The result is that no quark can exists in isolation[9]; this property is called color confinement. All combinations of quarks must be colorless hence the quark anti-quark state of the pion. Whatever color charge is carried by the u quark is precisely canceled by the $\bar{\text{d}}$ quark and they remain bound in the pion.

This color web complicates the theoretical description of the pion. The inner workings are not just two quarks but rather an entire sea of gluons and quarks popping into and out of existence. This sea makes a absolute theoretical description of the pion intractable. Instead all of the complications of this structure are combined into several parameters: f_π, F_V, and F_A.

1.1.3   Left-Handed Charge

The remaining fundamental charge in the standard model is the weak charge. The behavior of this force is dominated by the unique nature of its mediating particles, the $W^\pm$ and Z^0 bosons. Both are massive (about 100 times greater than the proton). Such a large mass severely limits the range of the force, hence the name weak force[10]. Addition-

---

[8]Traditionally red, green, and blue with the combination of all three being colorless or white.

[9]Please permit some liberty with respect to the top quark.

[10]In fact this feature is reason for the slow time signature alluded to earlier.

ally the W is a charged particle which allows many processes forbidden with the neutral mediators. Finally the weak force only couples to particles in certain spatial states. This behavior is remarkable and was completely unexpected by the physics community [16] [17]. The symmetry concerned is called *parity* and is represented by a complete spatial inversion[11]. Furthermore certain symmetries present in the formulation of the electromagnetic and the color force are not present it the weak force. The weak interaction can transmute quarks from one flavor to another [18] [19]. The ability to transmute quarks directly explains the disintegration of the pion. A rotation of the quark transmutation diagram produces the quark annihilation diagram. However, unlike Bhabha interactions, the annihilation takes place not with a particle and it's anti-particle, but rather two different quarks. In the case of the pion the weak force annihilates the quarks into a W boson.

Figure 1.2 shows a Feynman diagram of a pion decay with time flowing from left to right. At the beginning a pion (π^+) transforms into a W boson (W^+), the mediator of the weak interaction. The shaded region includes the gluon web (f_π) which obfuscates the underlying weak process ($\pi \to W$). The W is virtual and rapidly decays into a charged lepton (l^+) and its associated neutrino (ν_l). There are several candidates for the role of l and subsequently the decay rate for each channel will be shown.

1.2 Theoretical Predictions

1.2.1 Fundamental Symmetries and Conservation Laws

A key tool for physicists is writing an equation that describes the energy of a system. The reason this approach is so bountiful relies on a theorem proved about 100 years ago at the time of writing [20]. The fundamental idea as it applies to physics is that

---

[11]x↔-x, y↔-y, z↔-z
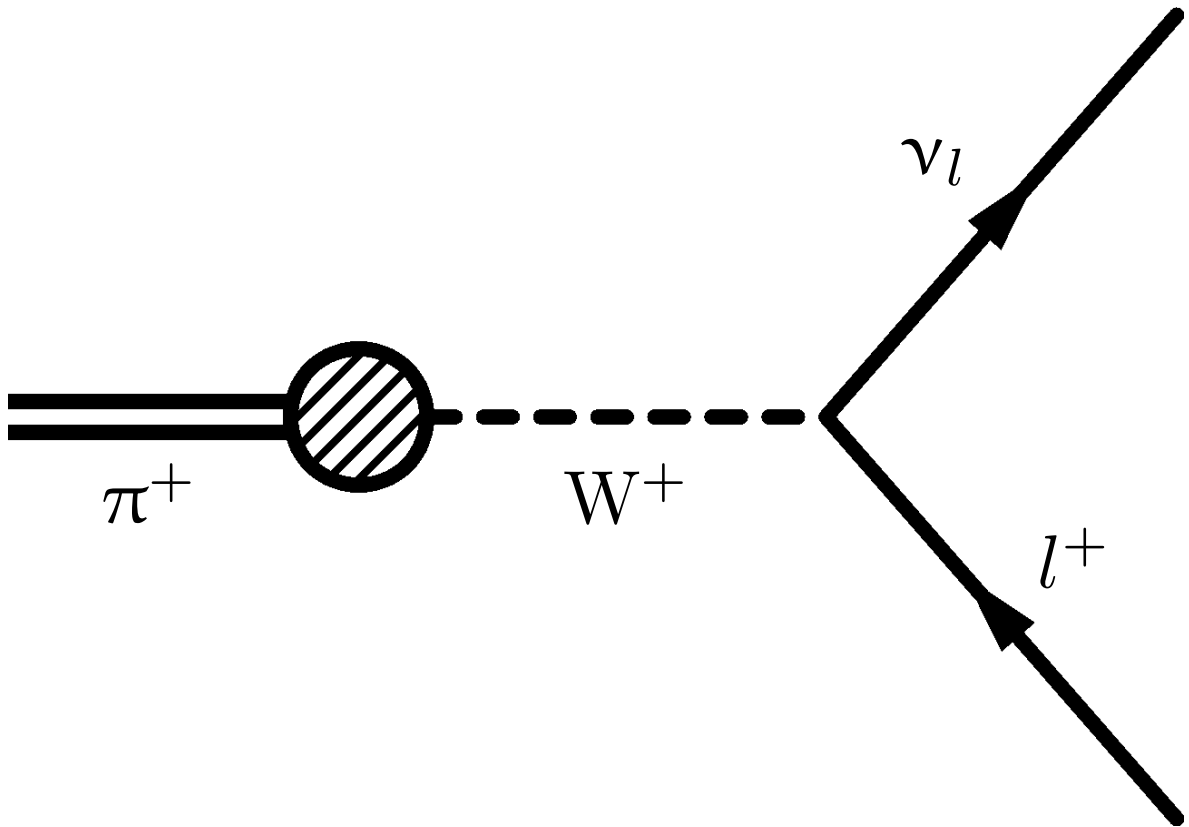
Figure 1.2: A Feynman diagram depicting the tree level decay of a pion.

symmetries present in the system correspond to conserved quantities. Common examples are conservation of energy and momentum. They are represented by the energy equation lacking a reference to absolute time (energy) or absolute position (momentum). In the case of the electric charge the symmetry is more subtle.

The equation of energy for the electromagnetic force, which we call the Lagrangian density is given by (1.1). Stripped down to the pieces relevant for our examination if reads:

$$\mathcal{L}_{QED} = \bar{\psi}(i\gamma^{\mu}D_{\mu} - m)\psi - \frac{1}{4}F_{\mu\nu}F^{\mu\nu}. \tag{1.1}$$

The wave-functions of our particles are represented as ψ, γ represents the Dirac matrices, D is the gauge covariant derivative ($D_{\mu} \equiv \partial_{\mu} - ieA_{\mu}$), m is the mass of the

particle, and F is the electromagnetic field tensor. We have the symmetries mentioned earlier, producing energy and momentum conservation, but in addition more symmetries are hidden in this equation. The understanding of ψ in quantum mechanics comes from the probabilistic nature of the theory. In fact ψ is not the final description of the state of the particle but rather $|\psi|^2$ is. Mathematically this relation means that ψ can vary by an overall phase (choice of gauge) and leave the final observable unchanged. Physically this behavior has great ramifications. The conserved quantity associated with the gauge degree of freedom is called electric charge! Therefore all interactions based on this Lagrangian cannot cause net electric charge to be created or destroyed.

The next force we will examine is the strong nuclear force governed by the following Lagrangian:

$$\mathcal{L}_{QCD} = \bar{\psi}(i\gamma^\mu D_\mu - m)\psi - \frac{1}{4}G^a_{\mu\nu}G^{\mu\nu}_a. \tag{1.2}$$

The equation is similar to that of QED but with the replacement of $F \rightarrow G$, the exchange of the photon for the gluon. The derivative also changes to $D_\mu \equiv \partial_\mu + igT_aG^a_\mu$. Additionally extra indices are included on the spinors and the derivative and tensors. These indices take into account the SU(3) nature of QCD and that there are 3 fundamental charges instead of one (as mentioned in Section 1.1). The structure of the tensor term is different because the mediators of the strong force (gluons) can interact with each other. This time the local gaugue basis of the theory leads to a conservation of color charge. Even more remarkable is the additional feature known as asymptotic freedom, that bizarre behavior of the strong force which states the strength of the force grows with distance[12]. These properties produce the behavior known as color confinement and explain why the pion remains in a bound quark anti-quark state.

Now we incorporate the weak force in our theory and look at the decay of the π^+. The

---

[12]What earlier was called the "gluon web".

Lagrangian enforces conservation of energy, therefore we are limited to decay products that are less massive then the pion itself[13].

Table 1.1: Elementary Particles Less massive than the π^+

Particle	Mass (MeV)	EM Charge
π^+	139.57	1
e^+	0.51099	1
ν_e	~ 0	0
μ^+	105.65	1
ν_μ	~ 0	0
ν_τ	~ 0	0
γ	0	0
g	0	0

Searching Table 1.2.1 for particles with charge we realize the final state must contain either a positron (e^+) or a muon (μ^+)[14]. Therefore we arrive at the intermediate solutions:

$$\pi^+ \rightarrow \mu^+ + \text{???} \qquad \text{or} \qquad \pi^+ \rightarrow e^+ + \text{???}. \tag{1.3}$$

Interactions of these kinds are forbidden for the electromagnetic and strong forces. There are many different explanations for why these are forbidden, since we have already established electric charge conservation let's use that law. Recall from Figure 1.2 that the mediator of the decay process must be charged. Table 1.2.1 shows that the gluon and photon have no charge therefore the process is forbidden for all forces except the weak force. So it is time to look at the weak Lagrangian in detail.

$$\mathcal{L}_{weak} = -\frac{g}{\sqrt{2}} \left[\bar{u}_i \gamma^\mu \frac{1-\gamma^5}{2} M_{ij}^{\text{CKM}} d_j + \bar{\nu}_{li} \gamma^\mu \frac{1-\gamma^5}{2} l_i \right] W_\mu^+. \tag{1.4}$$

In (1.4) g represents the strength of the interaction, the γ^i are the Dirac matrices[15], M

---

[13]The pion is the lightest of the hadrons so no quarks have been included in Table 1.2.1.

[14]Additionally we could add on final state electron-positron pairs or photons but for the moment we are constructing the most basic process.

[15]In particular γ^5 plays a special role and will be elaborated on in the upcoming section.

is the quark weak mixing matrix, W is a mediator particle of the weak force, and u, d, ν, and l are the familiar particles from Table 1.2.1. The second term shows us that we must balance the lepton l with an associated neutrino. Therefore we arrive at the final state solution of:

$$\pi^+ \to \mu^+ + \nu_\mu \qquad \text{or} \qquad \pi^+ \to e^+ + \nu_e. \tag{1.5}$$

However this correspondence of neutrinos to massive leptons is not essential for the theory. We could include terms in the theory that couple electrons to muon neutrinos but evidence of this process has never been observed. Such an observation of lepton flavor violation would be remarkable and indicate some exciting physics beyond the standard model.

1.2.2 Decay Rate

Let's now carry out the calculation of the decay rate of the pion. We start with a standard formulation for decay rate (Γ) given by (1.6) in differential form.

$$d\Gamma = \frac{1}{2m_\pi}\overline{|\mathcal{M}|^2}\frac{d^3p}{(2\pi)^3 2E}\frac{d^3k}{(2\pi)^3 2\omega}(2\pi)^4\delta(q-p-k). \tag{1.6}$$

Where m_π is the mass of the pion, $\mathcal{M}$ represents the fundamental physical interaction matrix element, k, p, and q are the momenta described in Figure 1.2, with E and ω representing the energies of the associated particles.

The momentum-based differentials suggest a larger decay rate for the electron because it is much less massive than the muon and therefore there is a much larger phase space for the decay process. The physics of the problem is contained in $\mathcal{M}$, which is also known colloquiually as the matrix element. This term represents the probability for different physics interactions. In fact the Feynman diagrams represented earlier
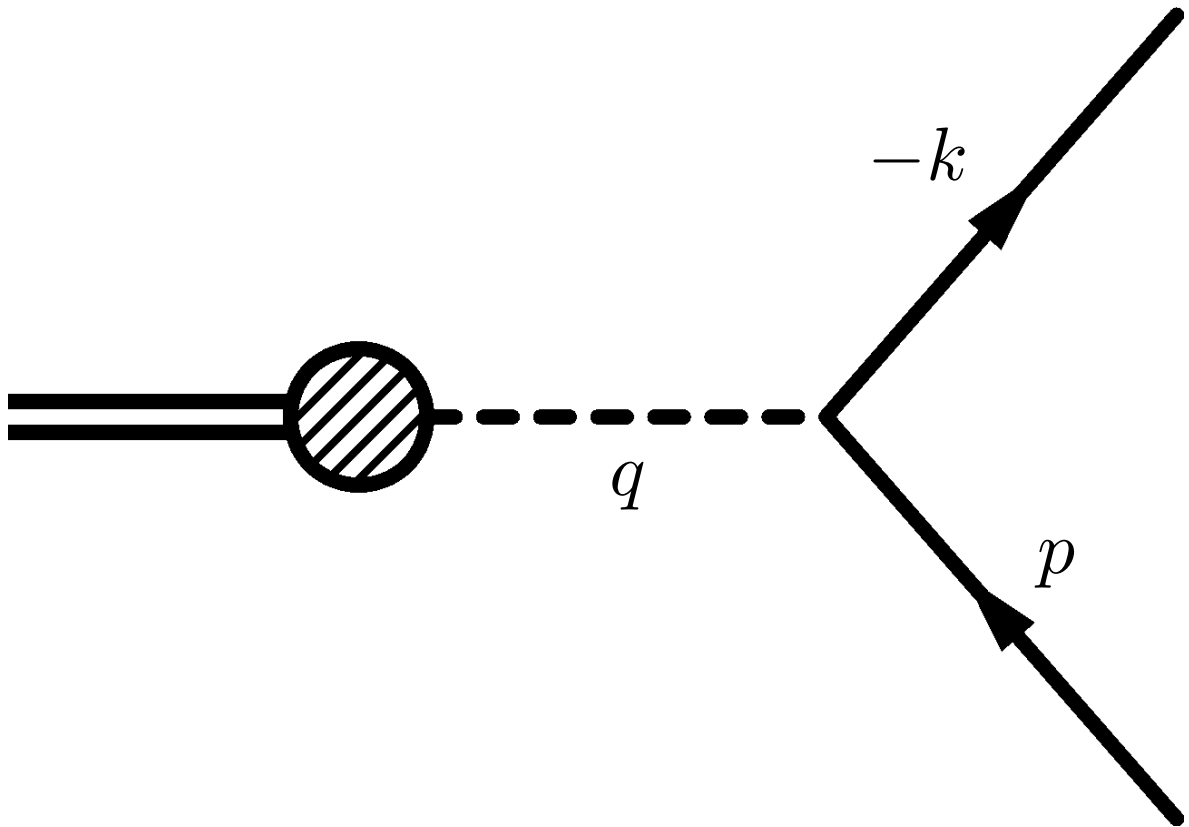
Figure 1.3: A Feynman diagram depicting the tree level decay of a pion.

are a pictorial representation of the matrix element. We may write the mathematical representation of Figure 1.2 as (1.7):

$$\mathcal{M} = \frac{G}{\sqrt{2}} g_l f_\pi m_l \bar{u}(p) \gamma_\mu (1 - \gamma^5) \nu(k).$$

(1.7)

For the time we will spare the mathematical details and focus instead on the physics involved. The critical term in this matrix element is $1 - \gamma^5$. To understand this term is to understand everything about the weak force. The term is a combination of a vector interaction and an axial-vector interaction. The difference between these two kinds of vectors is the symmetry of parity (a complete spatial inversion). Interactions that contain this combination $(V - A)$ maximally violate the parity symmetry. In other words if we describe a particle using vectors and axial-vectors and observe a correlation

between the two quantities then we know the interaction violates parity. The weak force is the only part of the standard model with this term so a parity violation signal is a signal of the weak force.

In charged pion decay this parity term plays a critical role in determining the ratio of decays that follow the electronic versus the muonic channel. Unlike the phase space consideration where the light electron mass increased the decay rate in this case the light electron mass decreases the decay rate dramatically. On account of the two body nature of the decay process the summed momentum of the decay products must cancel out (the particles fly apart back to back). However the pion is also spin-0, therefore the spins of the two decay particles must also be in opposite directions. That means we have both particles with their spin the direction of their momentum[16]. The trouble is that the $(V - A)$ term forces particles to be left handed and anti-particles to be right handed. The decay should not even be allowed at all!

However this concept of handedness is not a Lorentz invariant quantity. The lack of Lorentz invariance means that we are able to violate this forced handedness in proportion to the mass of the particle. In terms of our decay, the muon is much more massive than the electron, therefore the probability of violation is much higher and hence the matrix element for the muon is much larger. Now that we understand the physics behind the math we may write the tree level decay rate for charged pions as:

$$\Gamma = \frac{1}{\tau} = \frac{G^2}{8\pi} g_l f_\pi^2 m_\pi m_l^2 \left(1 - \frac{m_l^2}{m_\pi^2}\right)^2 \tag{1.8}$$

The decay rate is given by (1.8), where g_l represents the strength of the coupling and f_π is the pion decay constant (the term that hides the interaction in the blob in Figure 1.2). We can estimate the value of the decay constant but it will introduce large errors in any calculation. By comparing the probabilities of different pion decay channels, formally

---

[16]When a particle's spin aligns with its momentum we say the particle is "right handed".

called *branching ratios*, we can eliminate this large systematic error and make very precise predictions. Throughout the remainder of the dissertation we will use the notation π_{2e} to represent the pion decay channel into a positron. In a similar fashion other decays will be represented with the relevant particles listed. We will always supress the neutrinos in this notation.

1.2.3   Branching Ratios

$\pi \rightarrow e\nu_e$

Taking the ratio of the π_{2e} and $\pi_{2\mu}$ process yields (1.9),

$$B_{\pi \rightarrow e\nu_e} \equiv \frac{\Gamma(\pi \rightarrow e\nu_e)}{\Gamma(\pi \rightarrow \mu\nu_\mu)} = \left(\frac{g_e}{g_\mu}\right)^2 \left(\frac{m_e}{m_\mu}\right)^2 \left(\frac{m_\pi^2 - m_e^2}{m_\pi^2 - m_\mu^2}\right)^2 \approx 1.2 \times 10^{-4}. \qquad (1.9)$$

The only inputs we need to know to calculate the branching ratio (B) are the masses of the particles involved and the value of g_l. The masses are well known and studied, however the term g_e/g_μ is not. Many sources do neglect this term all together and state the weak force couples to the electron and the muon with the same strength. This unified coupling is called *weak lepton universality*[17]. By measuring the branching ratio precisely we can measure the degree to which lepton universality holds. In fact this decay is the most precise way to do so [14].

Current theory predicts the branching ratio of the π_{2e} decay with an uncertainty of one part in 10^8[21]. This level of precision is remarkable and yields deep insight into a number of open questions. However current world experimental average has an uncertainty of four parts in 10^7. The discrepancy is more than one order of magnitude. The theory has made predictions that indicate a rich wealth of information is just over the horizon. The experimental uncertainty must be decreased for us to tap into this

[17]See http://pen.phys.virginia.edu/talks/pen_bvr2006.pdf page 7.

rich vein of information. Experimentally verifying this theoretical calculation is the fundamental goal of the PEN experiment.

$\pi \to e\nu_e\gamma$

Any experimentally measured branching ratio for $\pi \to e\nu_e$ implicitly includes radiative events. Soft photons are radiated through bremsstrahlung with very high probability and it is not practicable to divorce those events from the naked $\pi \to e\nu_e$ events. Therefore the previous subsection while theoretically accurate hides some of the experimental complexity. In fact for the PEN experiment the aim is to measure:

$$B_{\pi \to e\nu_e} \equiv \frac{\Gamma(\pi \to e\nu_e) + \Gamma(\pi \to e\nu_e\gamma)}{\Gamma(\pi \to \mu\nu_\mu) + \Gamma(\pi \to \mu\nu_\mu\gamma)}. \tag{1.10}$$

However there is another source for photons in the radiative decays. The constituents of the pion posses electric charge. Therefore during the transmutation of the quarks (the shaded region in 1.3) a photon can be emitted. Analysis of those photons yields information about the structure of the pion. Since the radiative events are part of the experimental branching ratio, obtaining the radiative branching ratio requires a renormalization and nothing else:

$$B_{\pi \to e\nu_e\gamma} = B_{\pi \to e\nu_e} \left(\frac{N_{\pi \to e\nu_e\gamma}}{A_{\pi \to e\nu_e\gamma}}\right) \left(\frac{A_{\pi \to e\nu_e}}{N_{\pi \to e\nu_e}}\right) \tag{1.11}$$

Here N is the value for the number of observed events and A is the acceptance attributed to that process. The details of determining if a photon is from bremsstrahlung or structure interactions will be presented in Chapter 2. In addition to giving information about the structure functions of the pion (F_V and F_A) using the *conserved vector current* hypothesis a determination of the neutral pion lifetime is also possible.

1.3   The PEN Experiment

Proposed in January 2006 the PEN experiment is dedicated to measure the $\pi^+ \rightarrow e^+\nu$ branching ratio with a relative uncertainty of 5×10^{-4} or lower at the Paul Scherrer Institut (PSI) in Switzerland. The main experimental apparatus was commissioned for the PIBETA [22] experiment and has been under successful operation at PSI since 1999. From 2008-2010 the PEN experiment collected a large data set sufficient for reaching the main goal of the PEN experiment [23]. The experiment went through constant innovation including the design and implementation of a novel miniature time projection chamber. In addition to the main goal other measurements are possible, including radiative pion decay modes as well and purely leptonic muon decays. The scope of this dissertation will be the measurement of the radiative decay mode $\pi \rightarrow e\nu_e\gamma$.

The main components of this experiment are data collection, simulation, and data analysis. This dissertation contains a description of the data collection procedure and detailed breakdown of the PEN detector system. In addition a fully integrated simulation software suite was developed using GEANT4 and stand alone C++ programs to produce a simulated data file of identical form to the PEN experiment data file. The final part of this dissertation is a description of the simulation principles and techniques as well the application of the simulation to data analysis and branching ratio calculation.

Part I

Paul Scherrer Institut

Villigen, Aargau

Confoederatio Helvetica

Chapter 2

π^+ Decay Kinematics

Before describing the PEN detector system the kinematics of the physics processes must be well understood. This chapter describes the particles and the energies to be detected. First we begin with the generic decay of the pion into a lepton and discuss the associated Michel decay. Then a detailed description of the radiative pion decay mode $\pi \to e\nu_e\gamma$ will be presented, followed by a summary of all the relevant final state particles.

It must also be well understood that there are two main approaches to measuring pion decay. One is to use a stopped pion approach, the other is to observe pion decays in flight[1]. The PEN experiment elected to use a stopped beam approach. Since the pion must be stopped in some medium, positively charge pions must be used for a stopped beam measurement. If negatively charged pions were used, their interactions with the nuclei present in the stopping material would make the measurement impossible. As a result the remainder of this dissertation will only discus positively charged pions and their decay products.

---

[1]An example of a decay in flight experiment can be found in [24].

2.1 $\pi \to l\nu_l$

Much of this decay was discussed in Chapter 1. This Section just provides a review and sets the table for the discussion of more complicated processes relevant to the experiment. The important feature in this case is that the pion rest frame is the lab frame. Since there are only two outgoing particles their energies are fixed. Unfortunately no high efficiency neutrino detectors exist, so only the outgoing charged lepton may be detected with necessary statistics for the PEN measurements. As discussed earlier there are two candidates for the final state lepton: positrons and muons. For positrons this decay releases a kinetic energy of about $70\,\mathrm{MeV}^2$. For muons the energy is about $4\,\mathrm{MeV}$. In fact these muons do not have enough energy to escape the stopping target. However the story is not over for the muons. They subsequently undergo decay through the same standard model mechanism as the pion, producing a positron with enough energy to escape the target.

2.2 $\mu \to e\nu_e\nu_\mu$

Given the mass of the muon and the conservation laws discussed in Chapter 1 the only possible particle that can carry away the charge of the muon is a positron. Using that information along with the standard model conservation laws the only tree process for muon decay is depicted in Figure 2.1. For historical reasons this decay process is called Michel decay after Louis Michel who made large contributions to the understanding of this process [25]. This decay unlike that of the pion is a three body decay and that extra degree of freedom enables the decay positron to have a range of energies up to about $50\,\mathrm{MeV}$.

---

[2]The neutrino also has energy sufficient to conserved energy and momentum.
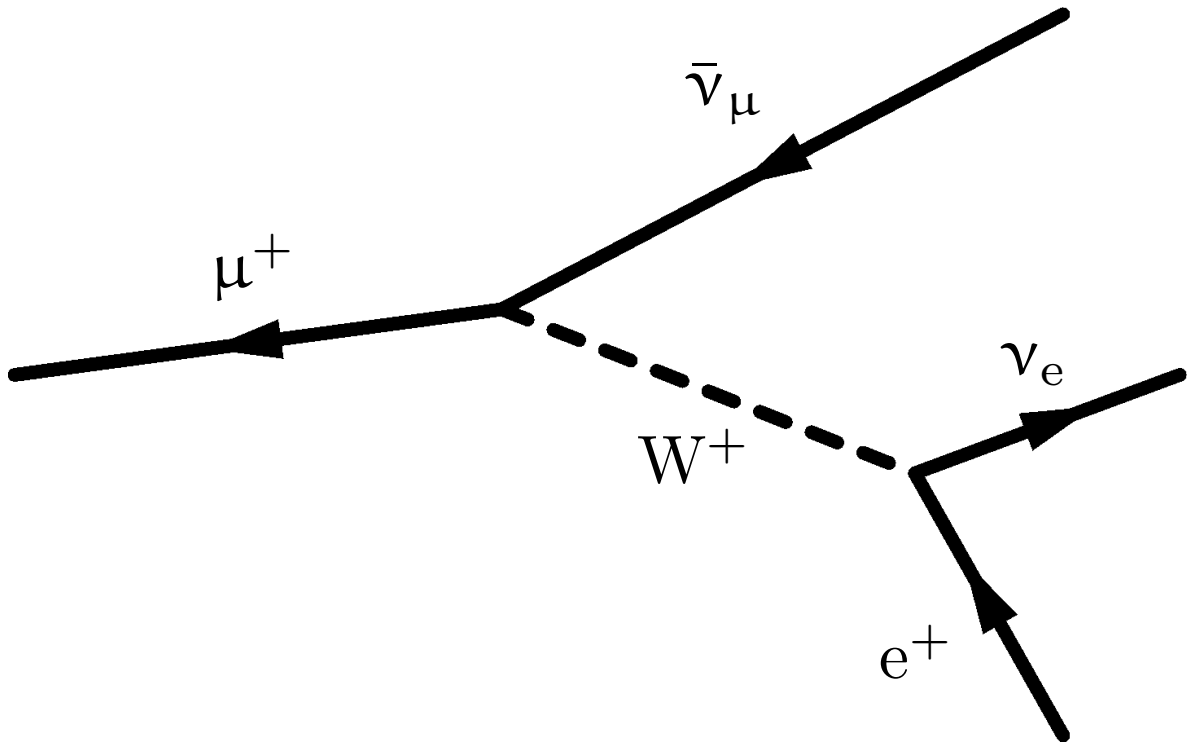
Figure 2.1: Feynman diagram representing the Michel Decay

2.3 $\pi \to e\nu_e\gamma$

At every step of the standard pion decay process a charged particle may emit a photon
. If that photon leaves the system the process becomes a radiative pion decay. Figure
2.2 shows a process independent picture of the radiative pion decay into a final state
electron channel. There are two components to understanding the decay of a pion. The
first part is the kinematics or phase space, the second is the higher level interaction-
specific component called the amplitude ($\mathcal{M}$). First a description of the kinematics will
be done because it is simpler than the amplitude.

There are 12 unknown kinematic quantities in this final state (the 4-momentum
components of each outgoing particle). However through use of energy and momentum
conservation along with the principle of mass-energy equivalence [26], that number of
liberties is reduced to five. Furthermore, by exploiting the freedom of basis choice, the
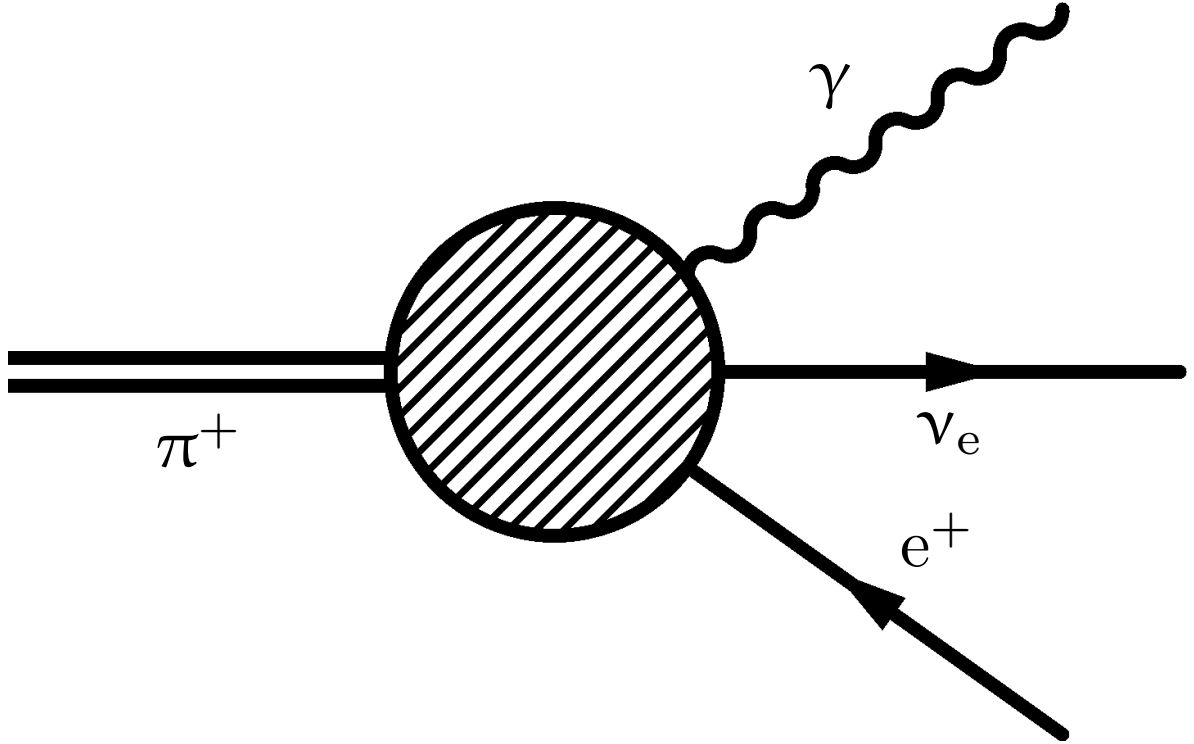
Figure 2.2: Feynman diagram representing the process independent electronic radiative channel

system can be determined in full by measuring only two quantities, the energy of the positron and the energy of the photon.

The standard parametrization in the literature yields (see [14] and [27]):

$$x = 2p_\pi \cdot k/m_\pi^2 \quad , \quad y = 2p_\pi \cdot p_e/m_\pi^2 \quad , \quad z = 2p_\pi \cdot p_\nu/m_\pi^2, \tag{2.1}$$

with p_π, p_e p_ν, and k, representing the four-momenta of the pion, positron, neutrino, and photon, respectively. In the laboratory frame these equations reduce to:

$$x = 2E_\gamma/m_\pi^2 \quad , \quad y = 2E_e/m_\pi^2 \quad , \quad z = 2E_\nu/m_\pi^2, \tag{2.2}$$

thus this form will be used exclusively. The plots will be plotted in units of $m_\pi/2$ so the

axis will range from 0 to 1. For example Figure 2.3 shows the opening angle between the photon and the positron which can be calculated using:

$$\cos\theta_{e\gamma} = \frac{y(x-2) + 2(1-x+r^2)}{x\sqrt{y^2 - 4r^2}} \tag{2.3}$$

with r representing m_e/m_π.
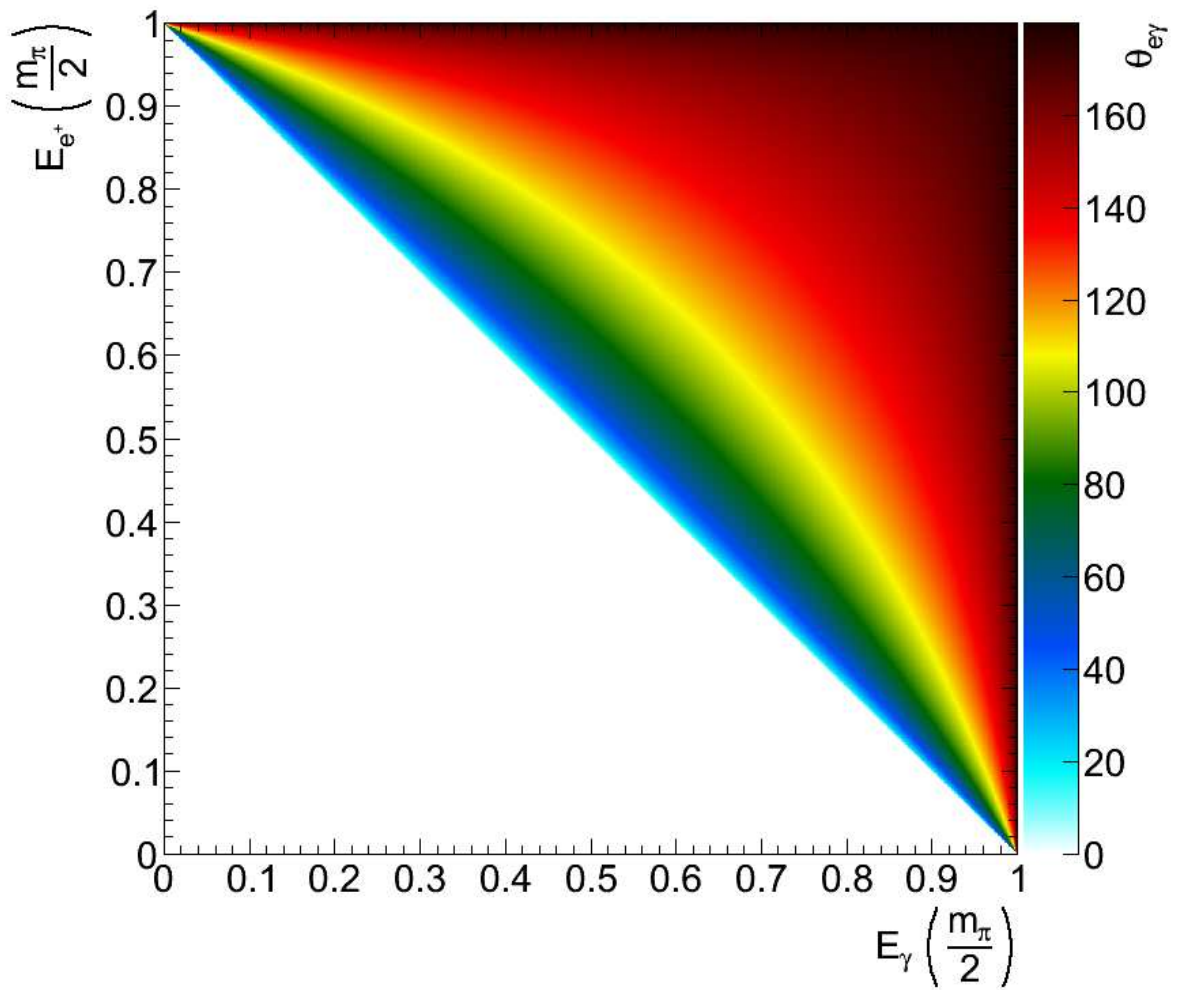
Figure 2.3: Opening angle $\theta_{e\gamma}$ in the E_e-E_γ basis.

The kinematic regions of interest involve opening angles of photon and positron that are large, therefore a wide acceptance is required for both particles. Furthermore

simultaneous measurement of the positron and photon energies with the opening angle is very powerful in terms of reducing background signals.

Now that the kinematics are out of the way the exciting work may begin. As will be demonstrated, the amplitudes provide the probabilities of certain processes producing events in different regions of phase space. It is these differences which will be used to extract the exciting physics. The amplitude for radiative pion decay is:

$$\mathcal{M}(\pi \to e^+\nu_e\gamma) = \mathcal{M}_{SD} + \mathcal{M}_{IB}, \tag{2.4}$$

where $\mathcal{M}_{SD}$ is the amplitude for structure-dependent processes and $\mathcal{M}_{IB}$ is the amplitude for bremstrahlung processes. The final form of the decay rate involves the square of the amplitude, therefore an interference term will also arise.

2.3.1 Structure Dependent Terms

There are two components to the structure dependent amplitude. The fundamental nature of the weak force is contained in the Lagrangian term $\gamma_\mu(1 - \gamma_5)$ which produces the characteristic $(V - A)$ behavior. Therefore these two amplitude components are F_V and F_A. Figure 2.4 shows the Feynman diagram for structure dependent radiative decay. The blob represents the strong interactions combined with the weak vertex that transmutes the pion into a W boson. That transmutation can take place through either the V or A component of the weak Lagrangian.

Mathematically Figure 2.4 is represented as follows:

$$\mathcal{M}_{SD} = \left(e\frac{G}{\sqrt{2}}\frac{\cos\theta_c}{m_\pi}\right)\epsilon_\nu^*[\bar{u}_\nu\gamma_\mu(1-\gamma_5)\nu_e] \cdot [F^V(s)\epsilon^{\mu\nu\alpha\beta}p_{\pi\alpha}k_\beta + iF^A(s)(g^{\mu\nu}(p_\pi \cdot k) - k^\mu p_\pi^\nu)].$$

$$\tag{2.5}$$
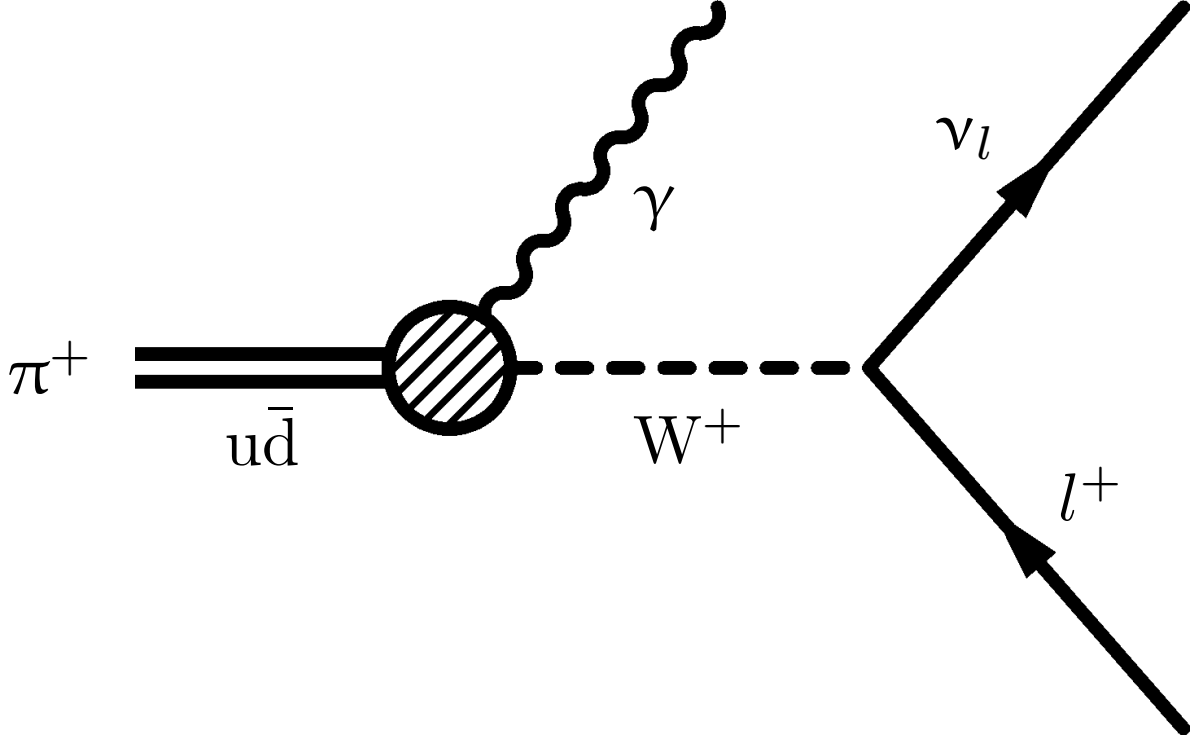
Figure 2.4: Feynman diagram representing the process of Structure dependent electronic radiative channel

Invoking photon helicity modes and introducing λ along with treating the system in the pion rest frame (2.5) reduces to

$$\mathcal{M}_{SD} = ie\frac{G}{2\sqrt{2}}\cos\theta_c m_\pi \times \bar{u}_\nu \epsilon_\nu^*(1 - \gamma_5)\nu_e[F^V(s) + \lambda F^A(s)]. \qquad (2.6)$$

Finally, we square the amplitude, and then sum over all polarizations. Applying the kinematic factors we arrive at the decay rate for structure-dependent processes:

$$\frac{d^2\Gamma_{SD}}{dxdy} = \frac{\alpha}{8\pi}\Gamma_{\pi\to e\nu}\left(\frac{m_\pi}{m_e}\right)^2\left(\frac{1}{f_\pi}\right)^2[(F_V + F_A)^2 SD^+(x,y) + (F_V - F_A)^2 SD^-(x,y)]. \qquad (2.7)$$

As shown in (2.7) the final form of the decay rate involves the pion form factors but only in combination with kinematic weights $[SD^+(x,y)$ and $SD^-(x,y)]$.
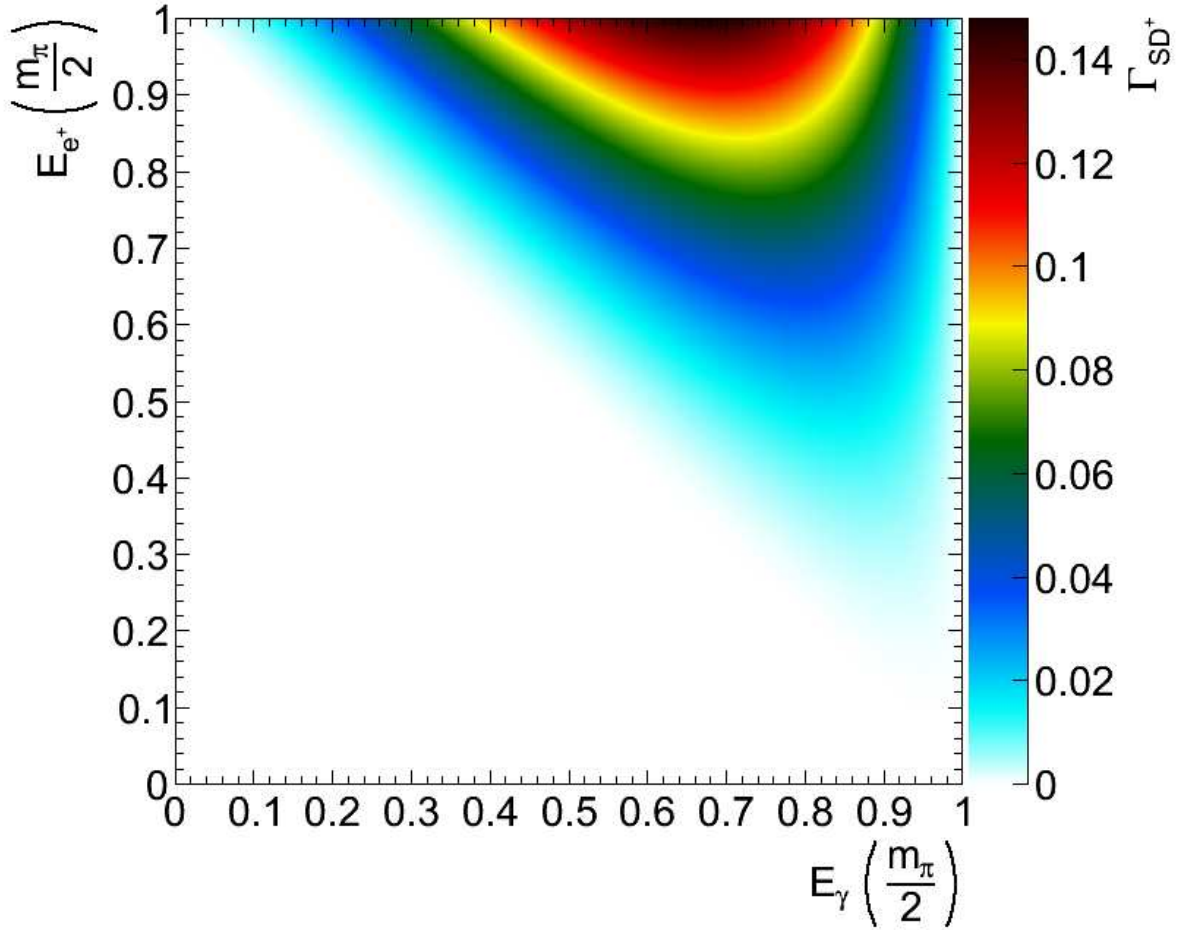
Figure 2.5: SD$^+$ Decay Rate in standard parametrization

Figures 2.5 and 2.6 show the decay rate for the different components in the standard positron energy vs. photon energy plane. The SD^+ contribution dominates in the large photon and large positron energy region whereas the SD^- contribution dominates in the similar region of photon energy, but with a minimal positron energy contribution. The clear separation of these regions is advantageous because it permits an independent measurement of $F_V + F_A$ and $F_V - F_A$.

Looking at both of the regions together we see that structure-dependent photons tend to be at larger photon energies. We also note that the SD^+ term contribution is largest for maximum positron energies and the SD^- contribution is largest for maximum
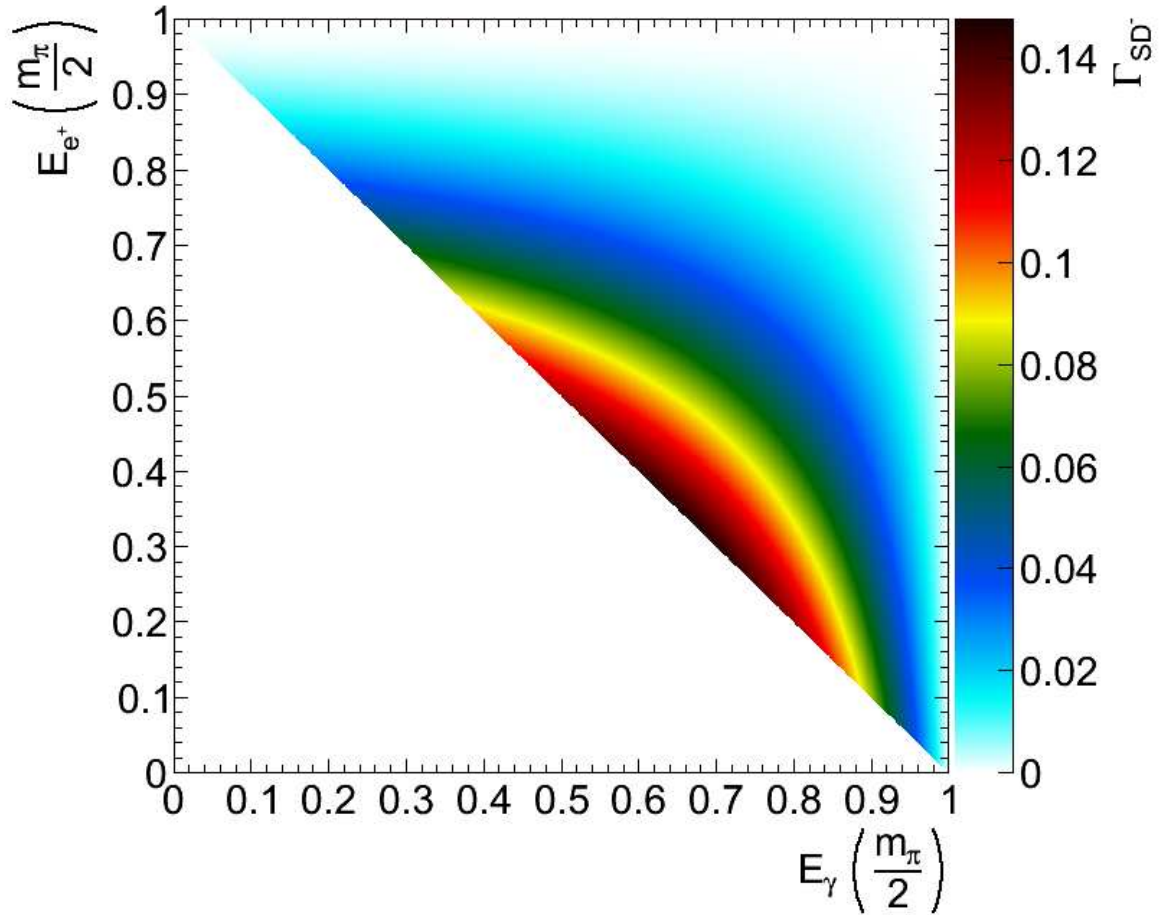
Figure 2.6: SD$^-$ Decay Rate in standard parametrization

neutrino energies. This information suggests that the SD^+ contribution will be easier to extract experimentally from the data.

2.3.2 Inner Bremsrahlung Terms

The other component of the amplitude is the bremstrahlung contribution, the basic diagram is represented in Figure 2.7.

It is important to note that the positron-photon vertex includes an incoming positron that is virtual. This virtuality enables some sidestepping of the strict kinematics outlined in section 2.3. The mathematical representation of this diagram is given by:
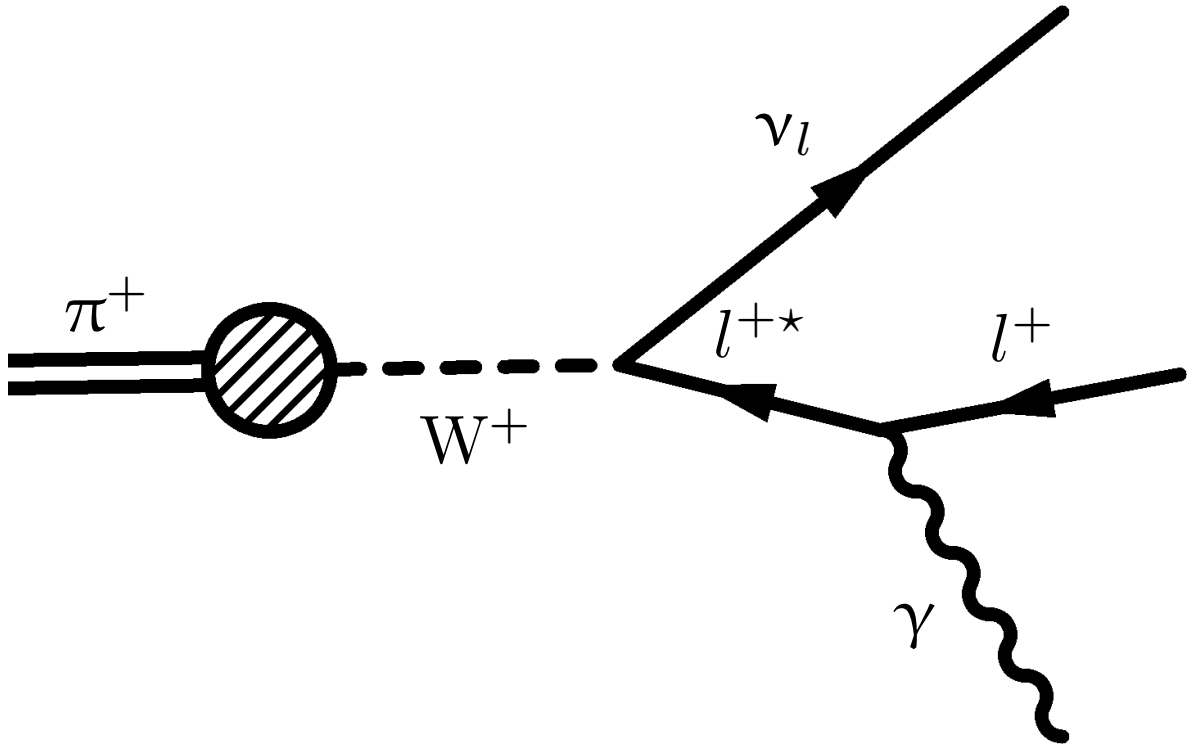
Figure 2.7: Feynman diagram representing the process of Inner Bremstrahlung electronic radiative channel

$$\mathcal{M}_{IB} = -ie\frac{G}{\sqrt{2}}\cos\theta_c f_\pi m_\pi m_e \bar{u}_\nu.\left(\frac{\frac{1}{2}k\epsilon^* + p_e \cdot \epsilon^*}{p_e \cdot k} - \frac{p_\pi \cdot \epsilon^*}{p_\pi \cdot k}\right)(1+\gamma_5)\nu_e \qquad (2.8)$$

The second term in parentheses represents the photon originating from the pion (diagram not shown). Processing (2.7) in the standard fashion produces the decay rate for the bremstrahlung component of radiative decay:

$$\frac{d^2\Gamma_{IB}}{dxdy} = \frac{\alpha}{2\pi}\Gamma_{\pi\to e\nu}IB(x,y). \qquad (2.9)$$

Again, much like the decay rate for the structure dependent terms in (2.7), the decay rate for the non-radiative channel is present along with a purely kinematic factor $IB(x,y)$, Figure 2.8 graphically shows the structure of the kinematic function.
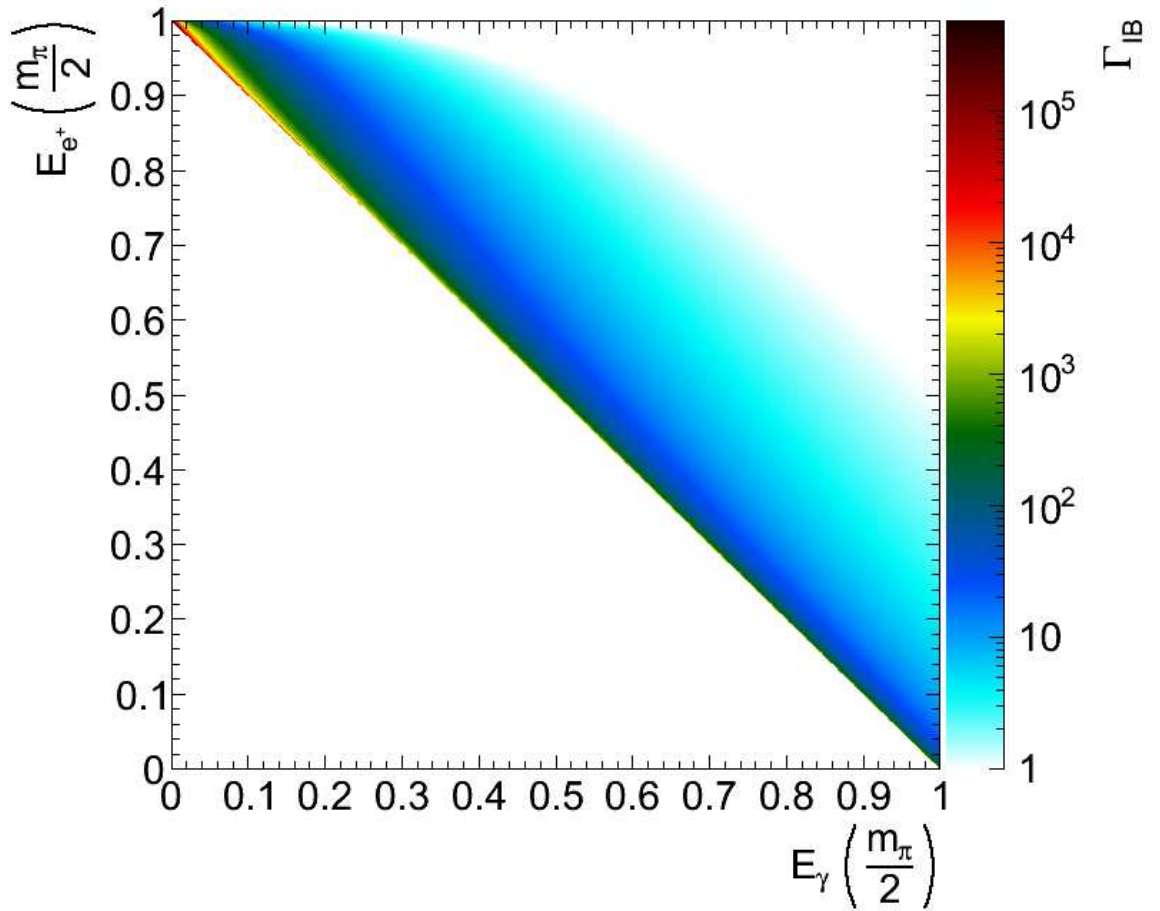
Figure 2.8: $IB(x,y)$ represented graphically (n.b. log scale).

The total radiative pion decay rate is dominated by the bremstrahlung component (note the scales in Figures 2.8, 2.5, and 2.6. Fortunately the IB component exists mainly along the line of maximal neutrino energy. This behavior means relatively little interference in the SD^+ region but will create quite a bit of trouble in the SD^- region.

2.3.3 SD-IB interference terms

There is no diagram representing the interference term between the SD and IB contributions to the amplitude. Rather it arises from the squaring of the amplitude required for calculating the decay rate.

$$\mathcal{M}_{INT} = -ie\frac{G}{\sqrt{2}}\cos\theta_c\frac{p_\pi \cdot k}{m_\pi}[F^{A*}(s) + \lambda F^{V*}(s)]\bar{\nu}_e(1 + \gamma_5)\epsilon u_\nu. \tag{2.10}$$

Following the same prescription as before we convert (2.10) into the interference decay rate:

$$\frac{d^2\Gamma_{INT}}{dxdy} = \frac{\alpha}{2\pi}\frac{1}{f_\pi}\Gamma_{\pi\to e\nu}[(F_V + F_A)F(x,y) + (F_V - F_A)G(x,y)]. \tag{2.11}$$

The structure of this decay rate is similar to the previous ones and once again the kinematic weight is shown graphically (see Figure 2.9).
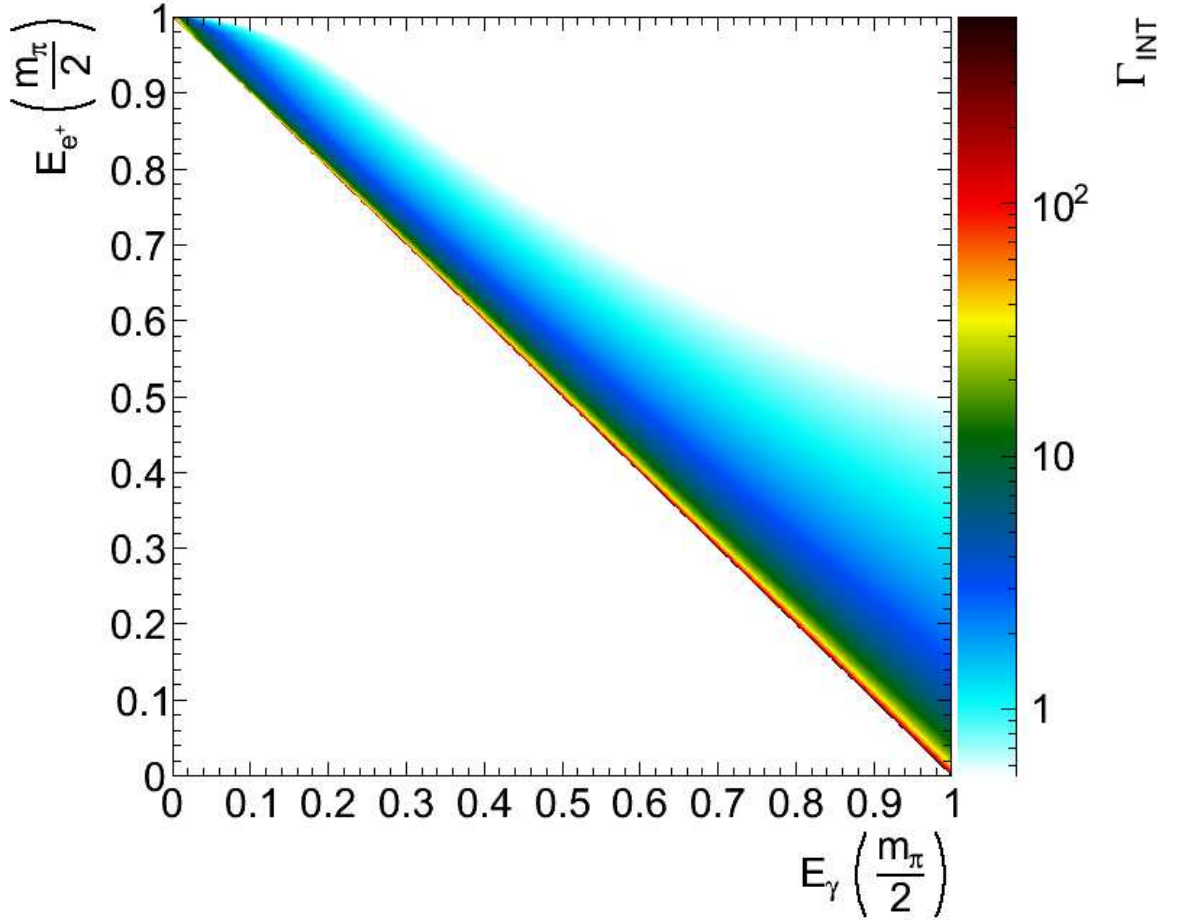
Figure 2.9: $(1 + \gamma) \cdot F(x, y) + (1 - \gamma) \cdot G(x, y)$ represented graphically (n.b. log scale).

2.3.4 Total Radiative Decay Rate

Figure 2.10 shows the total decay rate for radiative pion decay. The behavior is mostly dominated by the inner bremstrahlung contributions (recall Figure 2.8). The fundamental physics contained in the bremstrahlung terms is all QED and while interesting to study there are more precise ways to do so. However lurking in the structure-dependent terms are the form factors F_V and F_A. By selecting regions of phase space where the structure-dependent terms dominate, the contributions of these factors to the decay rate grows. As a result measurements in those regions can yield information about the pion form factors.
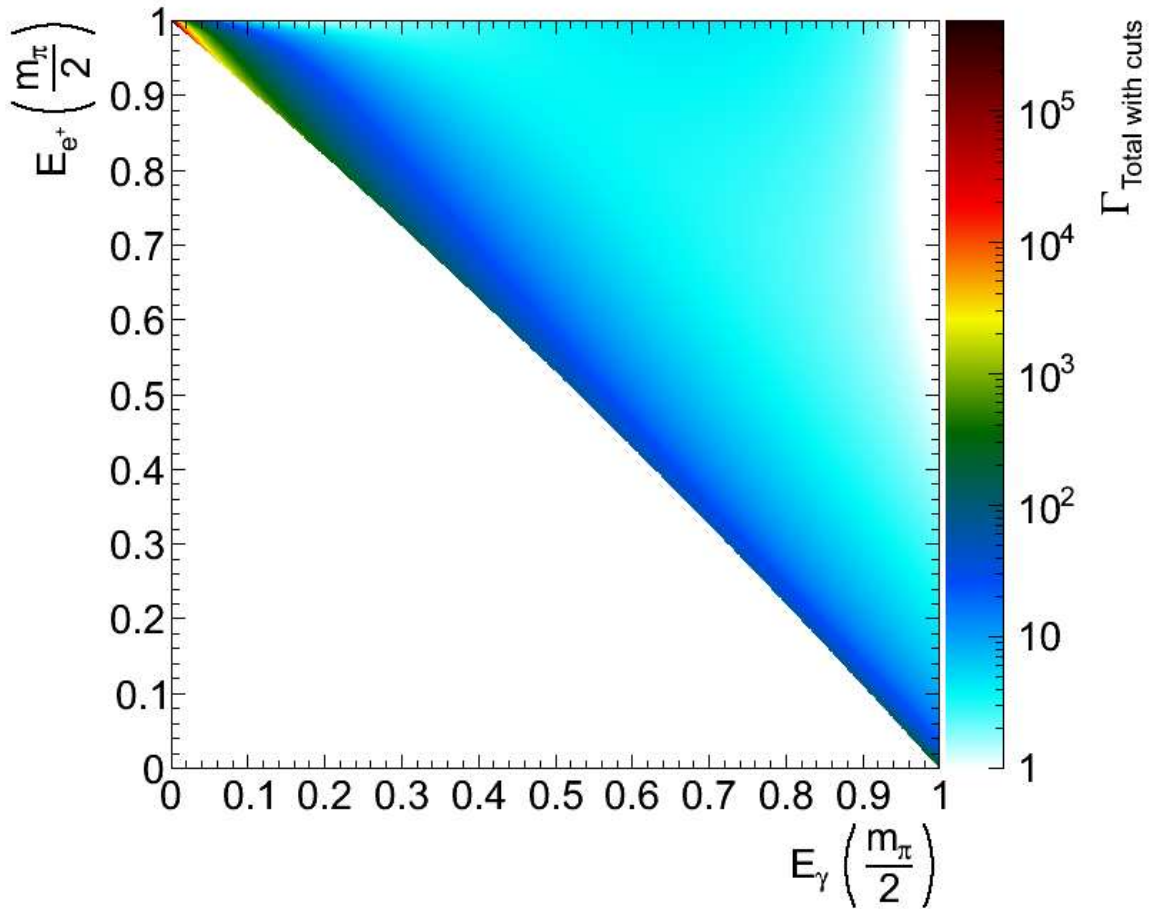
Figure 2.10: Total Decay Rate in standard parametrization (n.b. log scale).

Previous work on this channel by the PIBETA collaboration suggests the use of three regions helpful to the evaluation of γ (the ratio of axial-vector to vector form factors F_A/F_V) [1]. Table 2.1 shows a summary of the regions, including the kinematic cuts that define each region. The yield column represents the reduction in statistics expected from the kinematic cuts. The last three columns represent the change in the decay rate for a 1% change in the indicated parameter.

Table 2.1: Differential Sensitivity calculated for a 1% change in parameter.

Region	$E_{e^+} >$	$E_\gamma >$	%Yield	$\% \frac{d\Gamma(SD^+)}{(\Gamma + d\Gamma)}$	$\% \frac{d\Gamma(SD^-)}{(\Gamma + d\Gamma)}$	$\% \frac{d\Gamma(\gamma)}{(\Gamma + d\Gamma)}$
A	50	50	0.0084	0.1899	0.0007	1.1289
B	10	50	0.0479	0.0074	0.0025	0.1899
C	50	10	0.1279	0.0051	0.0003	0.1853

To further help the understanding Figures 2.11, 2.12, and 2.13 show the decay rate in the given kinematic regions. The most striking feature of Table 2.1 is the SD^- column and its low values. This behavior can be understood by examining Figures 2.6 and 2.8. The SD^- contribution is largest along the line of maximum neutrino energy $(X + Y = 1)$, the same place where the bremstrahlung contribution is large. However, the values of SD^+ are largest along maximal positron energy and large photon energy (the worst region for bremstrahlung).

Therefore these measurements will be most sensitive to the SD^+ contribution of the pion form factors, namely $F_V + F_A$. In the $F_V - F_A$ plane this measurement would be represented by an ellipse along the line perpendicular to $F_V = F_A$. Knowledge of $F_V - F_A$ would produce an ellipse along the line $F_V = F_A$ and both ellipses would intersect around the true value of F_V and F_A.
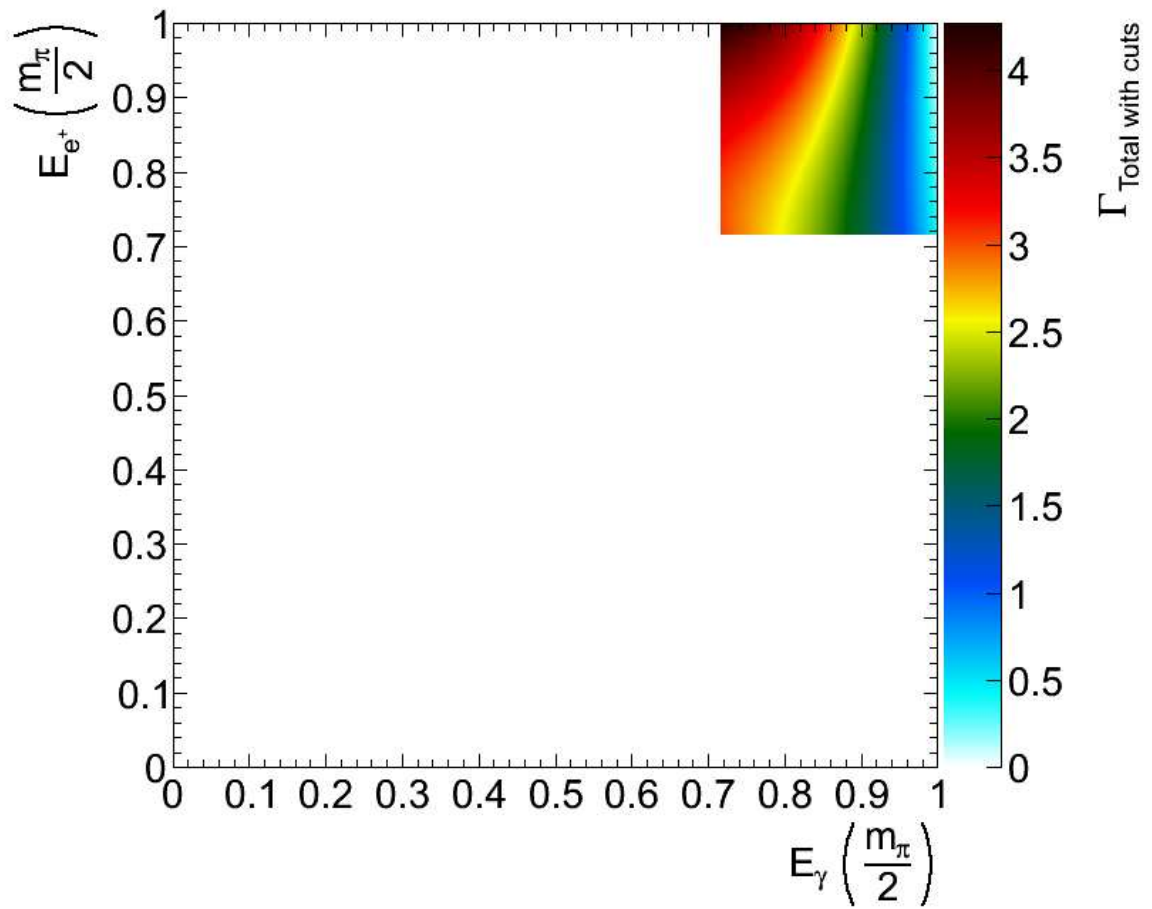
Figure 2.11: Total Decay Rate in standard parametrization (REGION A).
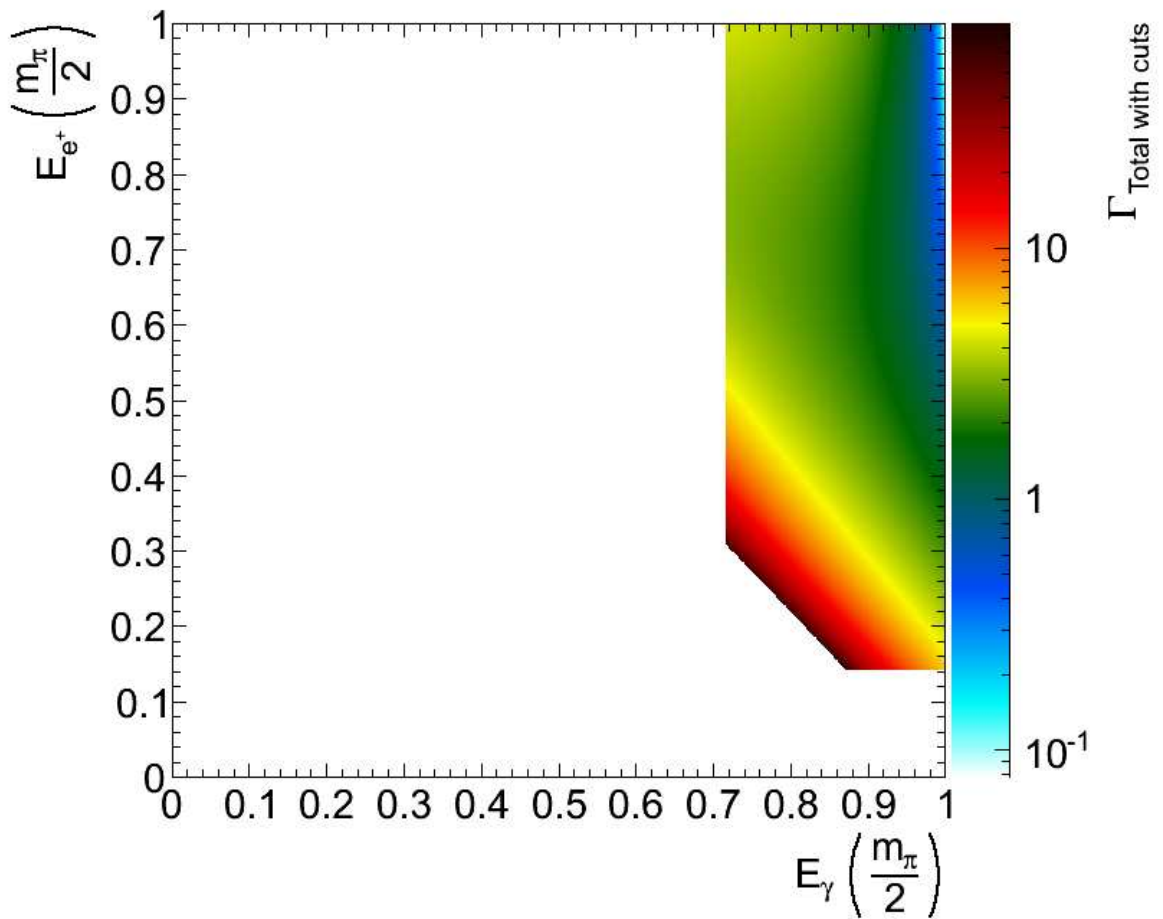
Figure 2.12: Total Decay Rate in standard parametrization (REGION B) (n.b. log scale).
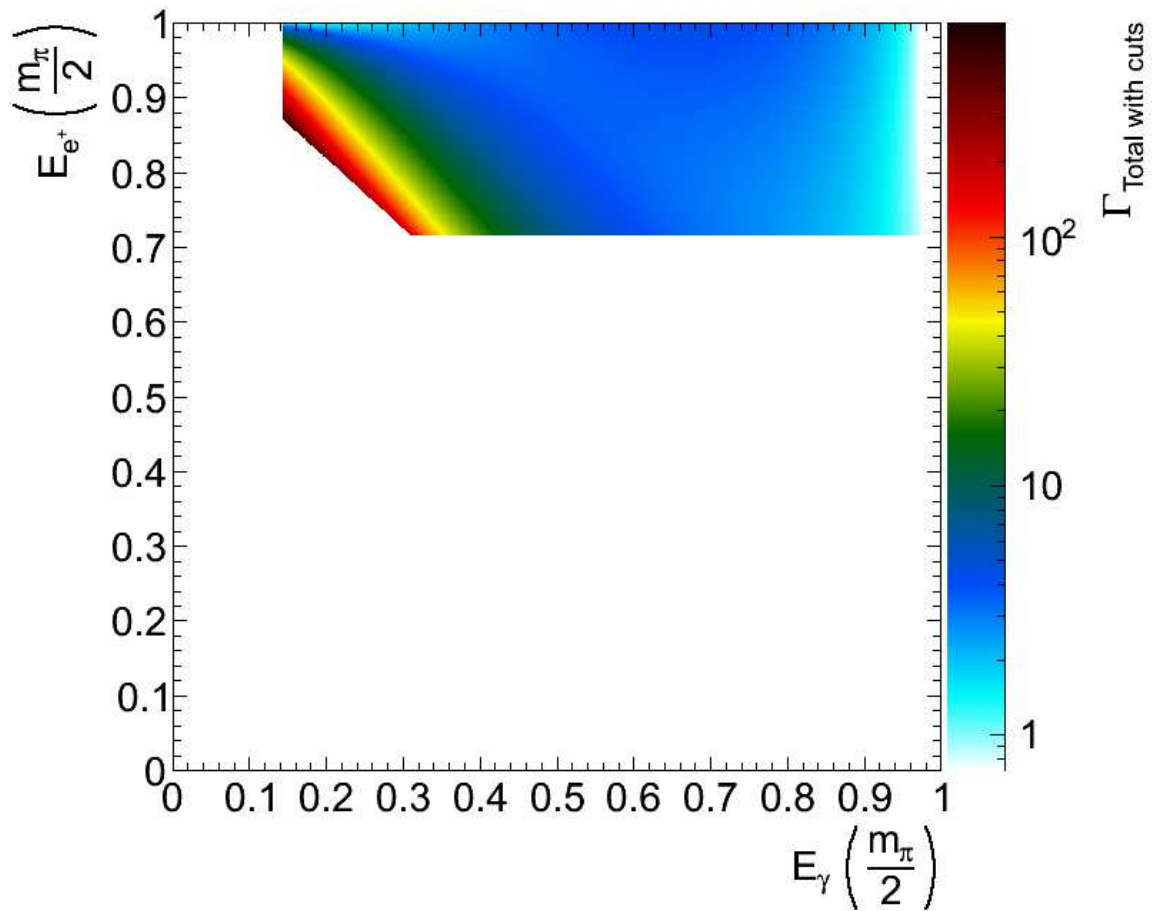
Figure 2.13: Total Decay Rate in standard parametrization (REGION C) (n.b. log scale).

Chapter 3

πE1 Beamline and PEN Detector

The first decision made in measuring pion decays is to choose between a stopped pion decay or a pion decay in flight. All subsequent detector decisions follow from this point. The PEN experiment elected to use a stopped beam approach. Therefore the experiment was placed at a high intensity low momentum pion beam line, the πE1 beam line at PSI (Paul Scherrer Institut, Switzerland). This chapter describes the experimental apparatus used to collect the data and the following chapter will describe the related hardware and software used to trigger the detector and store the information. We begin with a discussion of the method of pion production, followed by the pion stopping procedure. We finish this chapter with a detailed explination of the detectors used to record the decay products of the pion.

3.1 PSI User Facility

3.1.1 Proton Cyclotron

Commissioned in 1974 the ring cyclotron is the heart of the PSI particle physics program. Operating at a frequency of 50 MHz the apparatus emits pulses of protons with a proton
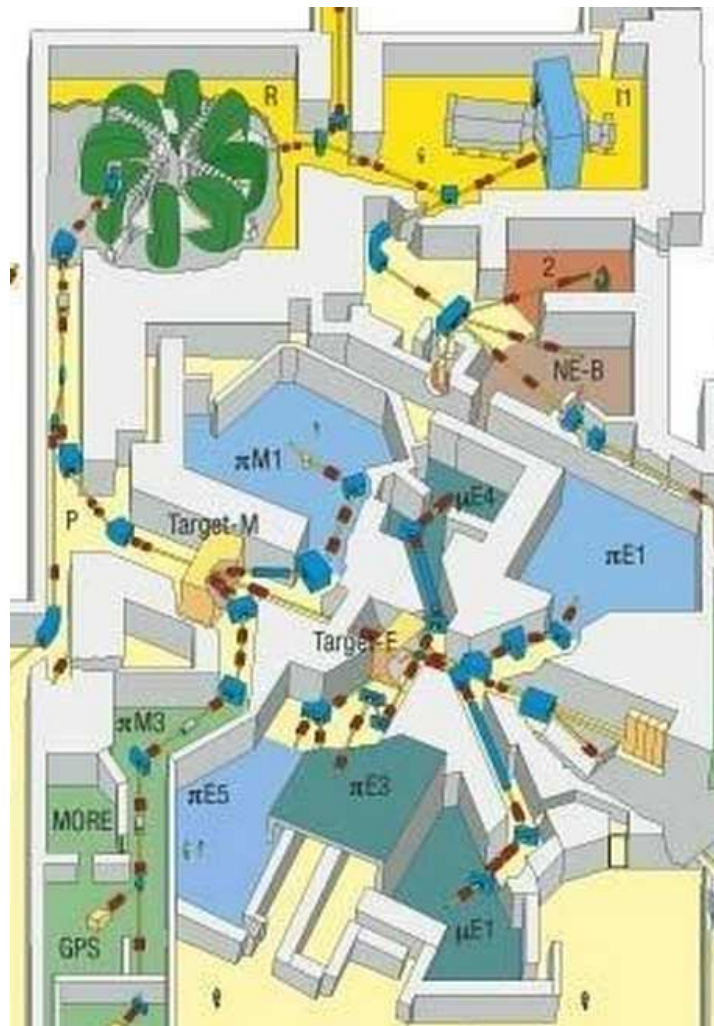
Figure 3.1: PSI experimental hall, πE1 is the PEN area (middle right).

current of up to 2.2 mA. The cyclotron is fed by a two stage process. First, protons are accelerated to 870 keV by a Cockcroft-Walton accelerator and then to 72 MeV by a smaller injector cyclotron. The final operating energy of the proton beam is 590 MeV. This beam is delivered to two separate graphite production targets and then on to the Swiss Spallation Neutron Source [28].

Figure 3.2: The $590\,\mathrm{MeV}$ proton accelerator ring

3.1.2 Carbon Production Target

In Figure 3.1 the two carbon targets are labeled "Target-M" and "Target-E". The goal is to produce pions from proton-proton interactions such as:

$$p + p \rightarrow p + n + \pi^+. \tag{3.1}$$

The designers of the target chose a material based on the following constraints. Light target elements do not provide sufficient density for the requirements of the lab (low pion yield, but very clean). Heavy nuclei targets lead to a higher rate of undesired particles such as neutrons (high yield but messy). Therefore a balance was struck and carbon was chosen. Additionally, carbon has some beneficial properties: good thermal conductivity for cooling, structural integrity in a vacuum, low thermal expansion, and so on. For thermal concerns the ring spins at $1\,\mathrm{Hz}$. The pions (and muons) that come out of these reactions are then guided electromagnetically to the different beam lines in

the experimental hall (see 3.1).
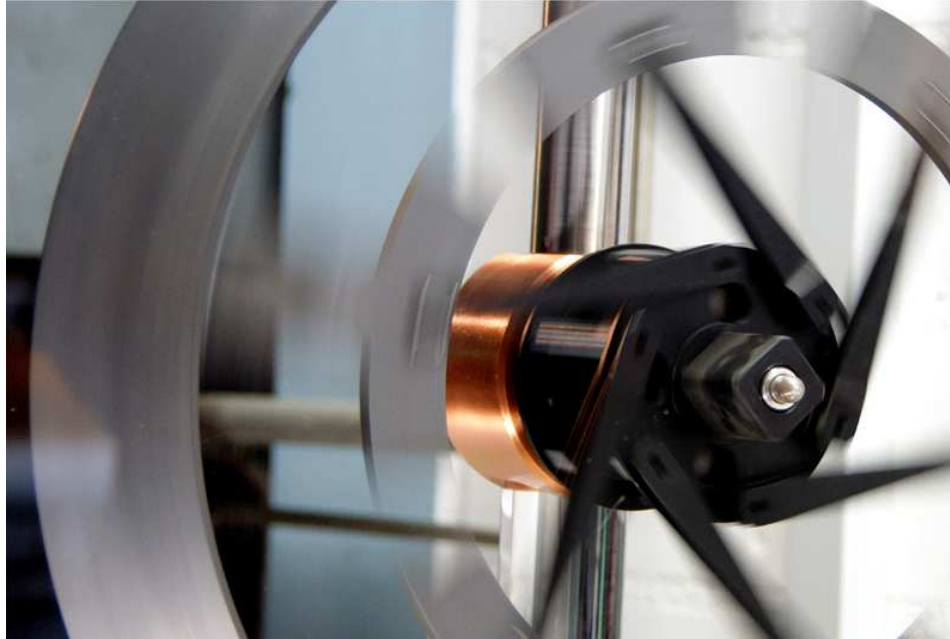
Figure 3.3: Pion production target.

3.1.3   πE1 Beam Line

The spallation products that emerge from the E target are shepherded to the πE1 area by a series of electromagnetic guides. Along the way there are physical colimators. The three bending magnets (ASZ51,FSH52, and ASL51) are shown in Figure 3.4.

In combination with the FSH52 slits, they select beam momentum in the range of 10 MeV to 500 MeV (the FSH52 slits also constrain the beam in the horizontal direction). The production yields are shown in Figure 3.5.

Since the PEN Experiment uses stopped pions, the momentum of the beam particle must be large enough to provide a reliable trigger while being as low as possible to reduce unwanted effects. The result is a momentum slice around 80 MeV/c. The FSH51 slits are used to constrain the beam in the vertical direction. Producing an overall beam profile show in Figure 3.6.

πE1

πE1-target

QSL54
QSL53

FSL51
QSL52
QSL51

FSH52

ASL51

30 °

QTB51
FSH51
QTH51
QTB51

ASY51
QTB52
QTB51

KSG51

P-beam

ASZ51

1 m

E-target

8 °
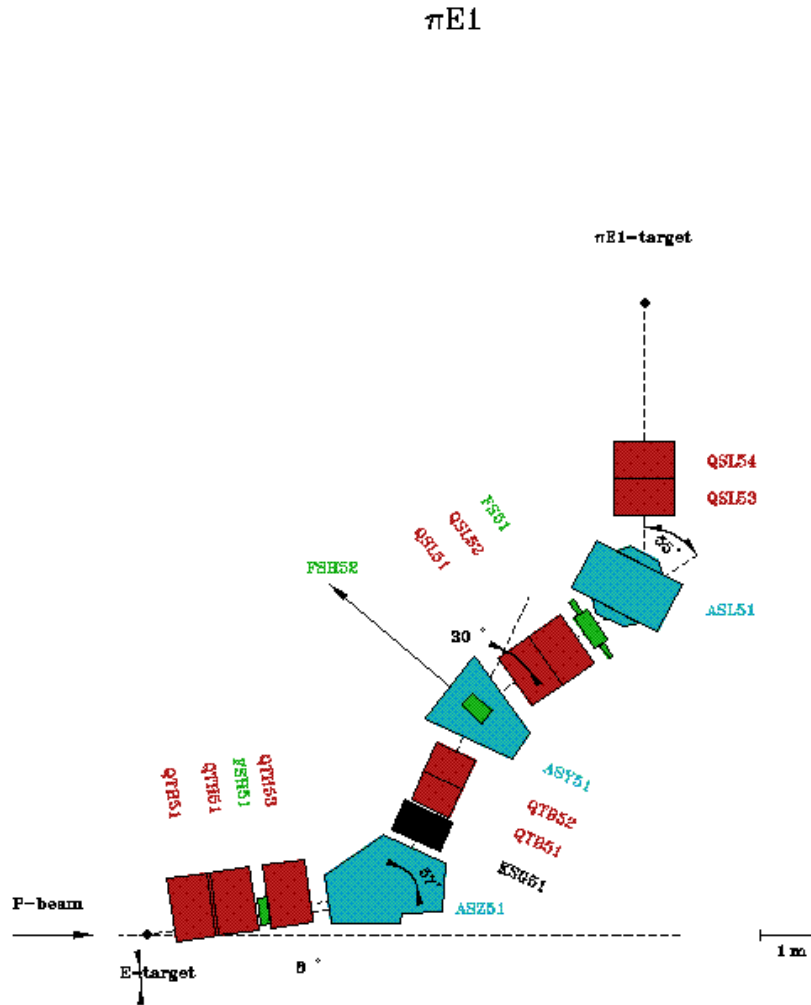
Figure 3.4: This diagram represents the beam line from the pion production target (bottom) to the detector area (top).

Finally the beam emerges into the πE1 experimental hall approximately 1.5 m off the ground. Figure 3.7 shows a picture taken looking directly at the beam line with no hardware in the detector area. Figure 3.8 shows the same area but with the PEN Experiment apparatus in place (albeit from a different vantage point, the lower gallery) [29]. There are several features of the experimental setup visible in Figure 3.8:

1. Beam pipe extending from the wall,
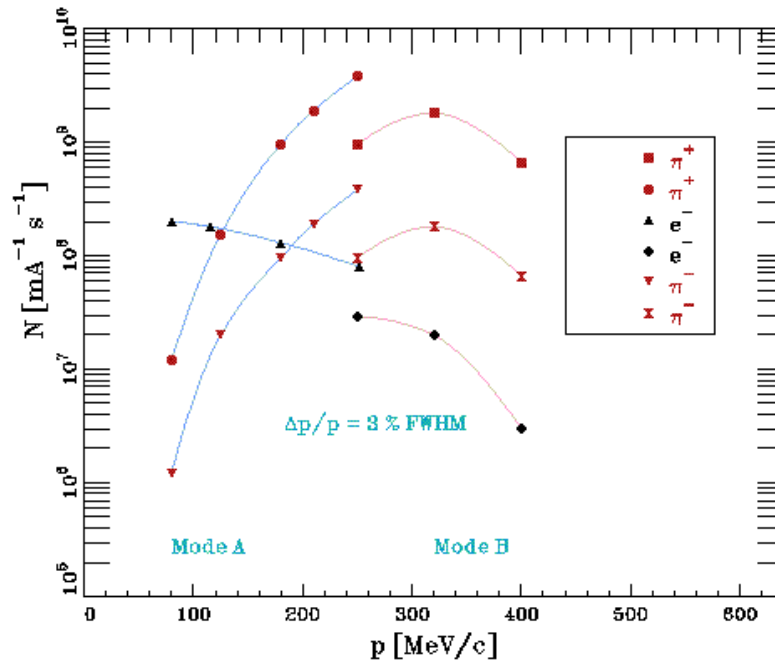
Figure 3.5: This plot represents the yield for different particles in the πE1 beam line. The π^+ curve of interest is represented by the red circles.
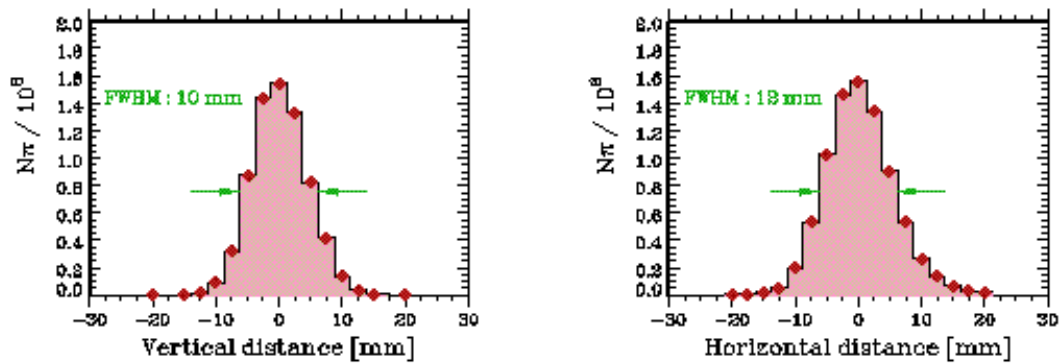
Figure 3.6: Profile in the transverse direction of the pion beam.

2. The final 3 focusing quadrupole magnets (red),

3. Lead wall,

4. Thermal house for the pen detector (wooden framed box),

5. Outer lead house that marries with lead wall (retracted),

6. Electronics room (wooden walled room next to the detector and behind the concrete wall),

7. Delay cables (big black spools),

8. High voltage system (to the right of the delay cables).

Figure 3.7: The πE1 area empty, looking at beam aperture (vantage: location of the detector).

3.2 Beam Line Detectors

The detector systems used in the experiment are divided into categories based on function and the particles they monitor. The first set of detectors lie along the path of

Figure 3.8: The πE1 area with the PEN detector in place (vantage: the lower gallery).

the pions as they emerge from the wall and ultimately stop in the target. There are three critical tasks the beam line detectors are designed to accomplish or provide data to accomplish:

1. Stop the pions,

2. Discriminate between pions and other particles,

3. Determine the pion stop time,

4. Determine the pion stopping position.

The beam momentum and the amount of material in the beam line must be chosen to stop the pions near the center of the target. Higher momentum produces increased background from scattering and nuclear interactions. Lower momentum makes extracting the necessary information more difficult [1]. The value that optimizes this choice is a

---

[1]Extracting information requires extracting energy from the beam.

few centimeters of plastic scintillator [2]. For our purposes the plastic scintillator chosen was Bicron BC-408. The beam momentum is then tuned to stop the pions at the desired position within the target.

This plastic scintillator is divided into three detectors. An upstream detector called B0, and two detectors near each other in the center of the detector [3] from the B0 counter. The first downstream detector is the degrader, which is composed of four fingers (see Figures 3.9 and 3.10). The second downstream detector is the target counter which is made of a different plastic scintillator BC-418.

The time of flight from the B0 to the degrader is used in beam particle identification (BID). The beam contains mostly positrons, muons, and pions. All of the beam particles have the same momentum but different masses, therefore the time of flight for each particle is different and can be used to determine the particle type. Figure 3.11 shows the relevant signals from the photomultiplier tubes attached to the B0 and degrader signal sum (taken from a data production run).

The top trace shows the signal from the B0 counter and the bottom shows the signal from the degrader. There are three distinct peaks in the B0 signal. Each represents the signal from a different particle type and the timing difference between them allows for particle identification. The particles arrive at the degrader in reverse mass order, so the solitary pulse is the positron signal. Then comes the muon and finally the pion signal. By aligning the trigger coincidence between B0 and degrader signals on the pion pulse we can select the trigger for beam pions.

Finally there is one additional feature of the degrader. The four fingers are wedged, two in the vertical direction and two in the horizontal direction. By comparing the light yield in each finger pair a measurement of the position of the beam particle in XY-space

---

[2]In fact the amount varied from run to run. In the final coniguration the value was as low as 8 mm preceeding the stopping target.

[3]The separation between the upstream counter and the degrader is about 4 m, producing a long flight time and hence an accurate measure of the pion momentum.

can be made with millimeter accuracy. As was discovered in developmental runs this information is invaluable and in fact needed to be better than the degrader was capable of measuring, thus precipitating the creation of a miniature time projection chamber. This device has spatial resolution an order of magnitude better in the drift direction (Y)!

The active target scintillating counter serves several roles. As the final beam line detector it is the stopping medium for our pions. Additionally the target is an active element. The signal is read out from a photomultiplier tube and used in several ways. Signals are sent directly to the system trigger as well as the data acquisition system. The target information is not used for trigger timing but rather for discrimination when enough energy is deposited in the target to likely be a pion. The target signal is digitized in the data acquisition system for complex waveform analysis later on (more on this to come).

3.3 Decay Detectors

The second set of detectors in the system are responsible for recording the information about the pion decay products. These detectors have several quantities to measure. Logically, we think in terms of particles traveling from the target to the calorimeter. We call this unit a *track* with the following components:

1. Direction,

2. Time,

3. Particle Type,

4. Energy.

The series of detectors are used to gather all of the information about the outgoing particles and then data analysis combines the measured signals from each detector into the different tracks. We will now step through each detector to discuss its role.

The first detector that the decay particles pass through is a series of two multi-wire proportional chambers (MWPCs). They are cylindrical in design and operate in the conventional manner (see Figure 3.14). Charged particles that pass through the chambers will ionize the magic gas inside leading to cascades along the anodes and influenced charge distributions on the cathodes. The geometrical layout of the device is such that anode and cathode hits are reconstructed by coincidence to support the claim of a passage of a charged particle through the chamber. None of the timing information is kept for this device but the charge magnitudes are recorded along with the wires where the charges was over a threshold. Careful analysis of these signals is able to determine, very precisely, the position of the particles as they pass. Therefore, this device is used to determine the direction of the track. Additionally the device is very low mass thus reducing the scattering in the detector.

Next the particles pass through a cylindrical plastic hodoscope segmented into 20 pieces and made of thin plastic scintillator (BC 408). The device is read out by photomultiplier tubes from both ends. The signal is split and sent to both the trigger system and the data acquisition system (where it is digitized for recording). This device contributes to the time of the track for charged partciles, for neutral particles that information must come from elsewhere. Due to the nature of the particles passing the detector (predominantly protons, positrons, and photons) this device can handle most of the particle identification duties. The positrons are minimum ionizing whereas the protons are not. The protons leave much more energy in the detector as well as a different characteristic shape (gaussian-like vs. landau-like). That information is used at particle identification time.

The last detector records the remaining energy of the particles, it is designed to capture the particles and as such is our main calorimeter. The PEN experiment's heart and soul is the 240 crystal CsI array. The crystals are arranged in a spherical geometry occupying a radius from 26 cm to 48 cm. The approximately spherical geometry is a truncated icosahedron further subdivided into mainly hexagonal crystals with 10 pentagonal crystals at each pre-truncation vertex. The calorimeter covers approximately a 3π solid angle and the two missing pentagonal modules are at the location where the beam enters the crystal ball and would exit if it were not stopped in the target. Figure 3.15 shows a computer model of the crystals without the requisite support structure.

Figures 3.17 and 3.18 show the crystal ball mounted and with photomultiplier readouts attached.

Figure 3.19 is a Mercator projection of the crystal modules.

The main purpose of the calorimeter is to measure the remaining energy of the particles. There are 11.89 radiation lengths so the containment is good for electrons, positrons, and photons. Protons are stopped easily by the calorimeter and good energy resolution is obtained for them as well. Additionally some directional and timing information is available from the segmentated calorimeter. In the case of photon tracks the timing must be taken from the calorimeter because no signal is left in the other detectors.

3.4 Putting it all together

Figure 3.20 is a beautiful picture showing the beam line as viewed from the just outside the target aperture. The yellow ring holds 20 PMTs for the hodoscope and the white cables are the readouts for the multi-wire proportional chambers.

Let us now step through what the signature of a radiative pion decay would look like.

For reference we represent Figure 3.21, which depicts the decay products of a radiative pion decay.

The incoming beam pion will leave a pulse in the B0 and degrader with the appropriate time signature. Then it will stop in the target. The blob represents the decay of the pion and the creation of the outgoing products. In this case we would expect two pulses, one for the pion and one for the energy lost by the positron as it exits the target. The photon would not produce any light in the target. Even if it did, that light would be coincident with the positron light and appear as one pulse. All information of the neutrino is lost to us. As Leo describes in his seminal work, "Neutrino detectors of high efficiency do not exist"[30]. The photon will shower in the calorimeter and deposit its energy. There is, of course, the chance the photon could convert to an electron-positron pair along the way, in which case some energy may be deposited as early as the target. Finally the positron will leave a pulse in the plastic hodoscope, along with hits in the MWPCs, and finally the positron will deposit its energy in the calorimeter.

Figure 3.9: A single degrader scintillating finger. The tip region is the scintillator and the rest is made up of a light guide.
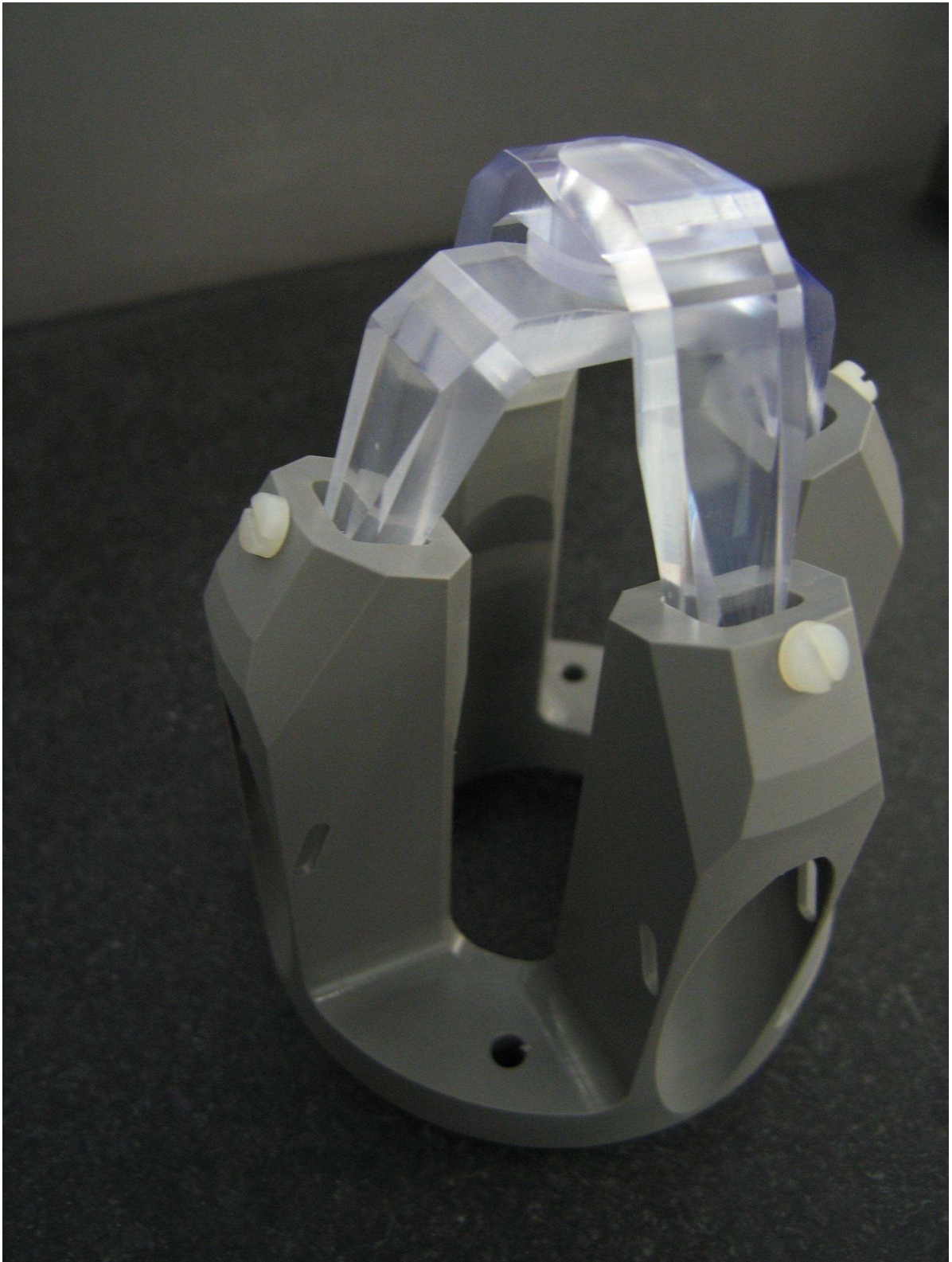
Figure 3.10: Assembled 4-finger degrader detector.
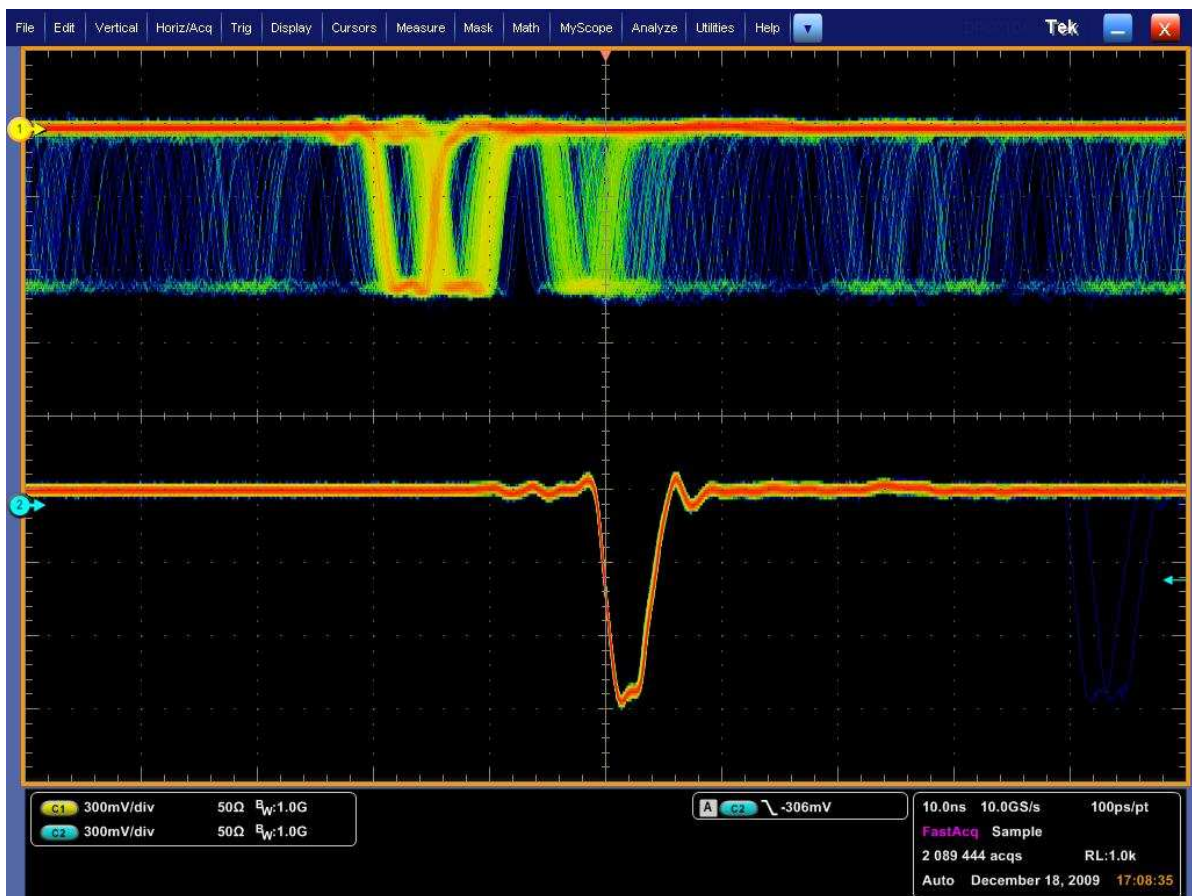
Figure 3.11: Top trace: B0 detector, Bottom trace: wedged degrader sum. The larger the time difference between the two traces the slower the particle (and as a result the most massive). Therefore we can identify the leftmost pulse as pions.

Figure 3.12: Wrapped and mounted active target counter. Behind it is an air light guide and then the photomultiplier tube.
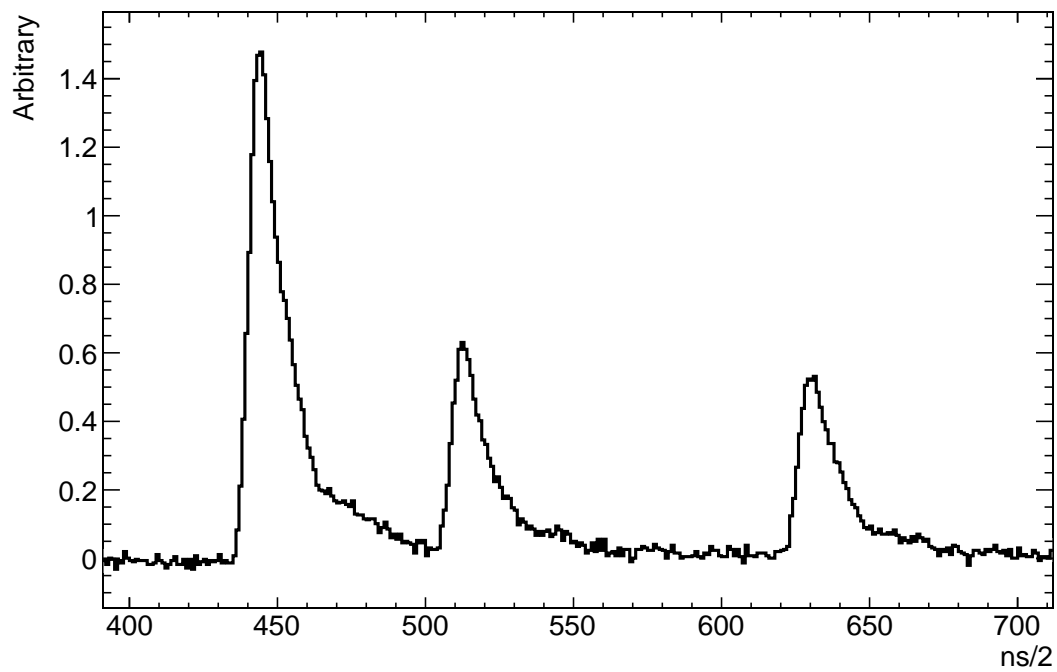
Figure 3.13: This plot shows a sample target waveform. This is a good candidate for a pion decaying into a muon and then the muon decaying into a positron.

Figure 3.14: The outer multi-wire proportional chamber. The white cables are the cathode signal readout.
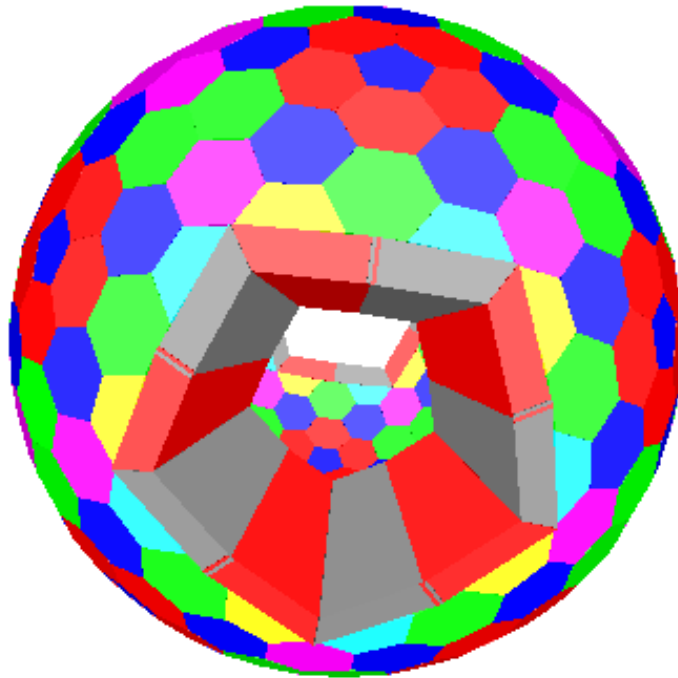
Figure 3.15: The PIBETA calorimeter color-coded by crystal. N.B. you can see through the opening to the inside rear of the calorimeter.
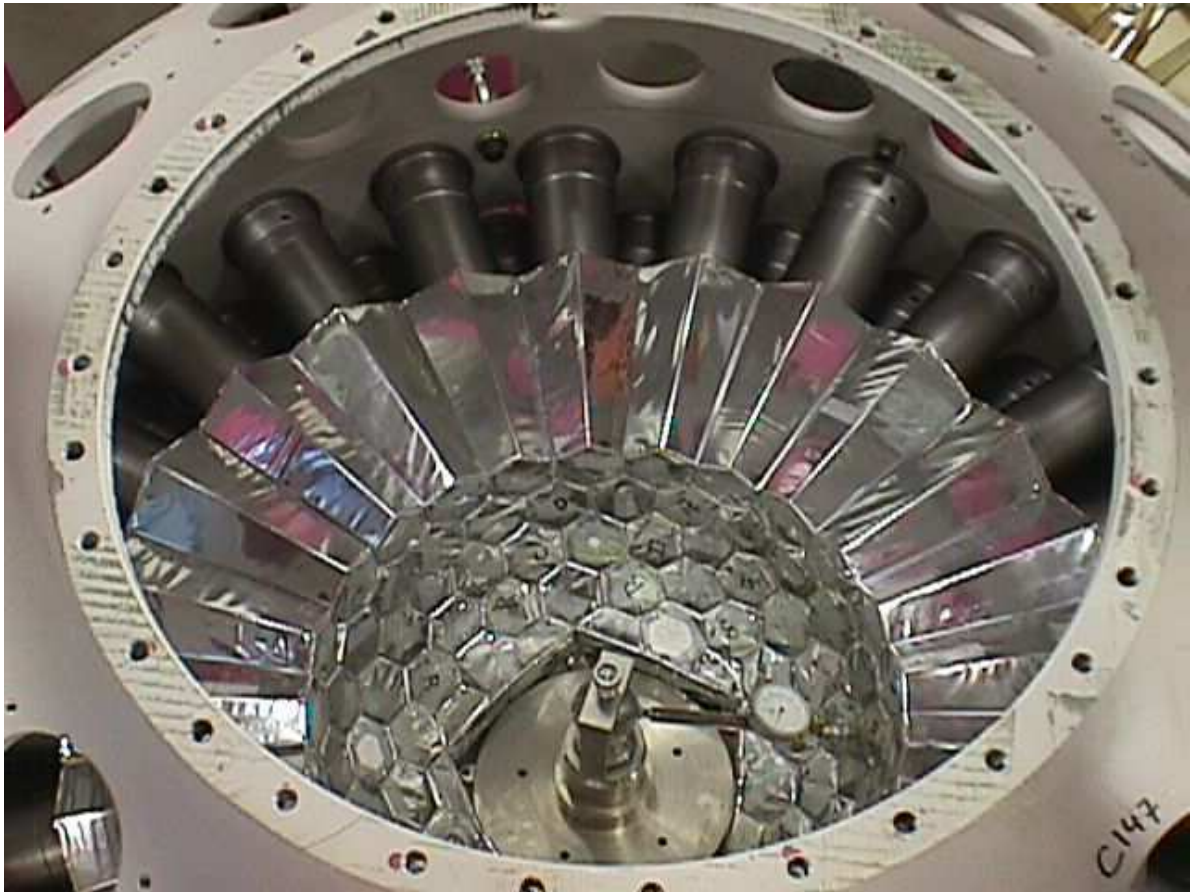
Figure 3.16: CsI Calorimeter under construction.

Figure 3.17: Close up of exterior of CsI crystal housing, the circles are PMT bases.
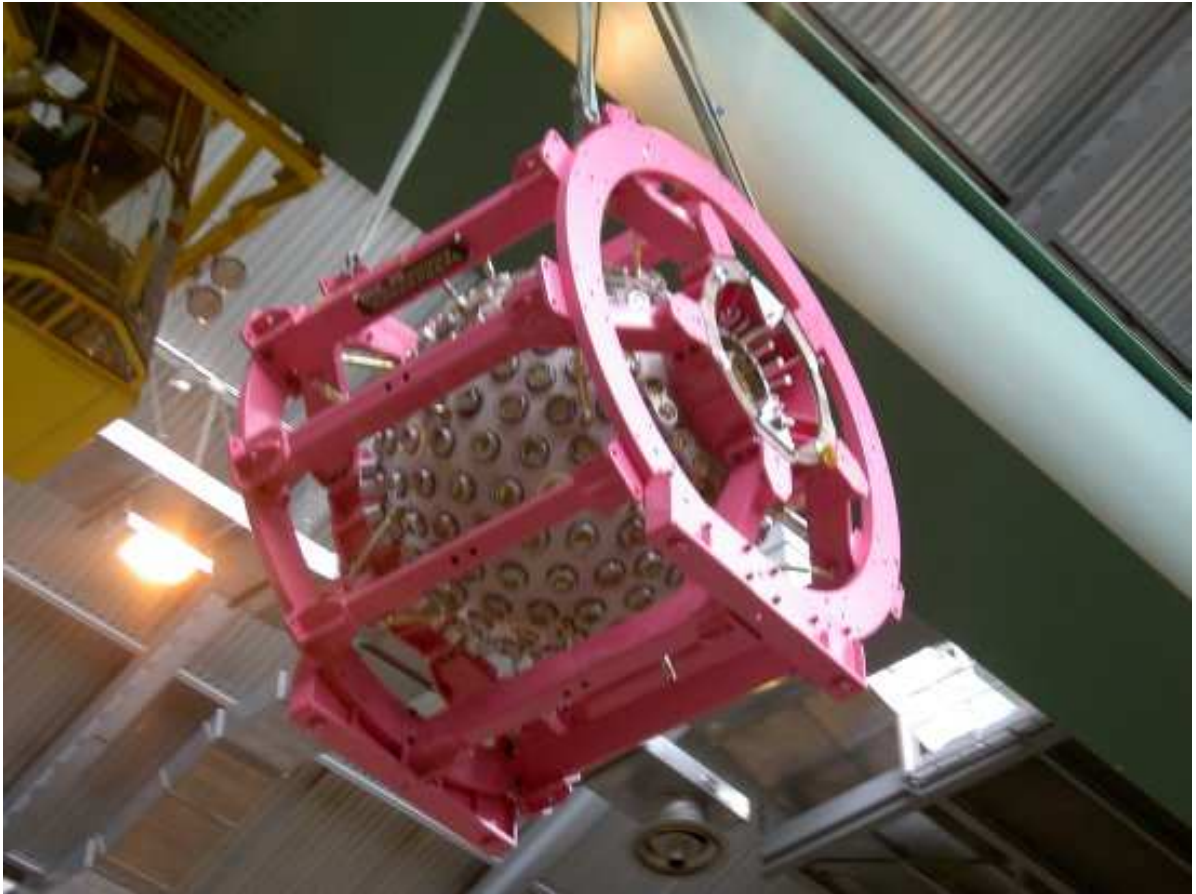
Figure 3.18: Full calorimeter with housing in transport.
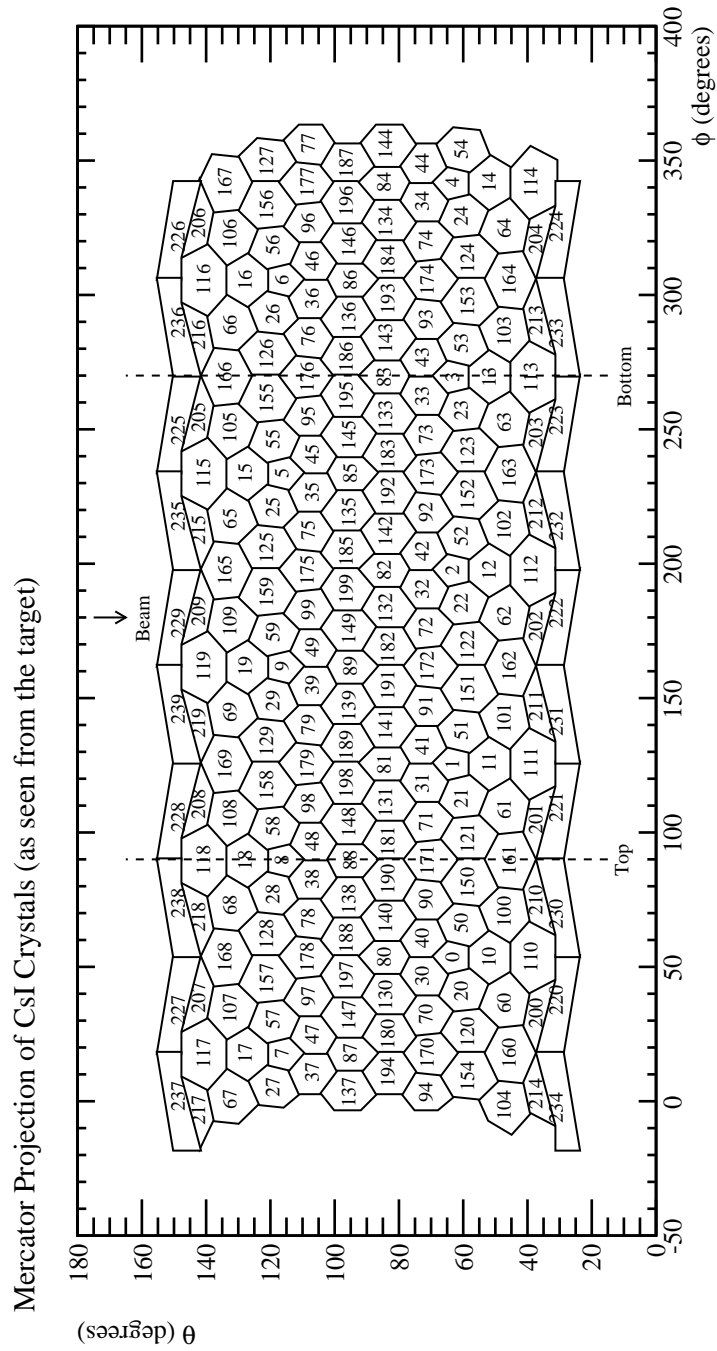
Figure 3.19: Mercator Projection of the 240 crystal CsI array.

Figure 3.20: Looking down the beam line, detector fully assembled
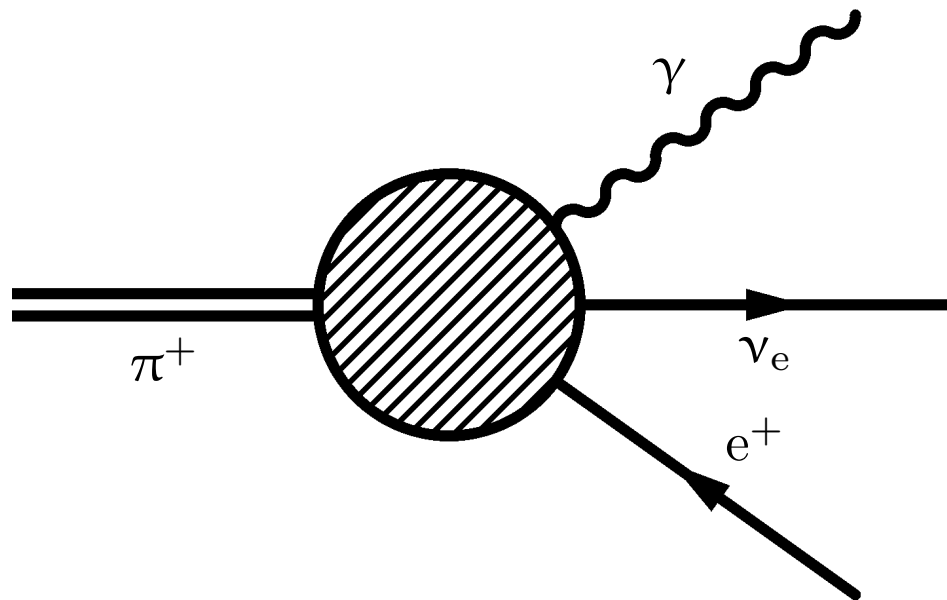
Figure 3.21: Feynman diagram representing the decay of a pion through the positron channel with a photon.
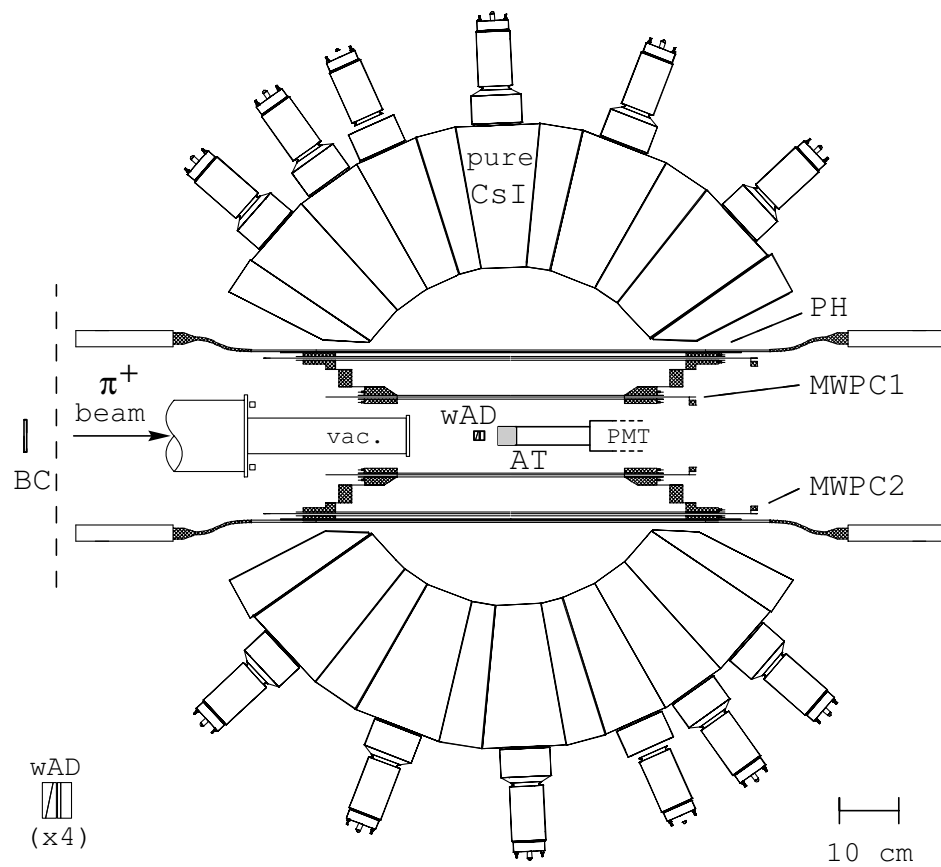
Figure 3.22: Schematic drawing of the assembled PEN detector.

Chapter 4

Event Trigger and Data Acquisition

The complement to the detector hardware system described in Chapter 3 is the system known as the *trigger*. The trigger is a series of fast decisions that ultimately decide whether the experiment records the signals produced in the detector hardware. It is vital to trigger the system correctly, otherwise signal events will be missed. By producing a clever trigger we can enhance the signal we are searching for. Furthermore a thorough understanding of the trigger comes from a thorough understanding of the physics involved. For the PEN experiment the relevant processes are listed:

- BR: $\pi \to e\nu$

    1. signal channel: $\pi \to e\nu$

    2. normalization channel: $\pi \to \mu\nu$

- BR: $\pi \to e\nu\gamma$

    1. signal channel: $\pi \to e\nu\gamma$

    2. normalization channel: $\pi \to e\nu$

The normalization processes are chosen to cancel as many systematic uncertainties from the measurement as possible. Determining the number of pion decays is very

difficult and obtaining the PEN goal[1] would be doubtful if that information was required. Therefore we chose to normalize the signal processes to other (more prevalent) decay modes of the pion. Given the list of processes we want to observe we can state the the PEN experimental trigger principles in three brief statements, which will be expanded upon in Sections 4.1-4.3.

1. We only record events where a pion stops in the target.

2. We only record events with early times relative to the pion stop.

3. We preferentially record events with large energies deposited in the calorimeter.

4.1   Stopped Beam Pions

The simplest trigger condition to understand is the requirement of a stopped beam pion. As previously discussed the first decision made in the design of the experiment is whether to used a stopped beam or a decay in flight. We chose stopped beam and as a result reap many benefits. Choosing the amount of material in the degrader allows for precise position of the stopped pion in the target. This added control simplifies the task of reconstructing secondary tracks. Additionally, it provides a very effective way to determine the inital time of the system. We refer to the moment the pions stops as t_0. In a similar fashion the resulting positron energy spectrum in the calorimeter is not complicated by additional (or missing) energy that would be introduced in boosting from the pion frame to the lab frame.

It is important to note the very complex signal of events where the pion decays in flight. It is inevitable that some pions will decay in our system before they stop. The majority of the pion decay in flight occurrences will not cause a trigger. However

---

[1] $\delta BR/BR = 5 \times 10^{-4}$

when the pion decays after entering the target a trigger is likely. For these events the characteristic time signature is distorted substantially and require special treatment in the analysis phase. This effect is most critical for the π_{2e} measurement and will not be discussed further in this document[2].

4.2   Early Decay Time

Measuring rare decay modes necessitates a trigger that rejects a large portion of pion decays. One tool at our disposal is the time signature of different processes. The $\pi_{2\mu}$ decay produces a muon which stops in our target[3]. Subsequently the muon will decay into a positron. However the muon lifetime is about 100 times longer than the pion lifetime. For our signal events there is no intermediate muon and therefore they have the time signature of the pion. This timing difference is represented graphically in Figure 4.1.

By only examining the early decay times relative to the pion stop time we greatly enhance the concentration of π_{2e} events in our sample. Additionally the $\pi_{2\mu}$ time signature in our detector is sufficiently large even at early times[4] that we will observe enough normalization events. The question then is what timing window to use.

We chose to trigger on events where the secondary particle was detected from $50\,\mathrm{ns}$ before the pion stop time to $250\,\mathrm{ns}$ after the pion stop time. The inclusion of the region before the pion stop is useful for understanding accidental backgrounds in the system. The decision to stop $250\,\mathrm{ns}$ after the pion stop time was made because it encompasses 99.99% of all signal events. This choice of timing cut produces an overall reduction in the amount of the $\pi_{2\mu}$ channel of one order of magnitude while having a negligible effect

---

[2]Details can be found in PEN experiment works detailing the π_{2e} measurement.
[3]Remember the muon has only $4.1\,\mathrm{MeV}$ of kinetic energy and penetrates only $1.7\,\mathrm{mm}$ in plastic.
[4]Remember that it picks up an enhancement of 10^4.
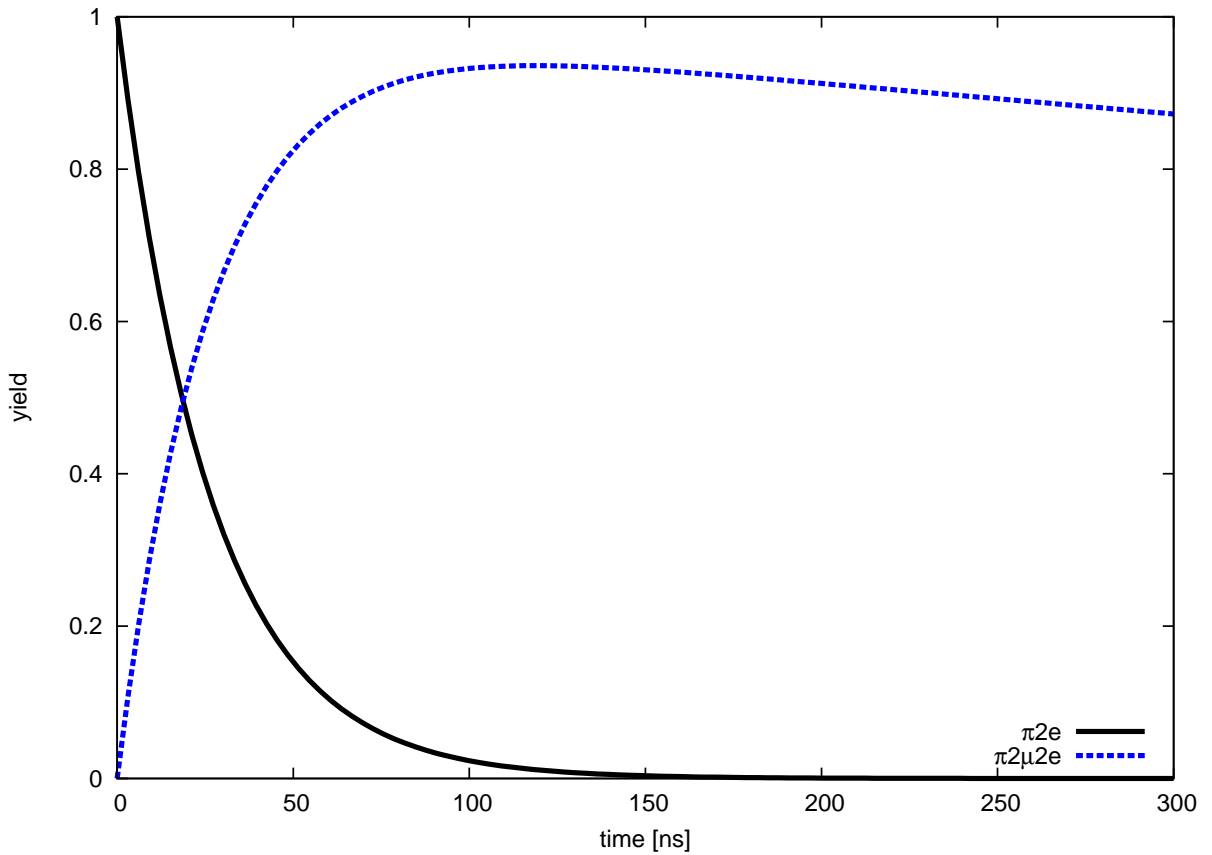
Figure 4.1: Characteristic time signatures for π_{2e} events (black) and $\pi_{2\mu}$ events (dashed blue).

on the signal process detection efficiency.

4.3   Large calorimeter energies

For our signal channels the secondary particle is a positron, in the case of the normalization channel it is also a positron but one from muon decay instead of pion decay. The energy spectra of the $\pi \rightarrow \mu \rightarrow e$ and $\pi \rightarrow e$ secondary particles differ substantially [25]. The Michel positron spectrum stops at around $52.8\,\text{MeV}$. The positrons from pion decay are mono-energetic at around $70\,\text{MeV}$[5]. The characteristic energy shapes including our calorimeter characteristic response are shown in Figure 4.2.

---

[5]This difference stems from the 3-body nature of the Michel decay and the 2-body decay of the pion.
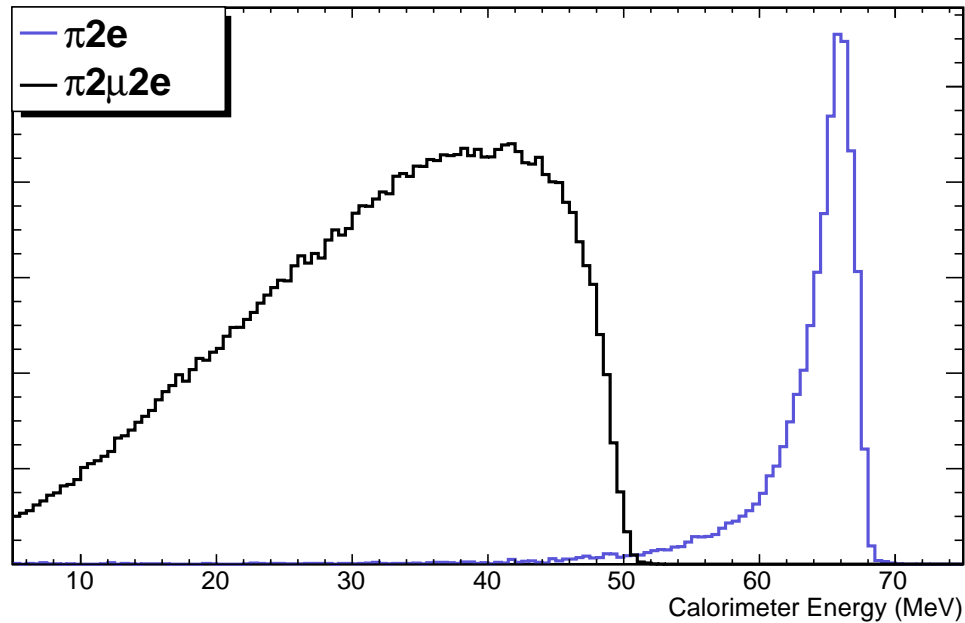
Figure 4.2: Characteristic energy signatures for π_{2e} events (blue) and $\pi_{2\mu}$ events (black).

We can exploit this energy response to preferentially select for signal channel events. The implementation is done by placing a threshold on the energy observed. However if that threshold is placed too high all of the $\pi_{2\mu}$ would be removed from our data set. That is unacceptable because we require those events for normalization. The answer to this puzzle is to have multiple triggers.

4.4 Physics Triggers

Since we are trying to observe several different processes with our apparatus it is only natural to have multiple trigger conditions. All of our observations are of pion decays so we stick with the stopped pion requirement. Additionally there are plenty of the normalization channel events in the early time window so we also impose that restriction on all of our triggers. Where we distinguish between the two events types with the most

discriminating power is the energy of the decay positron (E_{sp}). For events with a high E_{sp} we believe them to be mostly π_{2e}. Since that is our signal channel we want to record every one we can get our hands on. However for the events where E_{sp} is small the likelihood of the event being $\pi_{2\mu}$ is much greater than that of π_{2e}. We need some but not nearly all of them, therefore we employ a prescaling factor.

Prescaling means that we only record a fixed fraction of the events that produce a valid trigger. For the PEN configuration we ran with the $\pi_{2\mu}$ trigger prescaled by a factor of 64. Combined with the temporal acceptance of our trigger, which is about a factor of 10, we see a roughly 600 times reduction in the rate of the $\pi_{2\mu}$ signal. Since that signal comes in 10,000 times more frequently than our signal channel there is no problem taking a factor of 600 hit. This π_{2e} trigger is colloquially referred to as "LO" or "LOW", named for the energy threshold condition.

The signal trigger, π_{2e}, corresponds to events where the energy is above our threshold. The positioning of the threshold is critical. Figure 4.2 shows the characteristic response of the signal and normalization channel. We desire a threshold as low as possible so that we may capture as much of the blue curve as possible. However as the threshold is reduced the signal rate increases and the purity of the trigger goes down. We chose to place the threshold at the midpoint of the Michel positron edge. That way we recorded a large portion (about 98%) of our signal events in the signal trigger and maintained a high purity while allowing for some normalization events to enter[6]. This trigger was referred to colloquially as "HI" or "High".

---

[6]Actually a good thing from a systematic and calibration point of view.

4.5   Trigger Rates

Given the criteria detalied above our experimental trigger was constructed and data collection began. During the 2008 run the system ran with the same triggering hardware as the previous $\pi\beta$ experiment. Details on that information can be found in the dissertations of students from that experiment [31] and [32]. While the old trigger system was similar to what has been laid out in this chapter it was not optimized for PEN. For the 2009 and 2010 configurations of the experiment the trigger system was completely redesigned from scratch to adhere to these principles more closely.

Table 4.5 shows a summary of the processes that pass our experimental trigger and are written to file. The column labeled "Trigger" represents the trigger classification that the majority of those event types fall into. It is possible for an event to register a trigger class other than the one given in the table. The relative rates of the different phenomena are given before the prescaling factor is applied to any individual trigger.

Table 4.1: Rate and Trigger information for different processes.

Process	Data Role	Trigger	Rate (s^{-1})
$\pi \to e\nu$	signal	high	1
$\pi \to e\nu\gamma$	signal	high	<1
$\pi \to \mu\nu$	normalization	low	1,000
beam e^+	background	low	100
$\mu \to e$	background	low	100
$\pi + N$	background	high	100
$\pi(\mathbf{p} \neq 0) \to \mu\nu$	background	low	1
$\pi^+ \to \pi^0 e\nu$	background	high	0.0001

There is an additional constraint that is not motivated by the physics involved. The hardware used to read out the signals from the detectors requires time to do so. When the decision is made to read out an event from the system we are blind to incoming signals for an average of $1\,\mu$s. Therefore the maximum trigger rate the system can run at is 1 million events per second. However due to the amount of data being recorded the

computers can only handle a few hundred events per second. Therefore we are limited to a overall trigger rate of about 200 events per second. In practice the system ran at about 150 events per second.

4.6 Data Acquisition

The PEN Experiment data was acquired using the hardware detailed in chapter 3. That chapter only covers the hardware that produces signals. For every piece of signal producing hardware there are several pieces of equipment for the transportation, processing and storing of that information. All of the signals from the detector are channeled to a small room adjacent to the beam line known as the "electronics hut". Some of the information is sent via a delay sufficient for the trigger determination to be made, it should be understood that the trigger decision was optimized to be made as fast as reasonably achieveable. At numerous points the signals are split, amplified, and delayed; these processes occur so often in fact that the majority of those instances are omitted from this dissertation. We will begin by describing the software used to handle the storage of the data and then describe the components that digitize the signals from the detector and pass it along to the computer system for storage. The documentation of these systems is on the PEN webpage [33].

4.6.1 Software

Experiments of this scale require dedicated software for managing the data acquisition system. The predecessor experiment to PEN used the Maximum Integrated Data Acquisition System (MIDAS) [34]. Since that framework was already in place the PEN experiment elected to use the same system. Additionally several programs exist to facilitate the use of MIDAS. On the frontend machines code written in C++ uses MIDAS

libraries to control, read, and write the data. In fact the MIDAS system has its own file structure that was used extensively for all but the final stages of data analysis for PEN. Finally there were also a set of scripts that run on the various machines to monitor the system and automatically fix problems as they arose in data taking, for instance the different frontend computers may become missynchronized and there is a script to watch and repair that problem.

MIDAS

In use since 1993, MIDAS has been extensively tested and as a result is in widespread use at PSI and TRIUMF. As the name implies MIDAS has the ability to control the full experimental system [34]:

1. Hardware Control,

2. Slow System Control,

3. High order operations (run start, run stop, etc.),

4. Rudimentary Analysis (via a specialized C++ program),

5. Real time status updating.

It is also important to note that the simulation software also made use of the MIDAS libraries, as a result the simulation output was a file of identical form[7] to the measurement data files. Through the various computers the MIDAS system controlled CAMAC, VME, and FASTBUS crates, along with specialized high voltage systems. The end result was the the entire system could be monitored and controlled in real time through a single terminal. Taking advantage of the HTTP server capabilities of MIDAS enabled control of the system from anywhere the Internet reaches. Operating MIDAS system

---

[7]With the addition of the "divine" information.

is a complex task and therefore the PEN Collaboration employed a dedicated MIDAS coordinator.

Data File Structure

The MIDAS system divides the data runs into events. The data from each detector system is stored in banks which are written separately for each event. A PEN run contained about 200,000 events and took on the order of one hour to collect. Each event represents, in the ideal case, one pion stopping in the target and then the associated secondary particle depositing its energy in the calorimeter. Each bank contains information from a particular hardware system and information from a certain detector subsystem may have its information spread out over several banks, for example calorimeter energy (recorded by and ADC) in one bank and calorimeter times (recorded by a TDC) in another. Table 4.6.1 shows the details of the bank structure and its contents.

Table 4.2: PEN data banks and information summary.

Bank	Hardware	Information
TRIG	CAMAC	trigger bit
LTDC	FASTBUS TDC	time
PCOS	CAMAC	wire chamber wires
ZADC	FASTBUS ADC	calorimeter and hodoscope energy
RDGT	Acqiris Digitizer	beam line waveforms
ZCAT	FASTBUS ADC	wire chamber cathode energy

On a note of personal interest to the author we have included a schematic depiction (Figures 4.3 4.4) of the process by which data is written to a MIDAS file. This process is necessary to understand in order to write a MIDAS file, which is necessary to conduct a proper simulation. These figures detail the position and size of the pointers used in the C++ code at every stage in the data file writing process.
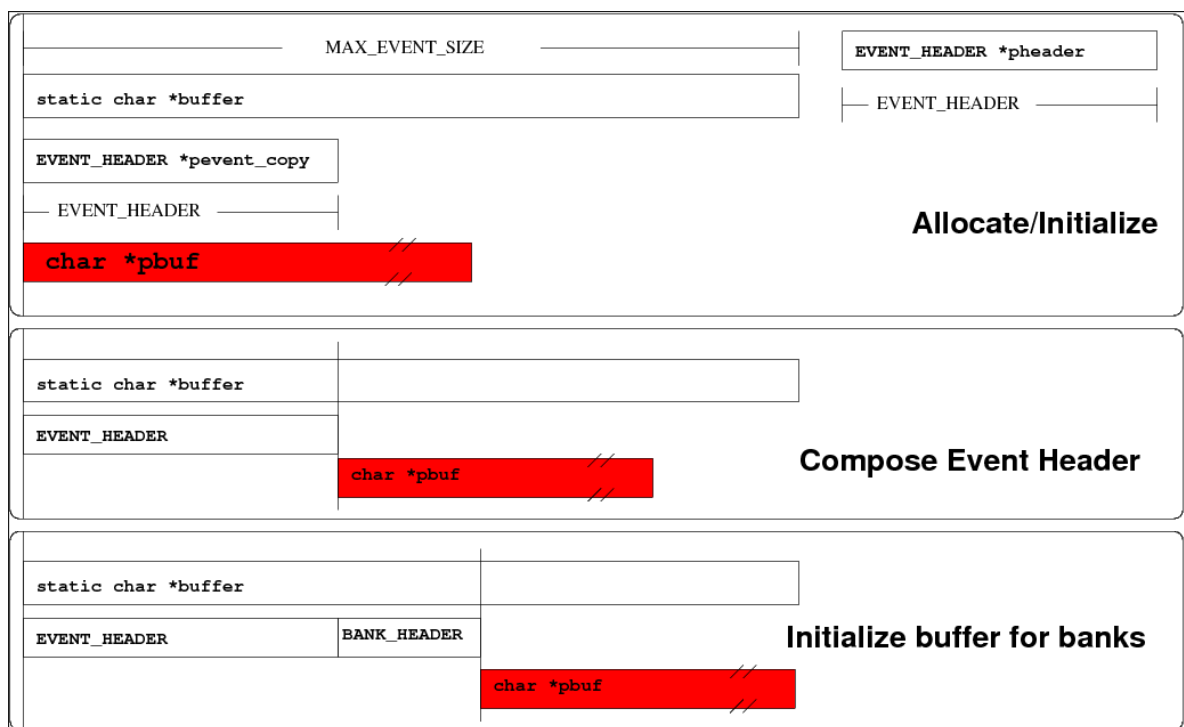
Figure 4.3: MIDAS file writing: Event initialization stage.

Figure 4.4: MIDAS file writing: Bank recording stage.

Part II

University of Virginia

Charlottesville, Virginia

United States of America

Chapter 5

Geant4 Simulation of the PEN Detector

Simulations serve different purposes at different stages of an experiment's life. For a mature experiment like PEN, a simulation represents the most complete understanding of the experimental system and the relevant physics processes. At this stage the simulation is comprehensive. It covers every aspect of the experiment from the tiniest features of detector signals to the exact format of the data files. For the PEN experiment we chose the following as the guiding principle for our simulation: **to the outside observer a simulation data file should be indistinguishable from a measurement data file**. As a result the analysis protocols are identical for simulation and measurement data. There is one exception[1] to this rule, the simulation data reports actual units (MeV, ns, etc.) whereas the measurement data reports pseudo "units" ("MeV, "ns",etc.). This distinction is important; the simulation values are used to calibrate the measurement data to the true SI unit system.

---

[1]Actually two exceptions, the second is the presence of the "divine" information.

5.1   Motivation

Given the simulation philosophy already described, the simulation serves several purposes. First and foremost, it lends great credibility to everything the collaboration says about the experiment. Since every feature of the experiment is accounted for in the simulation there is a rigorous accounting of each detail. It demonstrates that the nuances of the experiment have been measured and understood. Additionally this great confidence in the experiment simulation allows for study of the unknown.

The simulation is used to explain the data collected but since it is a faithful representation we can then ask other questions that are unanswerable with measurement data. For instance we may ask, "what percentage of pi2e decays in the target of our experiment produce triggers?" That question is fundamental to understanding the acceptance of our detector. Educated estimates can be made without the simulation but with it we can do much better. Of course it would be arrogant to proclaim absolute knowledge of the system, therefore the application of simulation data to analyze the unseen events introduces systematic errors into the experiment result. There is nothing wrong with this uncertainty. In fact the ability to faithfully represent the systematic uncertainty is beneficial for the experiment understanding as a whole.

Another feature that the simulation will give some insight on is the response of the crystal ball style CsI calorimeter. There is an inevitable low energy tail in the signal channel energy response emmanating from the leakage of the electromagnetic shower. That tail is buried beneath the signal from the normalization channel of the experiment (Michel energy spectrum). To access the precision our experiment aims for it is vital to know the shape of this tail.

This chapter will step through each of the detector systems in the experiment and demonstrate the simulation techniques as well as calibrations. Finally it will conclude with the relevant results of the simulation, acceptance calculations and full pi2e positron

energy spectrum.

5.2   Detector Systems

Then 2008 configuration of the PEN experiment consisted of three classes of detectors. The specifications are outlined in chapter 3 and previous publications already referenced. Those systems are summarized as follows:

1. CsI Crystal and Photomultiplier Tube,

2. Plastic Scintillator and Photomultiplier Tube,

3. Multi Wire Proportional Chamber.

Each separate system requires a different treatment in simulation. The first two share some features while the MPWC is a different animal. The first two systems convert kinetic energy to light via the process of scintillation and subsequently produce analog voltage signals via the photomultiplier tubes. The characteristic signal shape depends on the nuances of each individual element. However, due to the information we desire from each system, the readout occurs with different hardware and as a result the simulation techniques vary depending on the readout procedure. In some instances the analog detector signals are only used to determine a time. Other times they are integrated, and some times the entire signal is digitized and stored for further analysis. As a result we employ different tactics to simulate the detector signals, in some instances using multiple techniques for the same detector if its information is used in multiple ways. The third system is the most complex. The PEN multi-wire proportional chambers have undergone extensive study [35], but have not been simulated in great detail. Building upon MWPC literature [36] we developed a specialized technique for faithfully representing the critical features of our MWPCs.

As outlined in Chapter 4, the data file structure is broken down into banks. Each bank contains one type of information read out by one hardware system (e.g., ZADC bank records calorimeter energy readout by FASTBUS ADC). We will go through the banks and outline their roles, data collection techniques and features, and then explain the simulation procedure and calibration techniques. Special attention was paid to the TRIG bank because it plays the principal role in the determination of trigger acceptances.

5.2.1 Detector Geometry

The PEN experiment geometry is incorporated into GEANT4 [37] using ROOT. As with all of our software the code can be found in the PEN experiment repository on the experiment's content management system (CMS). This detector geometry is comprehensive and covers everything from the upstream beam counter to the CsI crystals. The passive wrapping materials for each detector are included as well. The principal work to produce the geometry file was done by our collaborators from Dubna. As the need arose additional revisions were made to the detector geometry.

5.2.2 Beam Profile

All of the information used to model the beam profile in the simulation software comes from in situ measurements. The relevant inputs include the beam momentum as well as the initial position of the pions[2]. To determine the beam momentum we measured the time of flight of positrons from the upstream counter to the degrader (11.97 ns). That value was compared with the time of flight for pions over the same flight path (24.04 ns). The comparison of these times along with the known thickness of the upstream counter

---

[2]Due to the excellent ability of the analysis code to discriminate against beam muons and beam positrons we only simulated the beam pions.

yields an initial beam momentum of 83.3 MeV/c. To cross check this value we calculated the range of the pions in our plastic scintillators (B0, degrader, and target). This value was then compared to the position of secondary track's emanation for perpendicular tracks ($MWPC1_z = MWPC2_z$). The results of this matching are shown later in Figure 5.10. The second input is the initial position of the beam particles. The upper right panel of Figure 5.9 shows the best measurement of the XY-plane distribution of beam particles as they enter the wedged degrader. That distribution was used to develop a seed function for the distribution of the beam particles in the simulation. The results after calibration are shown in the bottom two panels of the same figure.

5.3 Software

The amount of interaction between matter and fundamental particles in our experiment is simulated by GEANT4. We have chosen to implement version 4.9.0.p02. This version uses C++ and therefore is compatible with ROOT as well as our MIDAS data acquisition system. For all references to energy depositions, timings, and other related things the information was readout directly from GEANT4. I will spare the reader the details of GEANT4 classes but will mention that the full source code is posted through our content management system and version controlled with SVN[3]. The structure of the simulation follows standard practice. The procedure outlined below is illustrated in Figure 5.1 along with the measurement data procedure for comparison. There are two stand alone programs that encompass the simulation software suite. The first uses GEANT4 and it contains the detector geometry for the experiment. This program tracks events starting with a pion traveling down the beam line and stopping in the target followed by the

---

[3]anton.phys.virginia.edu/pen_cms

subsequent decay and secondary particle[4]. That bank contains the "divine" information relating to the event. The events are generated in the decay basis of the pion and stored in files based on pion decay channel[5].

That information is then passed to the second stage of the simulation software. This stage is called the frontend because it performs the same function as the frontend computers do in the measurement data collection process. This program is responsible for taking the simulation information (stored in the GSIM bank) and producing the realistic bank structure of a measurement MIDAS file. All of the detector response functions are contained here[6]. Chief among them is the TRIG bank, the bank containing the trigger information. Finally this program records the banks along with the GSIM bank into a file which at that point resembles a measurement data file. That file may then be handled in an identical fashion to a measurement data file during all subsequent analyses. There are three exceptions to this rule.

The run by run dependence of our experiment is removed with a series of parameters contained in codb files[7]. Those corrections are applied to the system before the simulation is calibrated. Therefore they are not necessary for the simulation analysis. The second exception is the presence of the current detector information at the beginning of each measurement MIDAS file. Since the simulation code is not taken in a live fashion, it is unnecessary to record the carry over information from one run to the next. The reason for removing this information from the simulation MIDAS file is disk space. There is a substantial amount of information that is not necessary. That information is used live when running the experiment but does not play a role in data analysis.

---

[4]Of course other things may happen along the way such as pion decaying in flight or scattering, rest assured those events are recorded as well.

[5]This detail is important and must be understood because the mapping from decay basis to trigger basis is non-diagonal.

[6]For the matching of the behavior of the plastic hodoscope detector it was necesarry to incorporate calculations at the step level. Those are found in the GEANT4 code out of necessity.

[7]codb: calibrated online data base, a peculiarity of MIDAS.

Therefore it is suppressed to save disk space. The final exception stems from the fact that the simulation data is measured in SI units where as the measurment data is not. Substantial work goes into correcting the values of the measurement data to report in SI units[8]. That calibration is done using the SI information from the simulated data and therefore those corrections are not necessary for the simulated data.

These figures will show identical distributions from measurement data and simulation data (when useful). In each the simulation data will be shown in green[9] and the measurement data in black. The histograms shown were produced with identical analysis routines for both the sets of data. The only differences are in the drawing of the data on the page. Now we will proceed to describe each bank in the MIDAS file and the assosciated production techniques.

5.3.1   PCOS

This bank contains the information from the anode wires in the MWPC. There are two concentric circles made up of longitudinal wires (one circle for each chamber). When charged particles pass through the chamber they ionize the gas. The potential bias then causes the electrons to drift towards the wires where ultimately they collect causing an avalanche and signal on the wire. That signal is discriminated and if it passes above threshold the system records a hit. That is all the PCOS bank contains, just a record of wires with a "hit". The signal is discriminated before storing in the bank, therefore the bank contains a boolean array with simple one dimensional scheme for encoding the wire number.

For the simulation side we collect the ionized energy (GEANT4) and calculate the

---

[8]e.g.: The calorimeter analysis is written to convert the reported energy in MeV (instead of adc channels), with the scale for that energy coming from matching the "line shapes" to simulated values.

[9]If it is useful to present the divine simulation values they will be shown in red. For multi-dimensional plots this convention is not applicable so please pay careful attention to the captions.

nearest wire on a step by step basis. At the end of an event we add up all of the ionization energy on a wire and if that is over the threshold a hit is recorded. Currently the threshold is set at $0\,eV$. Since the wire chamber does not play a role in the trigger system for the experiment there is little impact on the acceptance of the system from this artificially low threshold. There is room for further study and future work will include a treatment of the efficiency of the MWPC anode wires.

5.3.2 ZCAT

This bank encodes the information concerning energy deposited on the cathode strips in the MWPCs. A complicated system to simulate properly, the cathodes from our multi-wire proportional chambers (MWPC) require a careful treatment. The work on this system relied heavily on several sources: [38] [36] for charge influence modeling, and [39] and [35] for detailed behavior of the MWPCs themselves.

The first step in simulating the cathode system is understanding the readout system. It was the same as the ZADC bank, a series of FASTBUS ADC modules. However the energy deposition occurs through an inductive process. As covered in Subsection 5.3.1, GEANT4 records the ionization energy as particles move through the gas medium of the MWPCs. The charge is propagated to an anode wire. At this point the published charge influence models are applied to determine which cathode strips produce a signal [38] [36]. Figure 5.2 shows the comparison between PEN measurement data and theory. The amount of charge influencing the cathodes must match the charge of the anode avalanche. The cathode strips closer to the avalanche point are influenced more than those further away. After the event is complete at the frontend level the charge influencing a strip is converted to ADC channels. After appropriate detector response uncertainty is added the pedestal signal is applied.

For review here are the following steps for the simulation of the MWPC:

1. Step by step – Ionization energy deposition is recorded,

2. Ionization energy propagated to the nearest anode wire,

3. Influence functions model the charge deposited on the cathode strips,

4. Event by event – anode charge accumulation checked, boolean set if over threshold (PCOS),

5. Charge on each strip summed,

6. Each strip is smeared with the characteristic response and the energy recorded (ZCAT).

Returning to the details of the MWPC simulation: Figures 5.3 and 5.4 show the mapping of cathode strip to anode wire. These plots were produced using identical analysis software. Only certain combinations of wire and strip will produce a coincidence and therefore this picture is a good measure of the accuracy of the mapping. It demonstrates that the simulation properly maps the XYZ-space into the wire–strip-space.

5.3.3 RDGT

This bank contains the information digitized by the Acqiris waveform digitizer at a sampling rate is $2\,$GHz. The upstream beam counter, the wedged degrader, and the target counter are the detectors read out by this detector.

A typical event contains a pion pulse in the B0 along with one pulse for each of the degrader wedges, and finally a pulse for the pion, muon, and positron in the target. Figure 5.5 shows a typical pulse produced from the left and right degrader wedges. The task at hand was to simulate these signals in a reliable way.

Ultimately the pulses are analyzed and two pieces of information are extracted, time and energy. Therefore from a simulation standpoint we should use GEANT4 to tell us

the time and energy of a particular event. Then in the frontend stage of the simulation suite we can use those values as inputs to determine how to mimic the detector response. We settled on a procedure where the waveforms were sampled from measurement data and then interpolated to a binning of 500 fs. We then place these interpolated waveforms into the RDGT bank according to the time determined from GEANT4. The size of the interpolation binning required was small enough not to introduce systematic error. Since we observe a net uncertainty on the order of 100 ps in the measurement data waveforms we decided the interpolation necessary would be 100 times smaller [40]. Finally the sampled pulses were scaled to the recorded energy as given from GEANT4. The particles passing through these detectors include predominantly: pions, muons, positrons, and protons. Studies to be published demonstrated that the characteristic pulse shape was independent of particle type or energy [40]. That work was performed before I joined the collaboration. We now present Figure 5.6 which shows the same information as Figure 5.5 except produced by the simulation suite (still analyzed with the same code).

Moving onto higher level work done on this bank we now look a the results of the analyzer software. Figure 5.7 shows the detector response for the four degrader wedges[10].

However the story is not complete. In addition not only must each finger be calibrated correctly but also the left-right sum, and top-bottom sum, and the whole degrader sum must match simultaneously. Those distributions are shown in Figures 5.8 and 5.9, respectively.

Once the sums are within tolerances then the beam profile can be checked. The wedged degrader is a position-sensitive device and the left-right fingers measure the horizontal (x) position of the pion and the top-bottom fingers measure the vertical (y) position of the pion. Figure 5.9 shows the agreement between the simulation and

---

[10]As a reminder for all of these pictures: red represents divine simulation data, green represents simulation data, and black represents measurement data (and the green and black are produced using identical analysis algorithms).

measurement data.

The analysis proceeds to the prediction of the stopping position in (z) of the pion. Figure 5.10 shows the relevant information for the determination of the beam pion stopping position. The time of flight (TOF) is measured from the upstream (B0) counter to the wedged degrader and is shown in the rightmost panel. That information is used to determine the energy of the pion prior to entering the degrader. Then the degrader energy is subtracted and used to determine the energy of the pion prior to entering the target. That energy is converted into the stopping position of the pion using the formula

$$\text{range} = \left(\frac{\mathrm{p}_\pi}{64.56} \right)^{3.5}. \tag{5.1}$$

Where range is the penetration distance in centimeters and p is the momentum of the pion in MeV. The computation of stopping position is shown in the leftmost panel.

Clearly there is still some room for improvement here. While the degrader responses look great in the bulk there are still some discrepancies at the wedge by wedge level. In particular the right wedge has a strange shape that is not fully explained by the simulation. Work by the collaboration is ongoing on this front and recent work has shown that the calibration of the target counter position is accurate only to the $0.5\,\text{mm}$ level. Furthermore the calibration of the degrader energies was only done in a rough fashion. Lots of careful study is needed here. As a result the simulation effort to match these responses will have to be completely repeated when the PEN calibrations are complete.

5.3.4   ZADC

This bank contains the ADC values for the CsI calorimeter and the plastic hodoscope. By far this bank receives the most scrutiny. The simulation begins with the GEANT4

energy deposition values in each calorimeter and hodoscope module. For the colrimeter modules it is just the total energy deposited, however for the hodoscope modules a step by step correction must be applied for faithful representation of the energy deposition. The reason is the shape of the plastic. The modules are long and thin and the light has to travel 10's of cm in some cases. The scintillation light is attenuated and we observe a considerable difference in light collection depending on the z-position of the energy deposition. Fortunately this behavior is well understood and can be modeled with a simple exponential function. The formula used is as follows:

$$2 \times \text{Energy Reported} = \text{EDEP}_{\text{step}} \times \exp\left(-\frac{|z + L|}{\lambda}\right) \tag{5.2}$$

$$2 \times \text{Energy Reported} = \text{EDEP}_{\text{step}} \times \exp\left(-\frac{|L - z|}{\lambda}\right) \tag{5.3}$$

Where $\text{EDEP}_{\text{step}}$ is the energy deposited in the step measured by GEANT4, z is the position of the energy deposition, L is the length of the hodoscope module, and λ is the light attenuation length of each module measured from measurement data. The different equations represent the upstream or downstream photomultiplier tube respectively. For the PH the only correction left before the energy is recorded in the bank is the Poisson smearing which accounts for the photoelectron statistics.

We now turn to the treatment of the CsI calorimeter. There are 240 crystals that make up the PEN calorimeter. Each crystal is not quite the same and requires individual calibration both in the measurment data and the simulation data. The technique we employ is to adjust the measurement data to be uniform crystal by crystal and run by run. Then we calibrate the crystal energy response to the value of the simulation data. There are two main features used for this calibration, the Michel energy spectrum and the π_{2e} peak. Once the energies match we then proceed to determine the response of each crystal. That information is recorded in terms of a resolution measured at the π_{2e}

peak. The energy recorded by GEANT4 is used as the starting point for each crystal. We then apply Poisson smearing with a scale of 70 photoelectrons per MeV. To account for individual crystal resolutions the photoelectrons per MeV was modified by the measured crystal resolutions [11].

There is an additional complexity that creeps in stemming from the size of typical showers in the calorimeter. The typical shower hits several crystals. Therefore when we work to calibrate the energy in the calorimeter if we wish to observe physics structures like the Michel spectrum we must look at clumps of crystals as opposed to individual crystals. The clumps[12] are dynamic and may be centered around any crystal. We use the crystal with the most energy deposited as the center and sum all of the surrounding crystals. Then the calibration is applied to that value with the index of the central crystal.

Furthermore the cylindrical nature of our hodoscope and target adds another wrinkle. Depending on the polar angle the track is on a different amount of energy is lost in the target and hodoscope. It is therefore necessary to calibrate the CsI calorimeter using the full secondary positron energy. This energy is a sum of the target counter, the plastic hodoscope, and the relevant CsI signal (E_{sp}). The energy calibration of the target and hodoscope must be completed before the calorimeter energy response matching can be undertaken. Fortunately we have already detailed those systems and may proceed remembering that we are now looking at the full reconstructed particle energy and not just the CsI calorimeter.

---

[11]pen.phys.virginia.edu/restricted/crystal_resolutions.txt

[12]The routines that make this determination were extensively developed by the PIBETA collaboration and are explained in detail in [31] and [32].

5.3.5   LTDC

This bank is responsible for encoding the timing information of different detectors. The beam line elements have the full analog signal digitized and subsequent analysis extracts their times. Therefore the TDC values from those detectors are not used in our analysis. As a result the important timing information in the TDC modules is from two systems only: the CsI calorimeter and the plastic hodoscope. Due to inefficiencies in the CAMAC modules the trigger bit information is duplicated and sent to the TDCs.

The method for determining the timing of each signal is simple. GEANT4 records the global time when energy is first deposited in the detector for each element. Then at the end of the event all of those times are recorded with the appropriate offset. The inquiring mind may ask about energy dependent effects. To be sure, there is an requisite energy threshold for recording the timing information. This threshold mirrors the discriminator placed on the signals before they are sent to the TDCs in the real experiment. The second half of the energy question is about what is commonly called "walk"[13] . The simulated data are devoid of walk effects. The measurement data are corrected for walk effects and the correction applied to the simulation data for walk effects is nil. This difference between simulation and measurement analysis does not provide a significant contribution to the systematic error budget. The precision of the TDCs and our understanding of walk correction is good enough that it does not contribute to systematic concerns.

There is one more piece to the puzzle. The measurement data also include statistical fluctuations and other higher order effects. There is no need to control each of them individually. For the simulated data Gaussian smearing is applied to the CsI and PH

---

[13]Jargon time: The walk in a signal refers to the *apparent* energy dependent nature of signal time. What is going on is that the timing information is extracted from a discriminated analog signal. When the analog signal size varies the time to cross the discriminator threshold also changes. Hence the term "walk", the timing appears to "walk" around.

times before they are recorded. The weight of this smearing was adjusted to match the characteristic signal response widths of the individual detectors.

5.4 Results

5.4.1 TRIG Bank and Acceptances

The most important bank in the data file is the trigger bank. It is by far the most difficult bank to simulate properly.

The TRIG bank is the smallest bank, it contains only one word encoding the information as to which trigger fired. Relevant for this study are two triggers, HI and LO. Those designations refer to the amount of energy deposited in the CsI calorimeter as elaborated upon in Chapter 4. The importance of this bank is tied up in the calculation of experimental acceptances. The data analysis of the experiment aims to measure the number of signal events and the number of normalization events in our data set. For review we repeat Table 4.5.

Table 5.1: Summary of processes and important information

Process	Data Role	Trigger	Rate (Hz)	Sim
$\pi \to e\nu$	signal	high	1	Y
$\pi \to e\nu\gamma$	signal	high	<1	Y
$\pi \to \mu\nu$	normalization	low	1,000	Y
beam e^+	background	low	100	N
$\mu \to e$	background	low	100	N
$\pi + N$	background	high	100	Y
$\pi(\mathbf{p} \neq 0) \to \mu\nu$	background	low	1	Y
$\pi^+ \to \pi^0 e\nu$	background	high	0.0001	Y

This time there is an extra column, representing whether the channel is reproduced in the simulation or not. As mentioned in Section 5.1 the main function of the simulation is to measure the unobserved. Strictly only the signal and normalization channels are

necessary for the work in the acceptance calculation. However there is a great utility in the study of the background processes, especially in the case where the background processes masquerade as signal processes from the point of view of the analysis software. Often a valid signal or normalization event does not create a trigger. This can happen for a number of reasons, the most common of which is simply the decay particle missing the CsI calorimeter (one piece of geometrical acceptance). Other possibilities include temporal acceptance and detector efficiency. If the TRIG bank is simulated properly then the determination of the acceptance is nothing more than a counting exercise.

The procedure is to run the simulation data through the identical analysis code as the measurement data. However this time the final number of observed signal and normalization events can be compared with the initial number produced in the simulation. That ratio is then the measure of the detector acceptance. The PEN experiment takes advantage of the full simulation from initial state pions all the way to the secondary particle. By ensuring faithful representation of each system along the way (and of course the TRIG bank) we can wrap the acceptance calculation into one number. This technique has the added benefit of simplifying the normalization conditions for each step. Furthermore since the simulation of the initial pion is identical for each process all possible errors in that regime cancel.

There are two subtle points that require careful treatment. The first is that the simulation produces events in the pion decay channel basis. That is to say a simulated event begins with a pion where the decay mode is fixed. However events are recorded by the PEN experiment in the trigger basis. Equation 5.4 represents these ideas mathematically[14]. As a result of the prescaling factor imposed on the low threshold trigger we must simulate far more of those type of events than we need. One cannot simply generate "low trigger" events. We must go through the simulation process followed by

---

[14]It is important to note that these acceptance numbers are blinded. Broad features may be interpreted, but the details are not to be closely examined.

the event rejection process.

$$
\begin{pmatrix} \#pi2e & \#pi2m & \#prompt & \#DIF \end{pmatrix}
\begin{pmatrix} 0.102 & 0.772 \\ 0.869 & 0.004 \\ 0.206 & 0.026 \\ 0.148 & 0.005 \end{pmatrix}
= \begin{pmatrix} \#lo \\ \#hi \end{pmatrix}
\tag{5.4}
$$

Secondly there is the problem of infrared divergence. Recalling from Chapter 2 the bremstrahlungh process decay rate is divergent at low photon energies. As a result an cutoff must be applied. Furthermore the simulation data cannot be generated in proportion to the actual yield because to produce one event in the SD_+ region would require millions in the bremstrahlung region. Therefore the events are generated for simulation data uniformly in xy-space[15]. To extract physics results from simulation data the decay rate weight must be applied. This weighting must be properly accounted for the acceptances to be valid.

---

[15]Recalling x is photon energy and y is positron energy not the physical position coordinates of our detector.

MEASUREMENT   SIMULATION
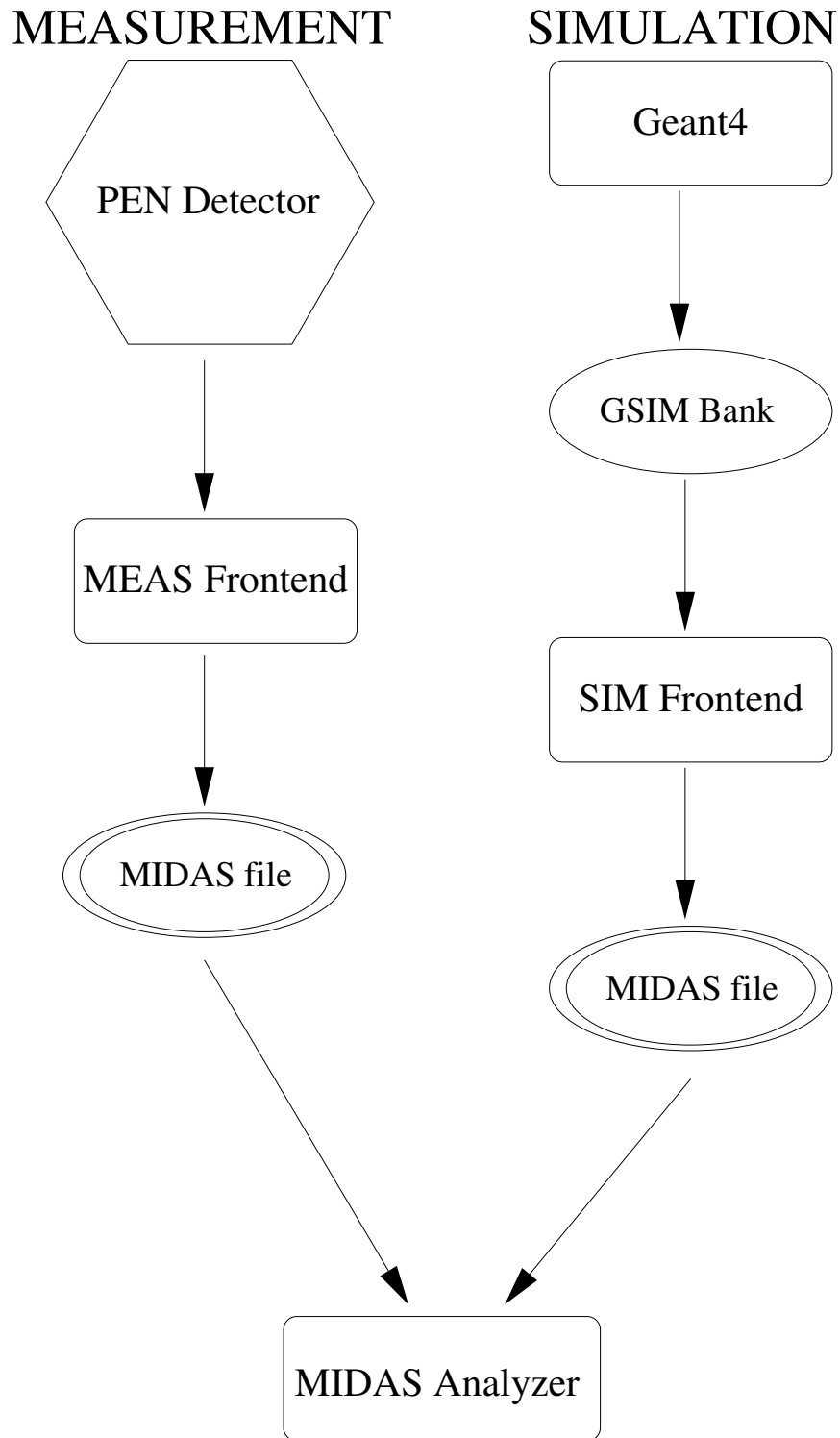
Figure 5.1: Data flow for both measurement and simulation data. Each shape represents a different object: Hexagons – physical systems, Rectangles – computer programs, and Ovals – data files.
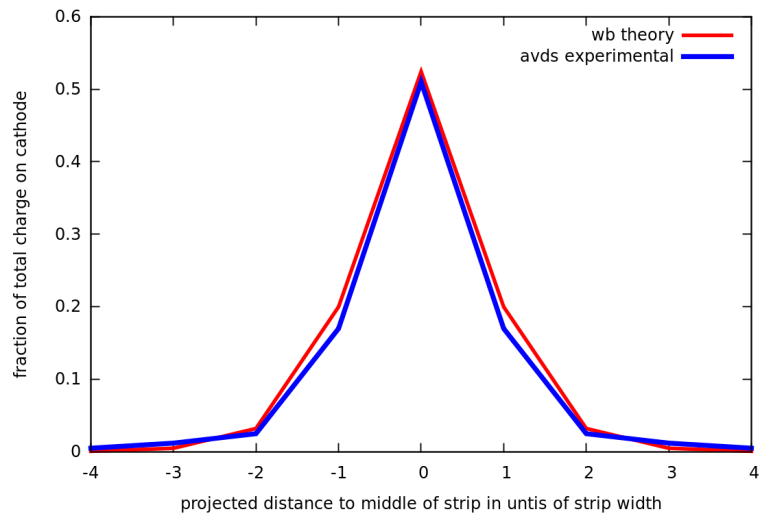
Figure 5.2: Comparison of Theoretical Prediction to PEN measurement data. The red curve shows the theoretical prediction and the blue curve represents measurement data results. The agreement is excellent. The data points are only at integer values.
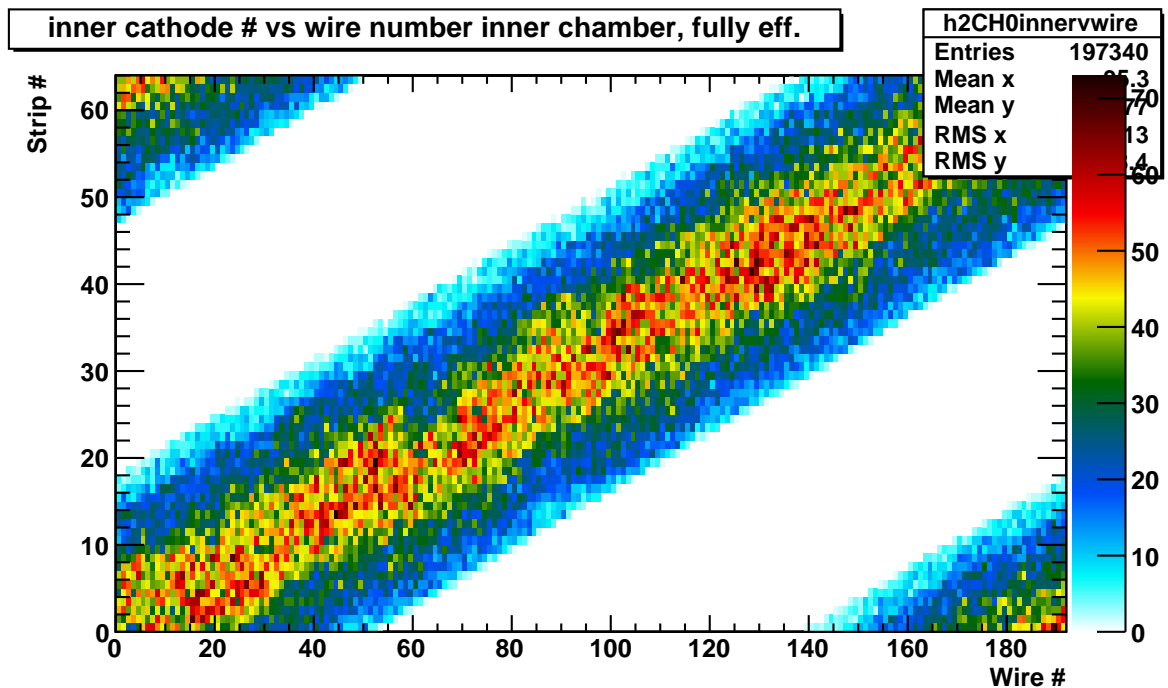
Figure 5.3: Measurement Data: This plot represents the correlation between the anode wires and the cathode strips. Given the geometry of the detector only certain combinations of the wire and strip will fire in coincidence.
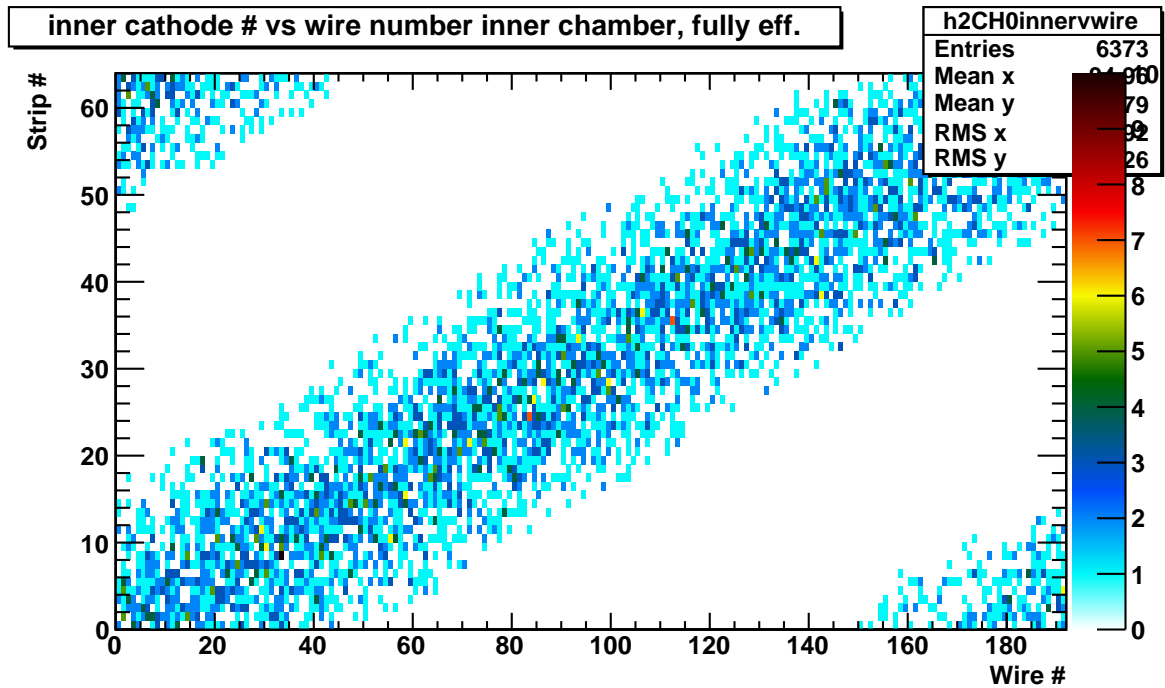
Figure 5.4: Simulation Data: This plot represents the correlation between the anode wires and the cathode strips. Given the geometry of the detector only certain combinations of the wire and strip will fire in coincidence.
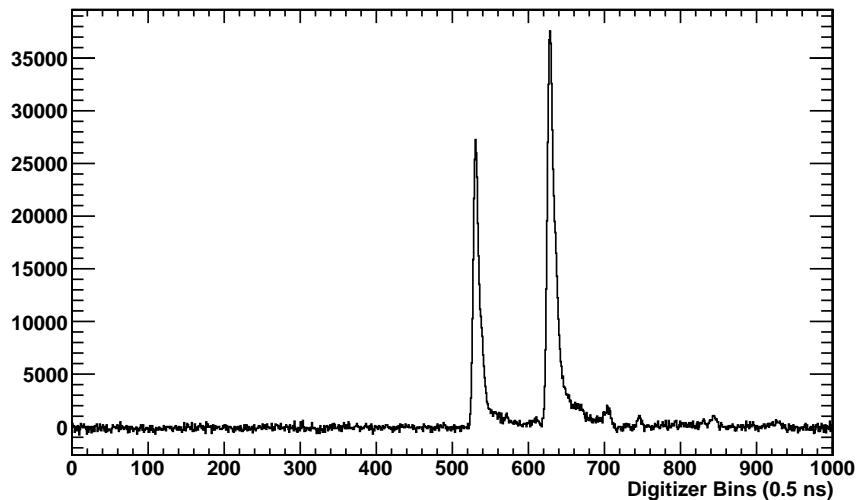
Figure 5.5: Sample waveform from the degrader detector. A pion pulse is shown from two different degrader fingers. The time separation is artificial and implemented for experimental reasons. The vertical scale is arbitrary.
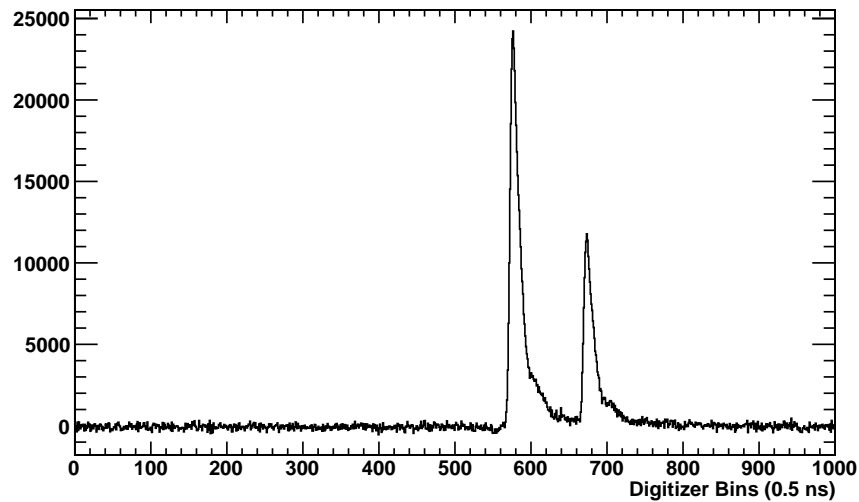
Figure 5.6: The same signal as shown in Figure 5.5 except produced form simulated data. That is to say the waveform from two of the degrader wedged. The vertical scale is arbitrary.
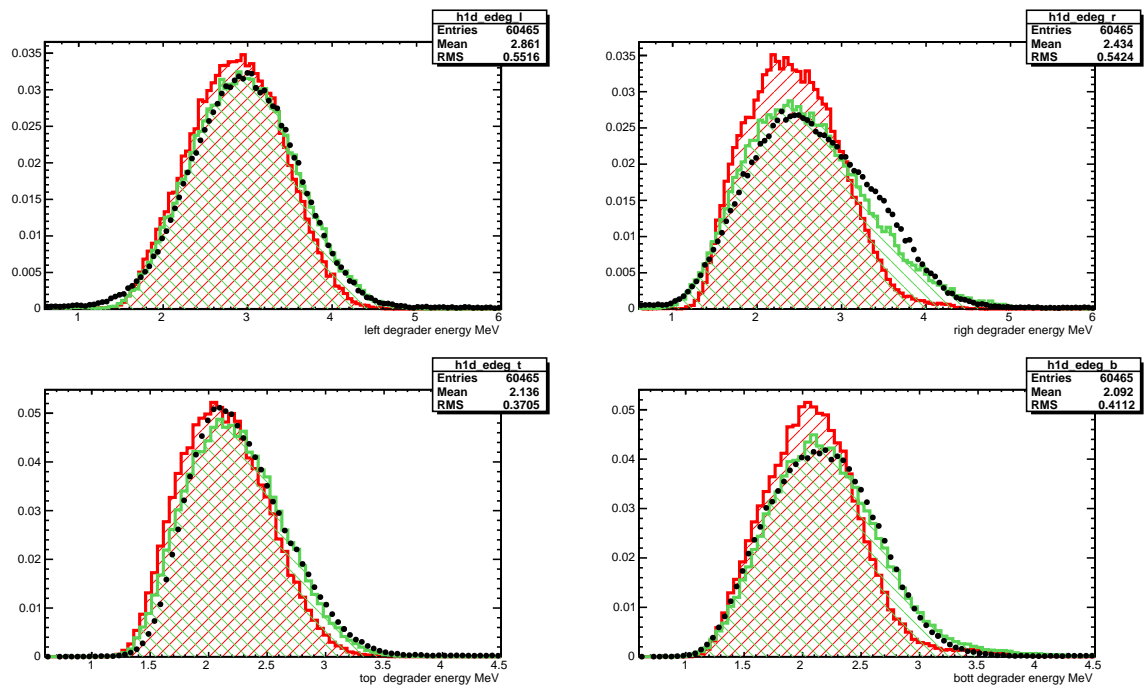
Figure 5.7: Each panel represents the energy deposition spectrum for a different degrader wedge. The signal is produced by beam pions. The vertical axis scale is arbitrary.
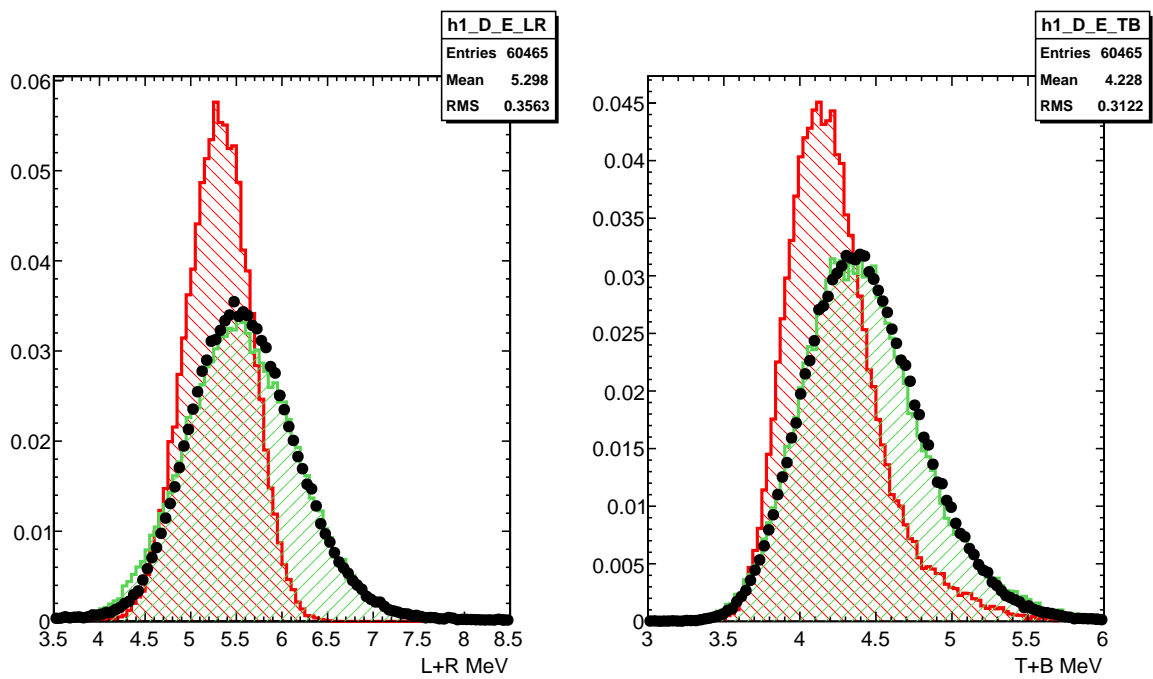
Figure 5.8: These panels represent the sum of the two horizonatal wedges (LR) and the sum of the two vertical wedges (TB). The vertical scale is arbitrary.
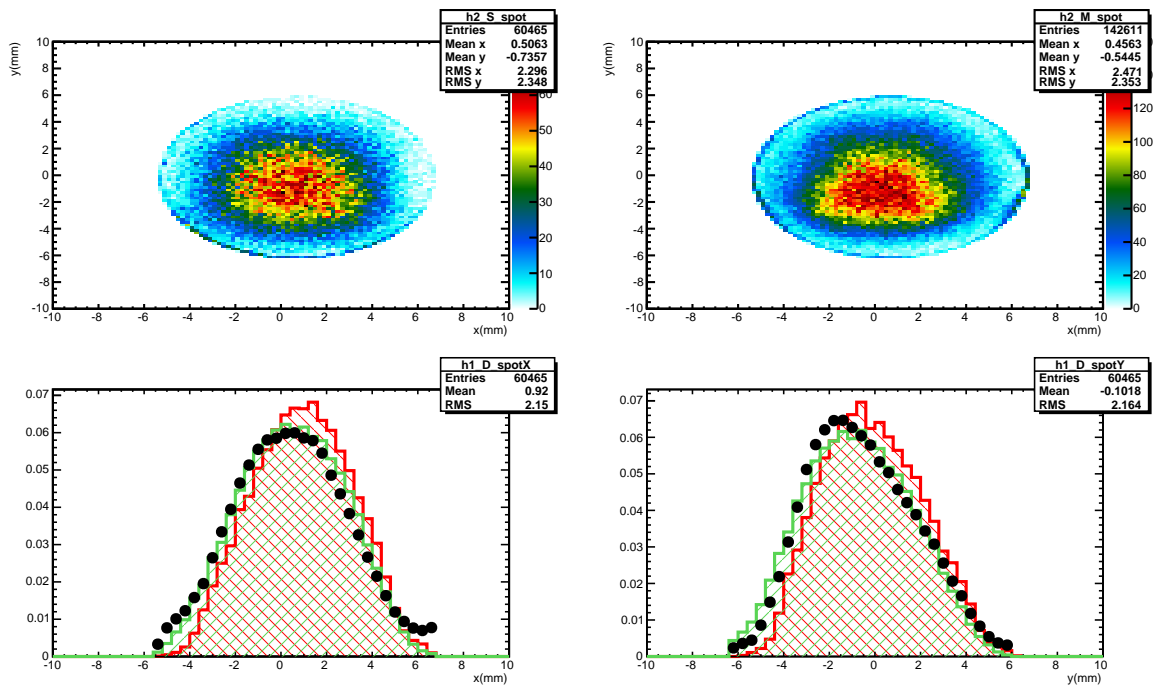
Figure 5.9: Panel 1: Simulation data – reconstructed xy position of the beam pion. Panel 2: Measurement data – reconstructed xy position of the beam pion. Panel 3: Horizontal profile of the beam pions. Panel 4: Vertical profile of the beam pions. For the bottom two panels the vertical scale is arbitrary.
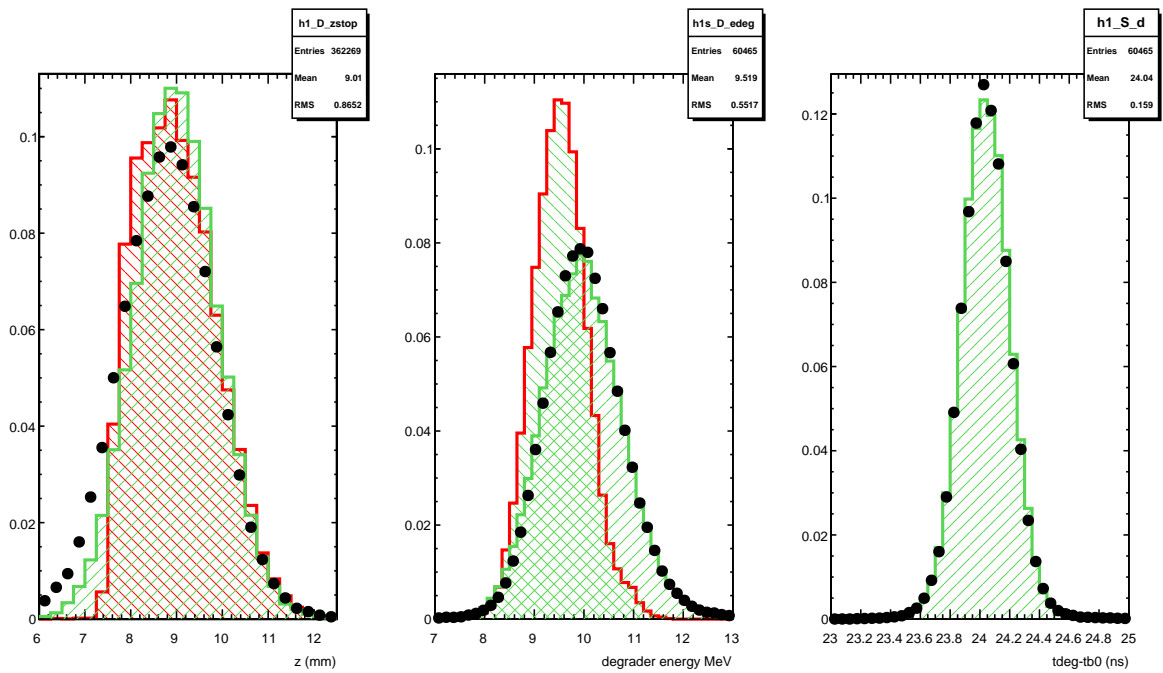
Figure 5.10: Pion stopping position constituent observables. Panel 1: Stopping position in the z direction. Panel 2: Degrader Energy. Panel 3: Pion time of flight from the upstream counter (B0) to the degrader. Again the vertical scale is arbitrary.
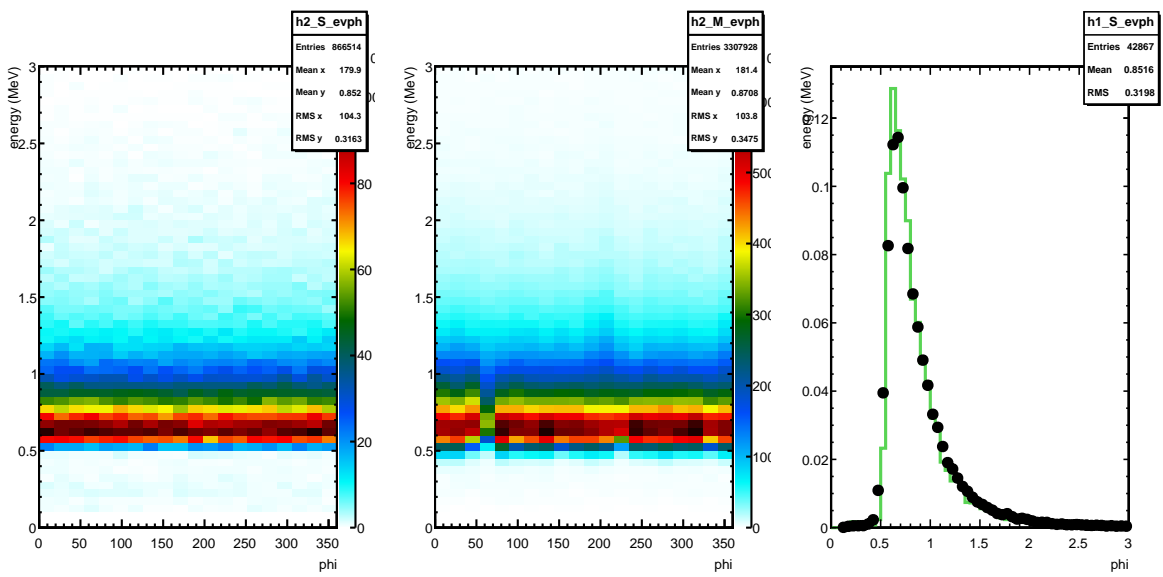
Figure 5.11: Summary of plastic hodoscope energy calibrations. The left panel is the simulation data, the middle is the measurement data. For these two histograms the horizontal axis shows the azimuthal coordinate but the binning is such that each bin represents only one module. The right-hand panel is the bulk response of all of the modules taken together.
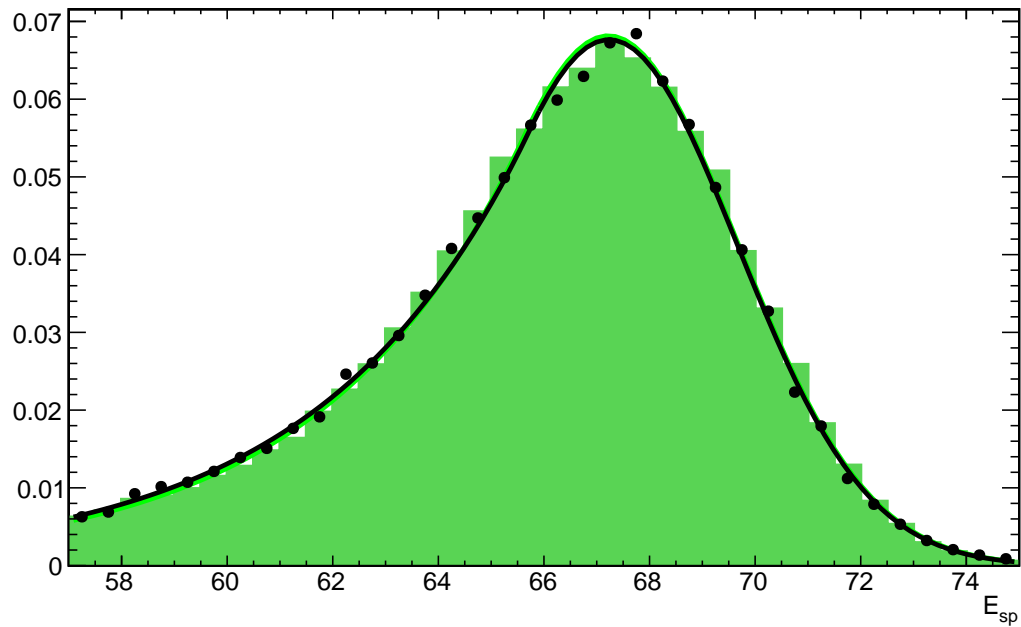
Figure 5.12: This plot represents E_{sp} for π_{2e} events. Measurement data is represented in black and simulation data in green. Various cuts are used to produce the event selection and the details are given in a technical note on the PEN web page.
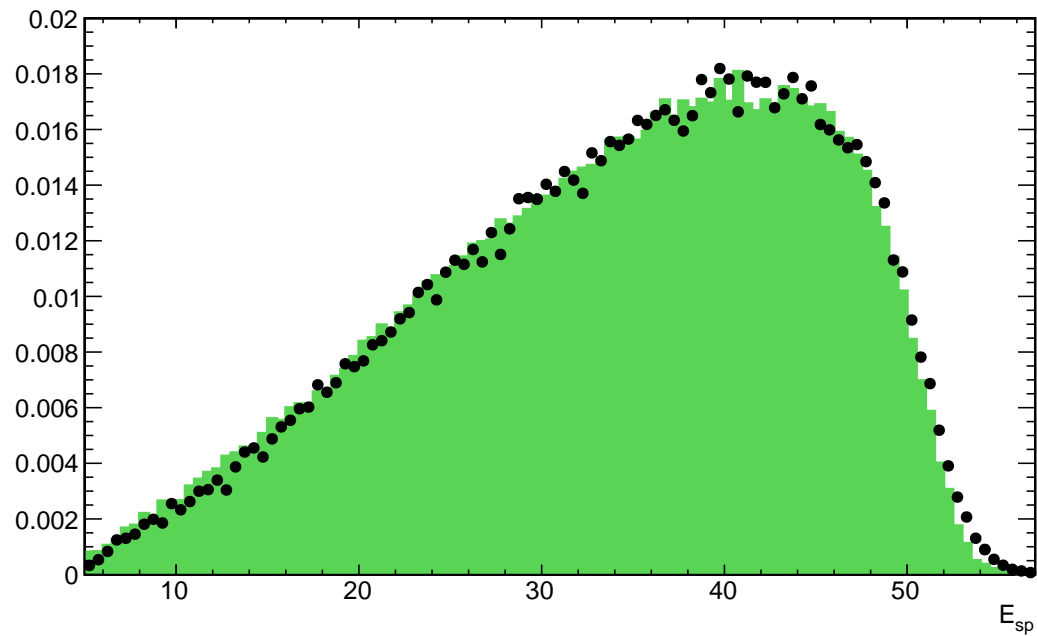
Figure 5.13: This plot represents E_{sp} for $\pi_{2\mu}$ events. Measurement data is represented in black and simulation data in green. Various cuts are used to produce the event selection and the details are given in a technical note on the PEN web page.

Figure 5.14: A photograph of the PEN electronics hut. The trigger system is located on the rightmost section. Below that behind plastic shielding are the raw CsI signal cables. The middle section of the racks contain the bulk discriminators and the bottom of the leftmost rack contains the FASTBUS modules. The left-hand section contains the slow control systems.

Chapter 6

Branching Ratio Analysis: $\pi^+ \to e^+ \nu \gamma$

Finally we have arrived at the most exciting part of this work, extraction of the $\pi \to e\nu_e\gamma$ branching ratio. All of the pieces are in place and we will now demonstrate the high level analysis step by step. As discussed in Chapter 1) and illustrated in (1.11) which is shown again for reference is the method for calculating the branching ratio:

$$B_{\pi \to e\nu_e\gamma} = B_{\pi \to e\nu_e} \left(\frac{N_{\pi \to e\nu_e\gamma}}{A_{\pi \to e\nu_e\gamma}} \right) \left(\frac{A_{\pi \to e\nu_e}}{N_{\pi \to e\nu_e}} \right). \tag{6.1}$$

Here B represents the branching ratio with the subscript denoting the process, N represents the number of observed events, and A is the acceptance. There are two components to this calculation. The first part is the main goal of the PEN experiment, namely $B_{\pi \to e\nu_e}$, which is the normalization channel for this measurement. From that branching ratio we normalize out the non-radiative decay. The second part is to factor in the radiative component yielding the radiative branching ratio. As a result this work needs to calculate the number of observed radiative pion decay events (RPD) and the associated acceptances.

To begin with, we will discuss the essential kinematic cuts brought about by nature of the decay. From there other experimental cuts will be discussed. The purpose of these cuts is to remove spurious events from the data set while not removing any signal events. As the clean signal begins to emerge the figures of merit along with signal and background definitions will be given. Finally the more delicate backgrounds will be handled to produce a clean signal. At that point the procedure of calculating the detector acceptance will be addressed. Due to the nature of the differential decay rate (xy dependence) the acceptance calculation is non-trivial. These results will be used along with (6.1) to produce the final result through a χ^2 minimization technique.

This analysis is purely cut based, therefore it is important to keep in mind the effect each cut will have on the experimental statistical yield, background elimination, and systematic uncertainty budget. Furthermore we are restricting our signal to events where both a positron and a photon are observed. As a result there will be RPD events that are indistinguishable from non-RPD events that we will reject from this analysis (for instance the radiative photon misses the geometrical acceptance of our calorimeter). It is also important to note that the decay rate weight factor is dependent on the parameters to be measured[1]. Therefore whenever results are presented we will show the results for a range of F_V and F_A (recall definition from Chapter 2. Historical evaluation of the form factors relied on fixing F_V via Conserved Vector Current hypothesis (CVC); the results will be presented in using this process [41]. Recent work by the PIBETA collaboration also presented the data for simultaneous fits of the form factors, as such we will present the results in that formalism as well.

---

[1] see (2.7) and (2.11)

6.1 Baseline Cuts

The choice of observable is of critical importance to any experimental study. For radiative pion decay the observation made is a coincidence between two particles. They both originate at the same point in space and time. Due to our detector's superior temporal resolution the natural choice of observable is the time difference between the decay positron (t_{e}) and decay photon (t_γ):

$$\Delta t \equiv t_{\mathrm{e}} - t_\gamma. \tag{6.2}$$

To begin we plot this observable from the raw data to see where our search begins (Figure 6.1).
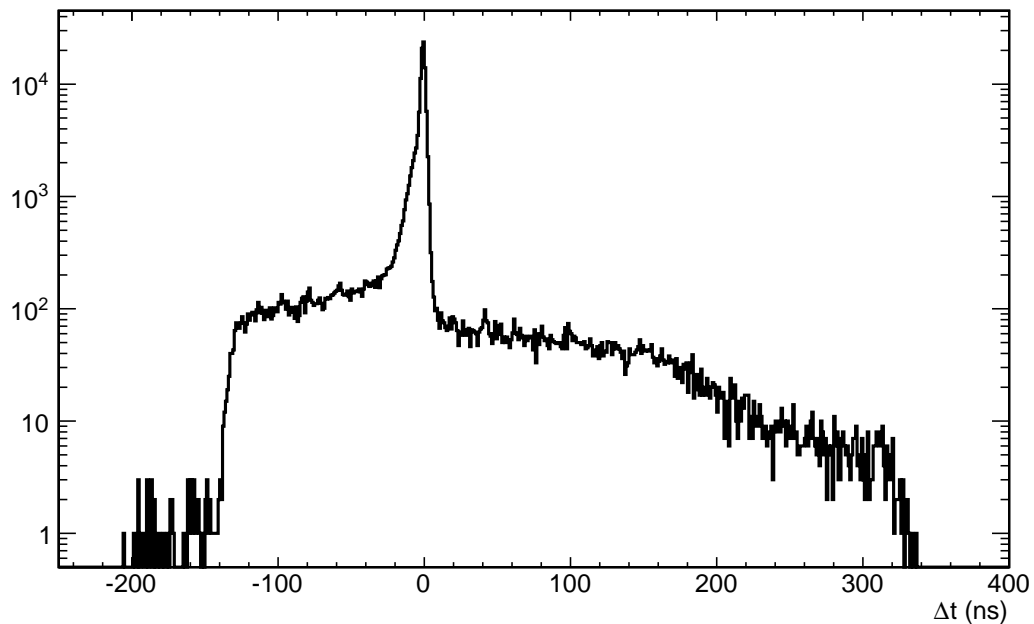
Figure 6.1: Main RPD observable: minimal cuts. The vertical scale is arbitrary.

Of course there are two classes of implicit cuts not mentioned that have already been applied to the data. The first class reside in the PEN group analysis code. The

general nature of these cuts is to remove seriously problematic events. For example this would include events where the data is fragmented, missynchronized between the different systems, or simply clearly containing errors that do not make physical sense. The second implicit cut is that only events with two tracks containing valid information are plotted . Furthermore due to nature of the trigger scheme in 2008 we will only examine the HI trigger. For the moment we will take a diversion to discuss the nature of these "tracks".

6.1.1   Tracks: Charged and Neutral Particles

Tracks are logical entities representing possible physical explanations of the signals measured by the PEN Detector. Each event may contain more than one track. Tracks are associated with a particular mass eigenstate or particle. For this study we are conerned with tracks that are reconstructed as positrons and photons. For the photon the only part of our detector that observes them with good efficiency is the calorimeter. If we see a signal from the calorimeter that is not assosciated with any signal from the tracking detectors then we label it as a photon. Of course this includes not only photons coming from our signal process but all sorts of background such as cosmic rays. The detector is cosmic ray shielded reducing the back ground. We can reduce this background further by acknowleding that signals from real photons originating in the target deposit energy in the calorimeter across a few neighboring crystals. These groups of crystals are called clumps. So to put it another way photon "tracks" are all of the excess "clumps" of energy measured by our calorimeter. There are additional constraints placed on the clumps such as exclusivity and temporal coincidence to further reduce background. The charged tracks are a little more complicated and involve a temporal coincidence between the calorimeter clumps and the charged particle tracking detectors.

Concerning the matter of particle identification for charged particles: given the

energy ranges acessible to PEN the only distinction that must be made is between positrons, pions, and protons[2]. The main method is to look at the energy deposited in the plastic hodoscope detector. Due to the minimum ionizing nature of these positrons and the decidedly non-minimum ionizing nature of the protons we simply apply a cut on energy deposition per unit length in the hodoscope (see Figure **??**. From this figure there is a clear separation in the signal from positrons and the signal from protons. The positrons show two peaks, one at the michel edge and the other at the π_{2e} peak position. They correspond to a low dE/dx. Where as the protons show an energy band up to the pion mass and have a dE/dx around six times larger. In fact there is evidence of an additional response above the proton energy that corresponds to a more massive hadronic state, likely an α-particle.
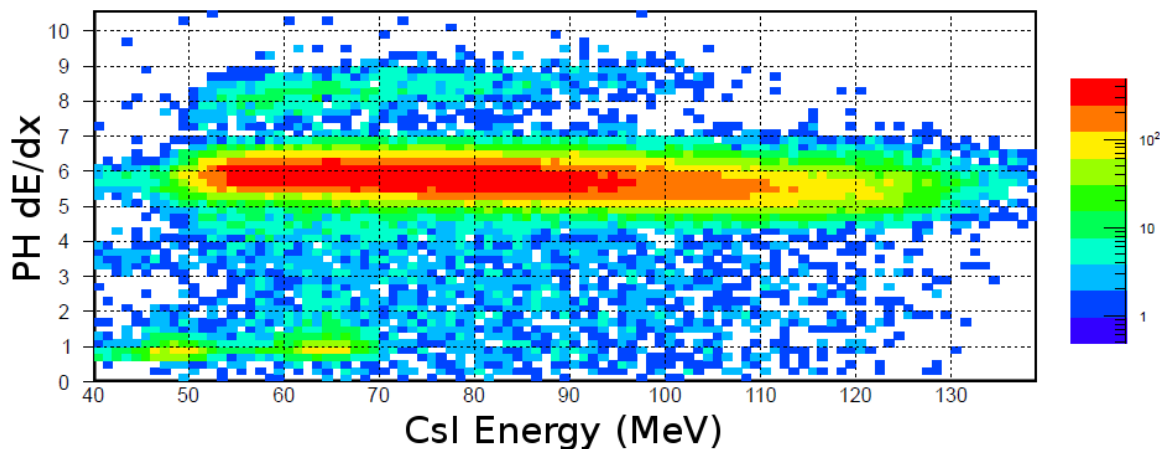
Figure 6.2: This plot shows the energy deposition per unit length for particles crossing the plastic hodoscope (vertical axis). The energy deposited in the CsI calorimter is plotted on the horizontal axis. Different particles show up in different regions of this plot. The lower left corner (low dE/dx) shows positrons. The middle band (dE/dx $\sim$ 6) shows the protons. We place a cut inbetween these two features to distinquis protons from positrons in the particle identification scheme.

Figure 6.3 demonstrates the situation after we include the particle identification routines in the PEN tracking system.

---

[2]Indeed there is no way for us to determine the sign of the charged particle.
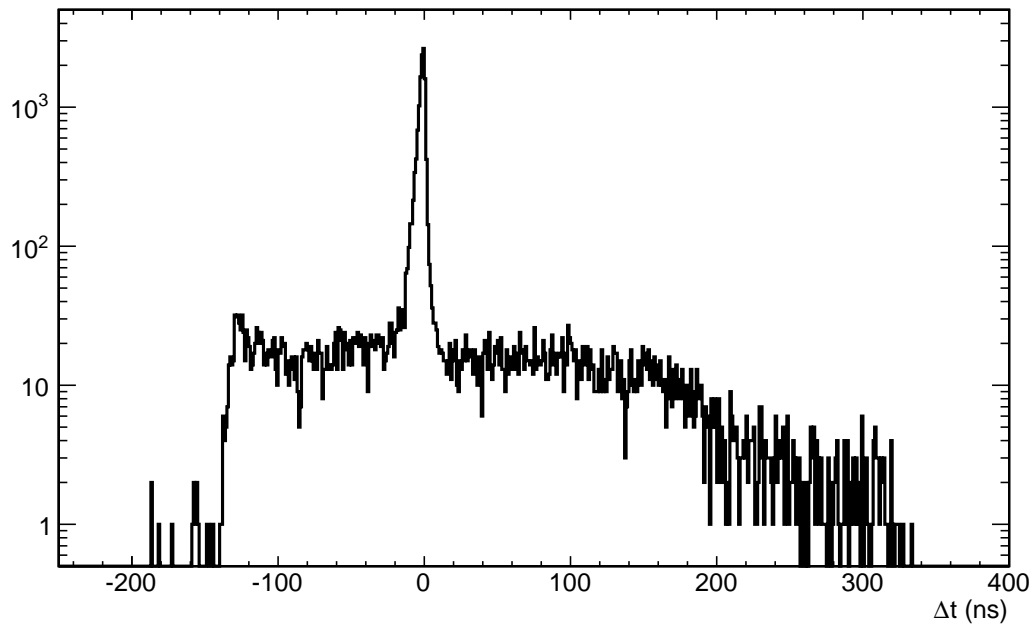
Figure 6.3: Main RPD observable: particle ID cuts. Vertical scale is arbitrary.

Track Reconstruction Efficiency

The efficiency of the track reconstruction process is a very important systematic to control. This process includes the deposition of signals in the tracking detectors all the way to final data analysis of those signals. For PEN we chose to simulate very carefully each step. Great care was taken to make sure that we have the correct simulation response for all of the detectors and that inefficiencies in those detectors are reflected in the result. The details of the simulation responses are given in the relvant sections of Chapter 5.

6.1.2 Broad Kinematic Region Cuts

The next step is to remove events from the data sample where the two tracks lay outside of the kinematic region described in Chapter 2. The least stringent of those cuts requires two conditions to be met. First it requires that the energy of the photon be greater

than 10 MeV. The photons below that energy threshold are predominantly from the inner bremsstrahlung contribution and do not contain information about the pion form factors. Secondly it requires that the opening angle of the two tracks ($\theta_{e\gamma}$) is greater than 40 degrees. Understanding the nature of the second cut is based upon the segmentation of the PEN calorimeter. The solid angle the typical crystal module spans 15 degrees. Showers from typical events are captured completely within a crystal and its nearest neighbors. Therefore the closest that two tracks can be resolved is 30 degrees. However we do not simply place the cut at 30 degrees because there is also the phenomena known as a *split clump.* When our software reconstructs the energy clumps in the calorimeter it is possible for two neighboring clumps to actually come from a single particle. For example a photon may leak outside of the nearest neighbor clump summation. The details of this process were worked out in the theses of M. Bychkov and B. van Devender ([31],[32]). As it turns out the frequency of split clumps becomes negligible (given the PEN error budget) at just below 40 degrees [42]. Therefore we round the cut up to 40 degrees for safety and elegance.

Figure 6.4 shows the status after the cuts enumerated so far. The structure in the observable has been reduced to two features, a flat region and a peaked region. The next step involves the behavior of the TDCs.

6.1.3   Kinematic Overdetermination Cut

As mentioned earlier (see Section 2.3) the measurement of the system is determined by making two measurements, the energies of the two particles. However it is also determined by measuring the energy of either particle and the opening angle between them. We use a kinematic observable λ and present two alternate ways of measuring
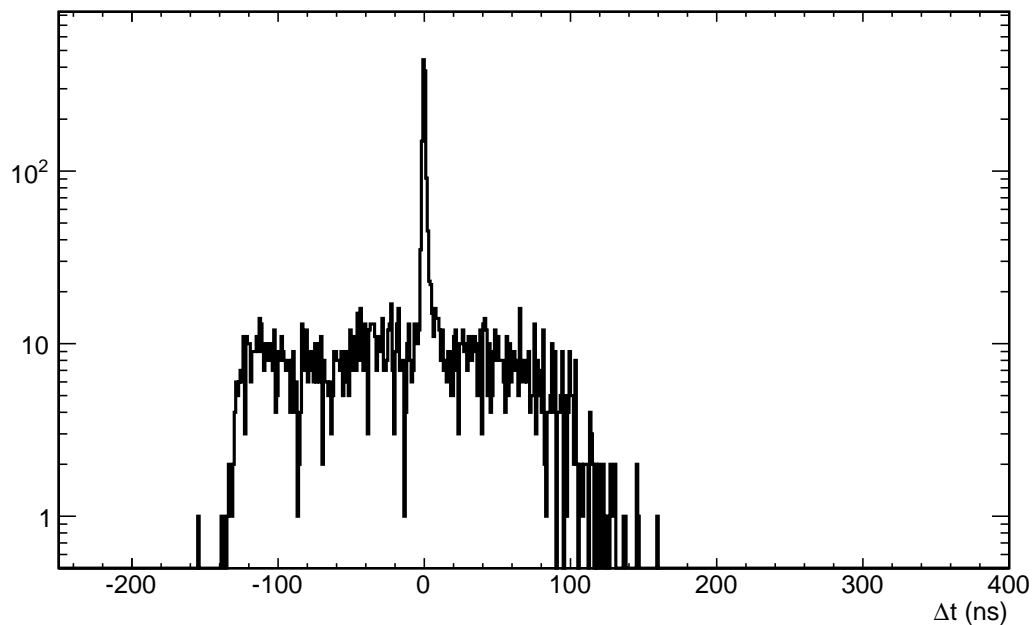
Figure 6.4: Main RPD observable: particle ID cuts and removal of low energy photons. Vertical scale is arbitrary.

it[3]:

$$\lambda_1 = y \cdot \sin^2 \frac{\theta_{e\gamma}}{2}, \tag{6.3}$$

$$\lambda_2 = \frac{x + y - 1}{x}, \tag{6.4}$$

$$\Delta\lambda \equiv \lambda_2 - \lambda_1. \tag{6.5}$$

We can then cut on the variable $\Delta\lambda$ to eliminate events that do not satisfy the kinematics of our decay. Figure 6.5 shows $\Delta\lambda$ versus Δt. From that picture we can see that the signal peak is contained in a narrow band of $\Delta\lambda$. We can make a broad cut to remove some background and revisit the fine tuning of this cut for optimization once we have established our figure of merit (which in this case will be the overal error estimate

---

[3]This convention differs from the literature. The traditional lambda contains only the angle measurement in λ_1 and only energy measurements in λ_2.

of the measurement).
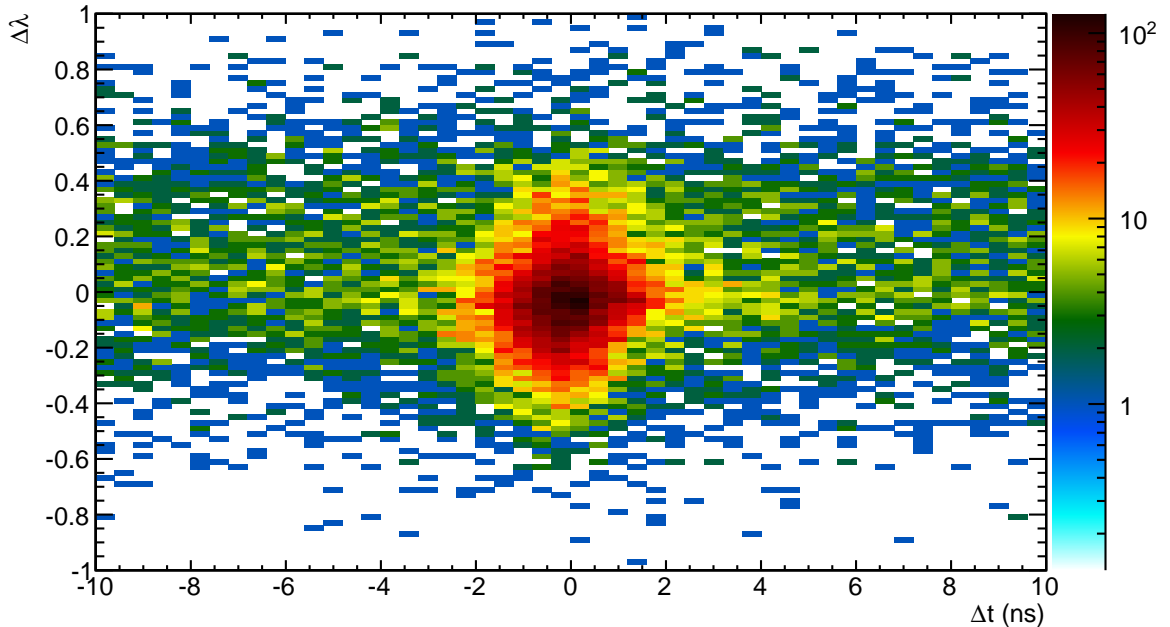
Figure 6.5: The plot shows the relationship between the kinematic overdetermination observable ($\Delta\lambda$ – vertical axis) and our signal observable (Δt – horizontal axis).

6.2 Signal Extraction $N_{\pi \to e \nu_e \gamma}$

6.2.1 PEN TDC Resolution

The next step is to use the coinicidence principle. We know that the photon and positron from the radiative pion decay are emitted at the same time. Both particles travel at the speed of light and deposit their energy in the calorimeter. Therefore we can reject events where the timing between the two particles is large. But how do we determine that region? Based on the data shown in Figure 6.4 we clearly recognize the signal peak around $\Delta t = 0$. Therefore we must inspect the resolution of that peak with the full detector and analysis effects included.
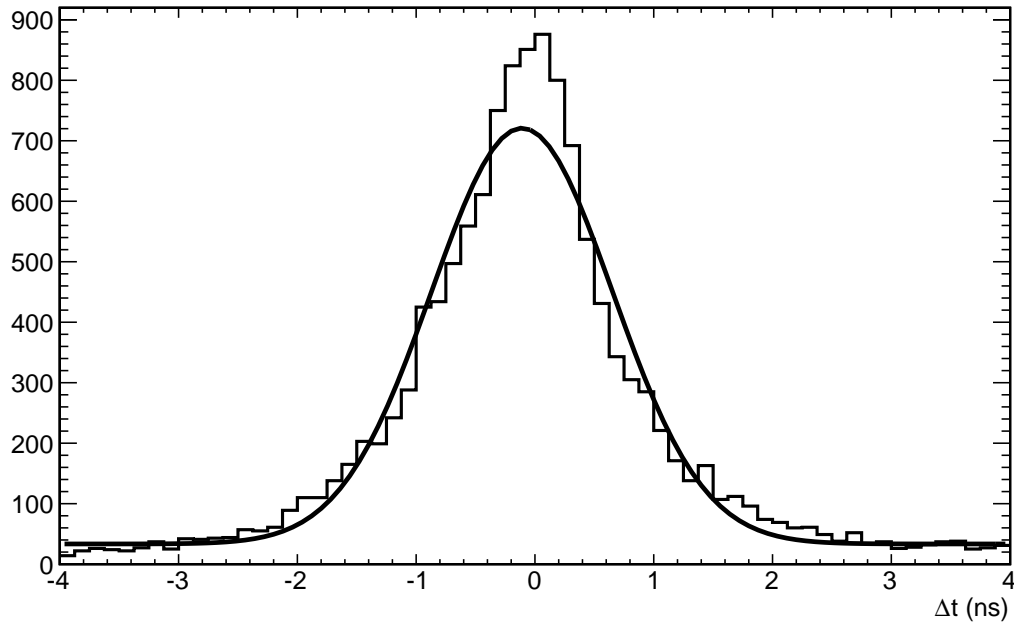
Figure 6.6: Main RPD observable: all baseline cuts included. Vertical scale is arbitrary.

Figure 6.6 shows the central region fitted with a two-component function (Gaussian plus a constant). The standard deviation of the peak shown is 1 ns. To determine the width of our signal region we compare this deviation with the acceptable error in our experiment. Extending the signal region to be five times as wide as the standard deviation implies a loss from the signal region cut of 1 event in every 1.7 million events. This acceptance is well below our uncertainty level for this experiment. Now that we have decided on a signal region of $(-5,5)$ for Δt we can define a background region. The elegent solution is to make the background region as wide as the signal region. Thereby accounting for an equal amount of observable space and large enough to reliably sample the background region. We proclaim the background region to be $(-10,-5)$ and $(5,10)$. Applying these definitions we arrive at a preliminary picture shown in Figure 6.7.
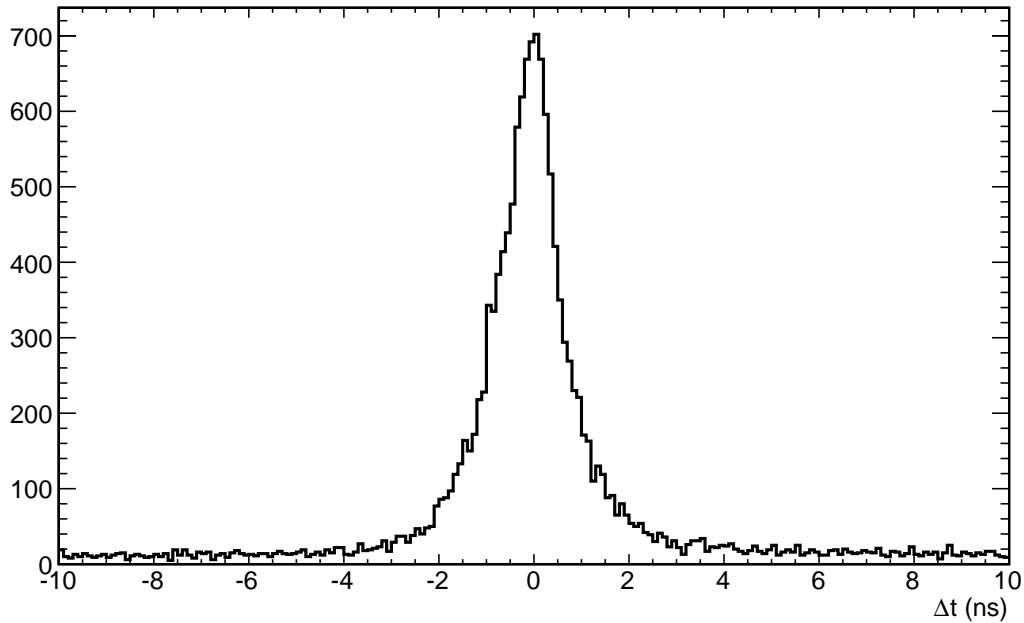
Figure 6.7: Main RPD observable: baseline cuts. The domain has been set to the signal and background region. Vertical scale is arbitrary.

6.2.2 Cross-check

Now that we have removed a large amount of background data it is time cross-check with another observable. Another equally viable observable to use for this analysis would be the apparent *decay time* of the event. Our system triggers on the coincidence of two occurances: the first is a stopped pion in the beamline, and the second is a large enough energy deposition in the calorimeter. The timing difference between these two events is the decay time. For a sample of purely radiative pion decays we would expect to see a decaying exponential with the characteristic time of the pion life time (approximately 26 ns). Figure 6.8 shows the decay time spectrum for the cuts detailed above.

From this figure we can see a clear deviation from the pion life time. There is substantial contamination from $\pi \to \mu \to e$ like events. They are characterized by a composite decay time consisting of the muon life time and the pion life time but with opposite sign.
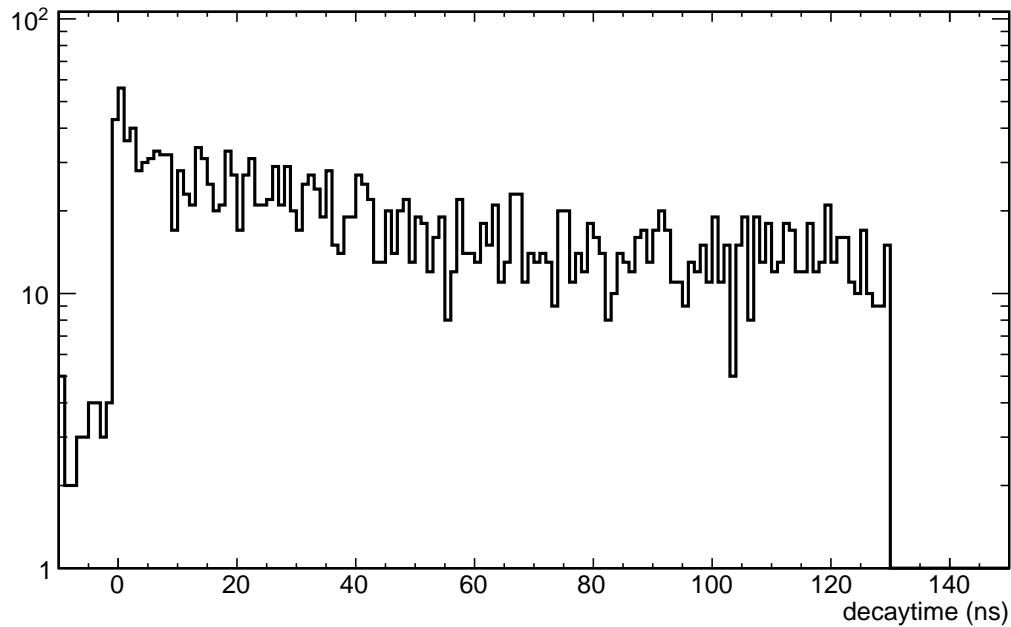
Figure 6.8: Decay Time for baseline cuts in the signal and background regions. Vertical scale is arbitrary.

Physically the pions must decay to populate the system with muon states before the muon can decay. We have two weapons at our disposal to remove this contamination. The first is the traditional timing fit with multiple components. The second is implement direct cuts to eliminate these events. While fitting this shape with characteristic time signatures of π_{2e} and $\pi_{2\mu}$ procesees will work, it leaves the experimentalist unsatisfied. The number of events observed now depends on this fitting ability. Continuing with additional direct observable cuts is preferable. Previous experimental attempts used the time fitting technique but advances have been made in the detector technology [43], in particular the addition of the Acqiris Waveform Digitizer. Using the information collected by that detector will enable us to remove the $\pi_{2\mu}$ background.

6.2.3   Target Waveform Analysis Cut

Examination of the target waveform enables a safe removal of events where the particles are well separated and a muon is present. The work to develop these routines was done by A. Palladino and many details on their development can be found in his thesis [40]. For the purposes of this study it is important for the reader to know the following:

1. For each event target pion and target positron time predictions are made.

2. For each event target pion and target positron energy predictions are made.

3. These predictions are used to estimate the pion and positron signal in the waveform.

4. Those estimates are then subtracted from the waveform.

5. **If a muon was present in the target waveform its signal sticks out like a sore thumb.**

The target waveforms are then tested using a χ^2 method and the resulting observables are presented for analysis. Figure 6.9 shows the event decay time versus the difference in the χ^2 variable for the 2-peak and 3-peak hypotheses (parameterized so that π_{2e}-like events are positive in $\Delta\chi^2$). There are two groups of events present in the plot. There is a band exhibiting the characteristic $\pi \to \mu \to e$ time signature centered around $\Delta\chi^2 = -21$ and a group that exhibits a $\pi \to e$ time signature centered around $\Delta\chi^2 = 13$. The purpose of this cut is to remove the former from the data set so we make a cut at $\Delta\chi^2 = -12$, removing nearly all of the problem events without impacting the good events at all[4].

---

[4]The optimization of this cut was done with the overal experimental uncertainty in mind. We tried a range of values and settled on the best one as determined by the figure of merit.
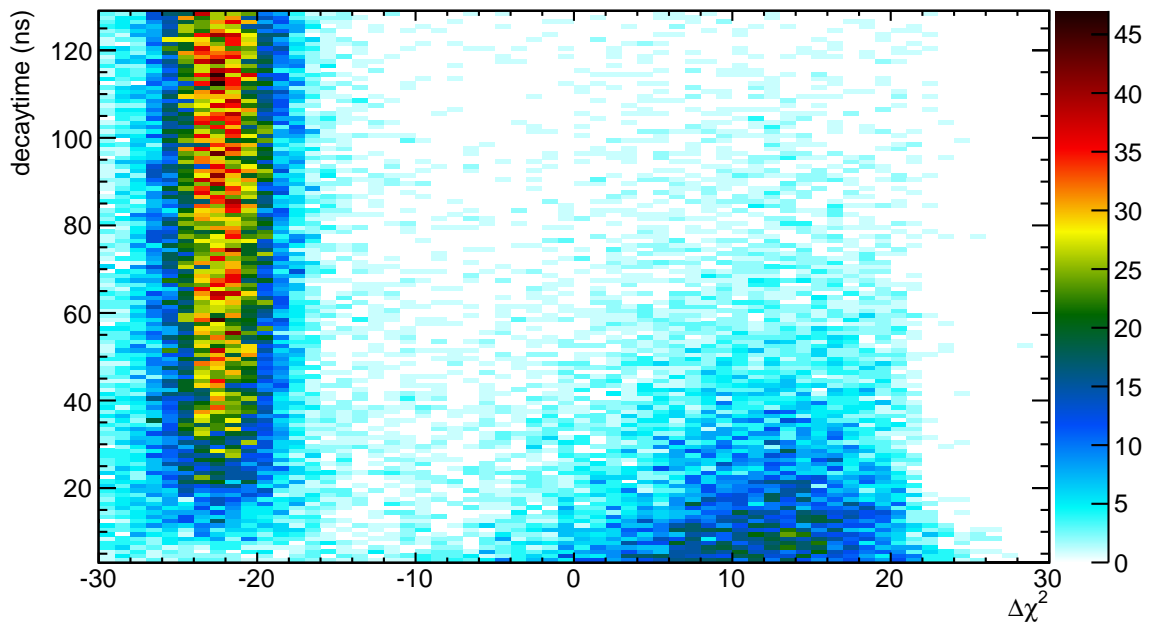
Figure 6.9: Decay Time vs. $\Delta\chi^2$. The events with the characteristic $\pi \to \mu \to e$ time signature are well separated from our signal events.

Now we can revisit the decay time spectrum. Figure 6.10 shows the decay time observable for all events with the waveform cut imposed. We chose to plot the distribution on a linear scale because a new feature is now present in the data. There is a structure with a period of 20 ns. Every step in the process seems to point to a new contamination, but rest assured each new wrinkle produces a smaller systematic error in the experimental system. Eventually the systematics will be reduced to a level below our sensitivity and we can proceed with the analysis.

6.2.4 Beamline Signal

There is one additional feature remaining in the decay time observable, it results from contamination. There is clear evidence of a repeating phenomena every 20 ns. As it turns out that structure comes from the accelerator frequency which is about 50.63 MHz. The
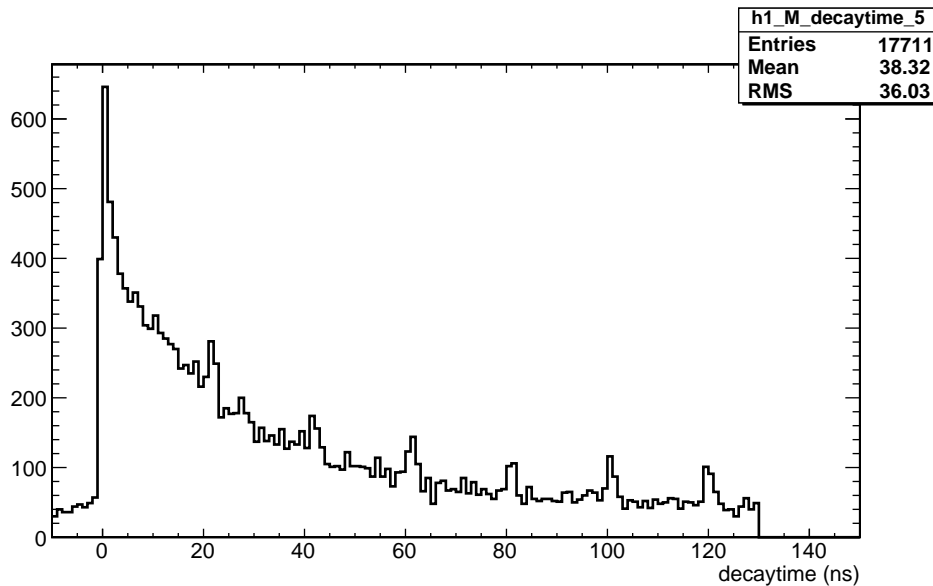
Figure 6.10: Decay Time for baseline cuts and waveform cuts in the signal and background region. Vertical scale is arbitrary.

majority of these events are scattered beam positrons. Through careful analysis of the beamline detectors (B0 and degrader) we have been able to identify events where there are extraneous or poorly behaved beam particles. Placing a cut on those events produces the following distribution shown in Figure 6.11. There are several features that can cause the rejection of an event. For instance the incorrect time of flight or the wrong amount of energy deposition. Details of this cut can be found on the PEN CMS [44].
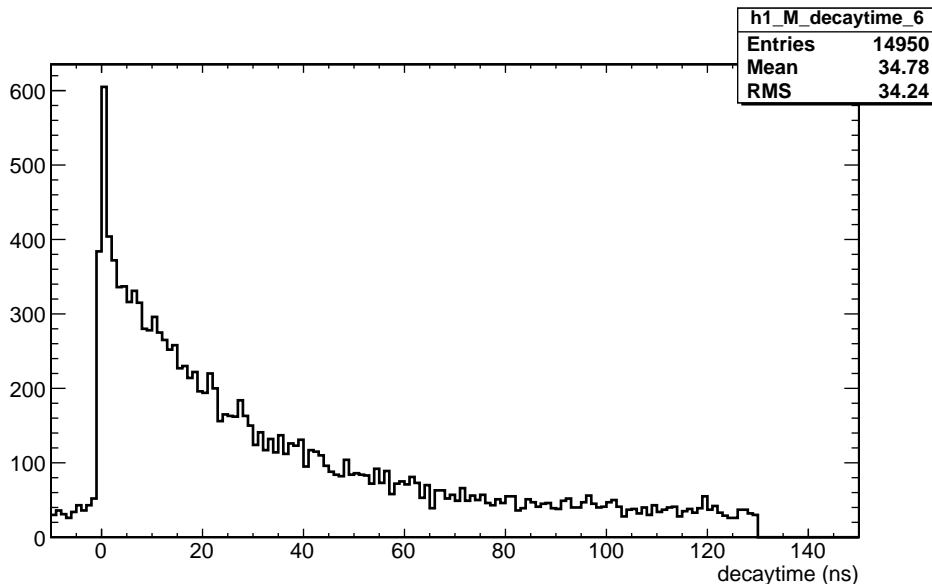
Figure 6.11: Decay Time for baseline cuts, waveform cuts, and **50 MHz supression** in the signal and background region. Vertical scale is arbitrary.

6.2.5 Summary so far

Now we present a summary of the cuts made on the data so far and show the two signal observables. Table 6.1 shows a summary of all of the cuts applied so far in the isolation of the RPD signal. Figures 6.12 and 6.13 show the track timing difference and the decay time observables.

6.2.6 Background Subtraction and Regional Yields

Now that we have eliminated as much contamination from our data set as possible it is time to measure the signal events in each kinematic region of interest. As a reminder Table 6.2 has been repeated. Recalling the results from earlier sections we recognize region A as the cleanest region from a standpoint of bremstrahlung contamination. Region B is the only region in this sample with sensitivity to the $F_V - F_A$ term. Region C is the least important for this study as it is mostly a poorer sample of $F_V + F_A$ than region A, however it does contain considerably more statistics. Unfortunately those

Table 6.1: RPD isolation cuts.

Cut Name	Description	Observable
Hi Trigger	A high energy particle	`trigger==1.`
Decay Time	select events t< $5\tau_\pi$	`decaytime_wvfm<130.`
Particle ID1	check for positron	`particle_1_id==3`
Particle ID2	check for photon	`particle_2_id==2`
Opening Angle	$\cos\theta_{e\gamma} < 40°$	`costheta_eg<0.766`
Timing Window	valid positron time	`fabs(t_y)<20.`
Timing Window	valid photon time	`fabs(t_x)<20.`
Valid Coincidence	$t_e + t_\gamma$ valid	`fabs(t_y-t_x)<10.`
Central Hit	avoid calorimeter edges	`CsI_outer_sum == 0.`
Photon Minimum	photon energy < $10\,\mathrm{MeV}$	`x>0.1433`
Valid Kinematics	$E_e + E_\gamma$ valid	`x+y>1.0001&&x+y<2.`
Valid Waveform Fit	Check for valid wffit	`delta_chi2!=0.`
Remove Michel like	Check wvfm $\Delta\chi^2$	`delta_chi2>-12.`
Use good 2peak fits	Check wvfm χ_2^2 is small	`chi2_2peak<25.`
Remove Beam Scatter	Cut on b0 dg wvfm signals	`beam_positron==0`
Kinematic Check	Check $\Delta\lambda$ is small	`fabs(lam1-lam2)<0.3`
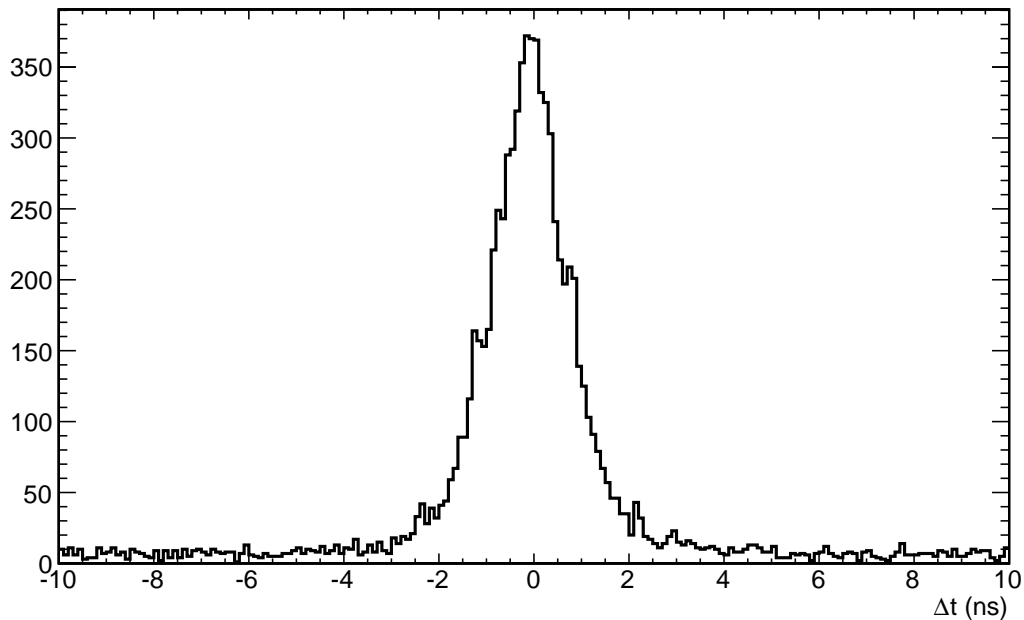
Figure 6.12: Main observable for all regions with all cuts imposed. Vertical scale is arbitrary.
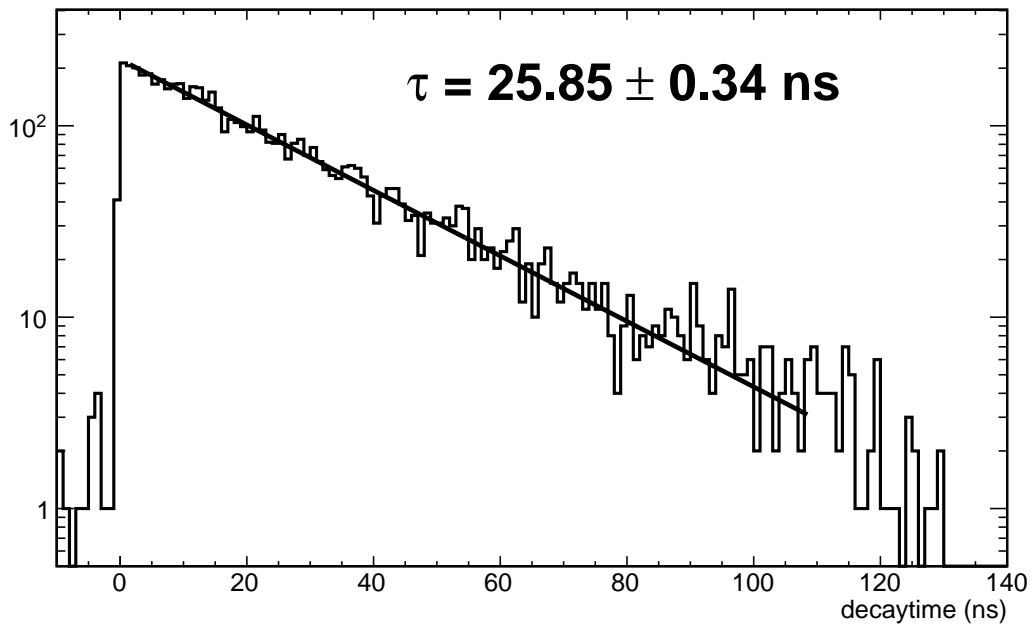
Figure 6.13: Secondary observable for all regions with all cuts imposed. The black line represents a one component exponential fit. The characteristic decay rate of the exponential is consistent with the pion life time. The error quoted is purely statistical. Vertical scale is arbitrary.

statistics are still not high enough for a reasonable measurement of the momentum dependence of F_V. Once the 2009 and 2010 PEN data is analyzed evaluation of a will be possible.

Table 6.2: Branching Ratio Evaluation Regions.

Measurement (MeV$_{exp}$)			BR Evaluation (MeV)		
Reg.	$E_{e^+}^{exp}$	E_γ^{exp}	Reg.	E_{e^+}	E_γ
I	> 51.7	> 51.7	A	> 50	> 50
II	$20 - 51.7$	55.6	B	> 10	> 50
III	> 55.6	$20 - 51.7$	C	> 50	> 10
			O	$> m_e$	> 10

Now that all of the cuts have been applied the Δt observable shows a Gaussian-like signal superimposed on a flat accidental background. This accidental background

presumably exists in the signal region as well. Therefore we sample the background region and subtract it from the signal region. Since the two regions were chosen to have the same size in Δt space no renormalization is necessary. This subtraction is done for each individual region of study. The resulting histogram is then integrated and the result reported in Table 6.3. Additionally the figure of merit of the quality of the data is the ratio of the signal peak to the background level. That ratio is determined by fitting the observable with a Gaussian plus a constant function. The results of that fit are then used to calculate the P/B ratio. Figures 6.14, 6.15, and 6.16 graphically represent the fits. These results are also summarized in Table 6.3.
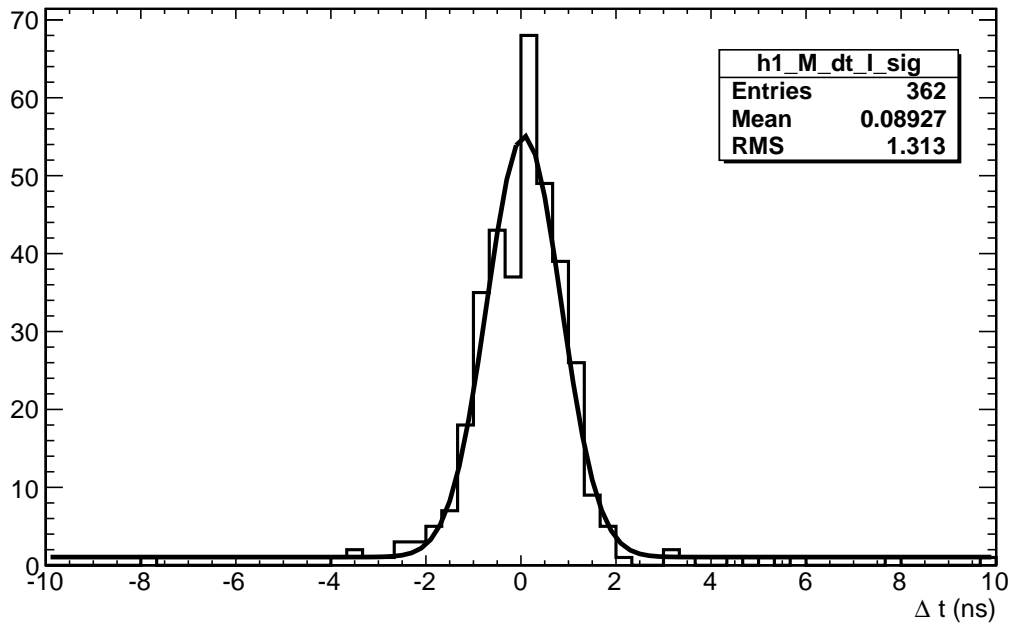
Figure 6.14: Region I event signal with the background subtracted. The superimposed line is a fit of Gaussian plus constant. Vertical scale is arbitrary.
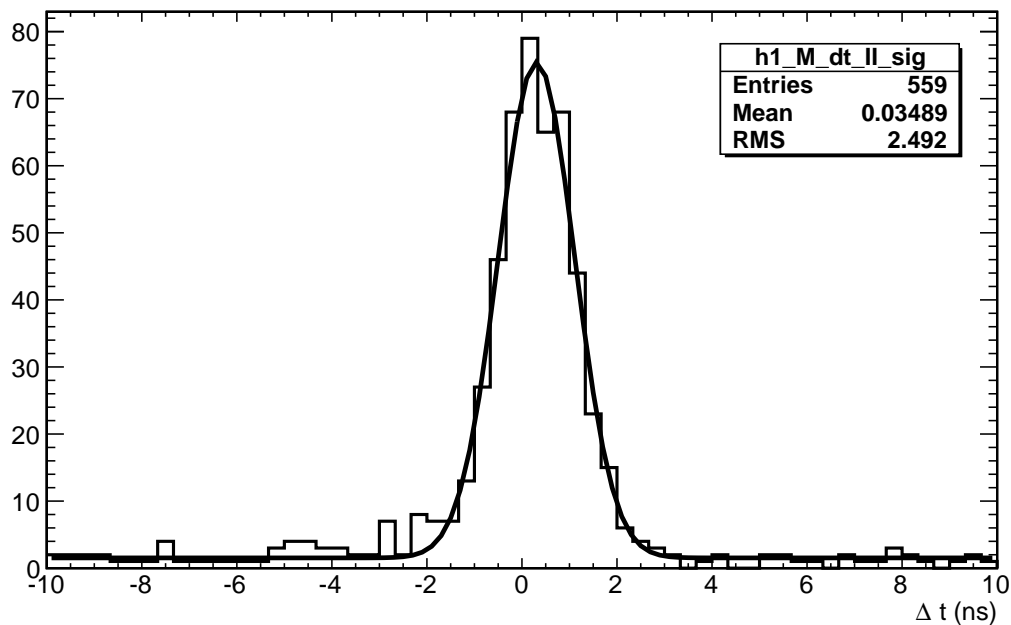
Figure 6.15: Region II event signal with the background subtracted. The superimposed line is a fit of Gaussian plus constant. Vertical scale is arbitrary.

Table 6.3: Events Observed By Region.

Region	Events		σ_E	P/B
I	192.9	$\pm$	14.0	>200
II	272.4	$\pm$	18.6	90.7
III	586.2	$\pm$	32.3	23.3
O	3884.1	$\pm$	71.2	64

6.2.7 Signal Contamination from π_β-decay

We have eliminated all signals not originating from a stopped pion decay. Now we must look to see if the pion has any decay modes which could potentially masquarade as our signal. Examination of the observed pion decay modes from the Particle Data Group yields one potential candidate. If the pion undergoes beta decay the subsequent decay of the neutral pion would produce two high energy photons. If one of those photons converts to a charged particle early enough it could produce a charged track and along
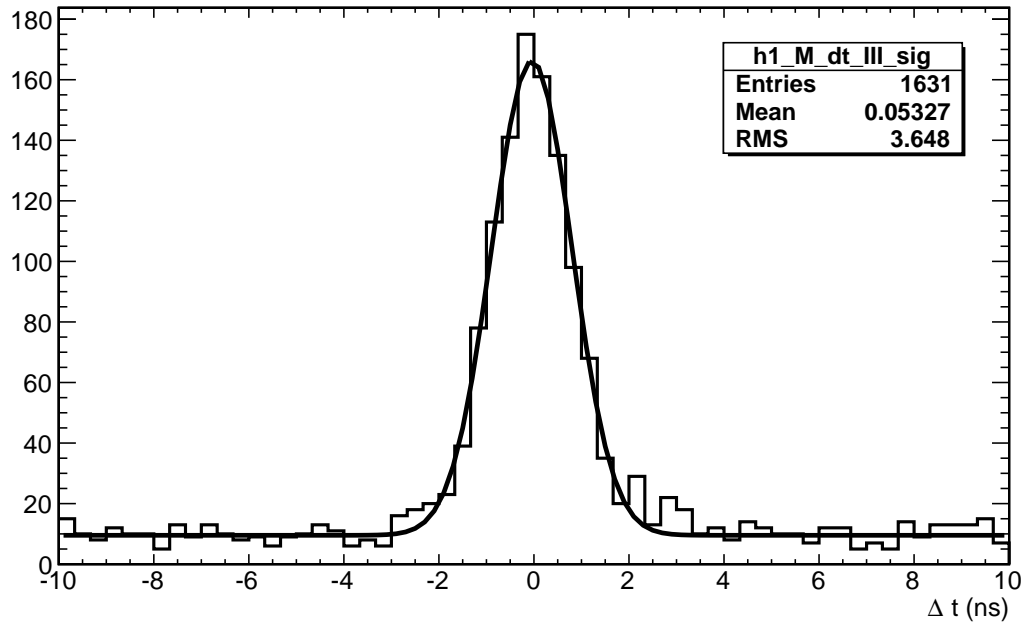
Figure 6.16: Region III event signal with the background subtracted. The superimposed line is a fit of Gaussian plus constant. Vertical scale is arbitrary.

with the other photon produce a signal of a high energy positron track and a high energy photon track. Additionally this event would pass the kinematic cuts ($\Delta\lambda$) because the neutral pion decay is back-to-back photons each with half the neutral pion mass.

Given the limitations of our experimental set up there is no way to eliminate this contamination with a cut on observed data. Therefore we must turn to simulation. Using the simulation we produced a sample of 10 million $\pi\beta$ events and then applied the RPD analysis code. That results when compared to the actual number of simulated decays gives a measure of the acceptance of $\pi\beta$ events as RPD events. From the measurement data we determined the number $\pi\beta$ events in our data sample and the applied the acceptance value from simulation to determine the number of events we reconstructed as RPD that were actually From the measurement data we determined the number $\pi\beta$ events.

The results are summarized in Table 6.4. The first column shows the kinematic region

of interest. The second column is the number of events extracted from the analysis as shown in Table 6.3. The next column shows the acceptance for pion beta-decays in each region. The last column shows the number of events after subtracting the $\pi\beta$ contamination.

Table 6.4: Results of $\pi\beta$ decay subtraction.

Region	Raw Reconstructed Events	$\pi\beta$ acceptance	Events After Subtraction
I	192.9	1.009(50)%	188.6
II	272.4	0.097(50)%	272.0
III	586.2	0.053(50)%	585.9
O	3884.1	1.207(50)%	3879.7

6.3 Acceptance calculation $A_{\pi \to e\nu_e\gamma}$

Now that the determination of $N_{\pi \to e\nu_e\gamma}$ is in place we turn our attention to the acceptance of the system $A_{\pi \to e\nu_e\gamma}$. At the most fundamental level the acceptance value ammounts to determining how many events would be observed for a given number actual events. In our case how many events we would reconstruct as radiative pion decays (in the appropriate kinematic region) for a given absolute number of radiative pion decays. The previously parenthetical statement actually adds quite a large amount of complexity to the problem as we will soon see.

The nature of acceptances is such that one must have a handle on the unobserved. However by that very admission we confess to not knowing everything. In this particular case we cannot know the actual number of radiative pion decays in our system because that is the very thing we are trying to measure. As a result we turn to simulation techniques to break the loop. We will use a simulation to produce a known quantity of radiative pion decays. Then we will apply our experimental signal cuts to the simulated data and extract the quantity of observed radiative pion decays. Of course there are a

few assumptions made in the technique. The first is that the simulation needs to be an accurate representation of the experimental system, and the second is that we have an accurate theoretical description of the process to begin with (in this case the differential decay rate). Both of these assumptions will introduce systematic errors into the analysis and through careful treatment are reduced to tolerable levels.

Understanding the underlying theory is critical to a sucessful simulation. In the particular case of many body decay we face the difficulty of the differential decay rate. In order to properly generate the simulation events we need to know the differential decay rate. But the parameters we are trying to measure also determine the differential decay rate. Therefore we must undertake our study in an iterative fashion. The acceptance of the system depends on the energies of the decay products and if the differential decay rate distribution changes then the acceptances will as well. Therefore we must calculate the acceptances for the system over a range of input parameters, F_V and F_A. The determination of the acceptances is inexorably linked to the evaluation of the branching ratio.

6.3.1   Differential Decay Rate

The differential decay rate for RPD is divergent at low photon energies. Additionally the region of interest has a much smaller value of the decay rate than the uninteresting bremstralung region. Therefore it is impractical to simulate the events with the proper phase space distribution. We simulate the events uniformly in the kinematic variables (x and y) and then apply a weight factor in accordance with the decay rate formula at analysis time. To determine the number of events thrown, we must simply add all the weights for the thrown events. When determining the number of events observed we must add the weights for the events that pass the experimental cuts.

There is an additional subtlety that enters in from the nature of the theoretical and

experimental region definitions. The experimental region needs to be small enough such that no events can come from outside of the theoretical region[5]. That means that we aknowledge the imperfection of our detector and realize that an event observed to have a certain amount of energy may in fact be an event with a larger or smaller amount of energy. To determine the branching ratio in a particular theoretical region (A) we sample events in a subregion (I). Then the acceptance value contains the expansion cooeficient from experimental to theoretical region. The better the detector system (in this case energy resolution) the closer in size the experimental region can be to the theoretical region.

In summary the the acceptance calculation is simply the number of simulation events observed in the experimental region divided by the number of simulation events thrown in the theoretical region. This calculation is done carefully and incorporates all of the nuances indicated previously. Additionally it should be noted that the simulation must be weighted based on the divine energy values and not the observed energy values.

6.4   Calculating $B_{\pi \to e \nu_e \gamma}$

In order to compare the values of the theoretical and experimental branching ratio we have elected to use a χ^2 technique defined by the following formula:

$$\chi^2 = \sum_{i=\text{A,B,C}} \frac{(B_i^{\text{the}} - B_i^{\text{exp}})^2}{\sigma_i^2}. \tag{6.6}$$

The summation is conducted over the theoretical regions of interest (A,B,C), the normalization for each term (σ) is taken to be the standard error of that evaluation. It is critical to remember that both the theoretical branching ratio (B^{the}) and the experimental branching ratio (B^{exp}) depend on the input parameters F_V, F_A, and a. Therefore

---

[5]At least a small enough number of events to be within the error budget.

at each iteration point the values must be recalculated.

6.4.1   Fixed F_V and a

Before the PIBETA experiment result there were no high precisions studies conducted on RPD. Several questions about the parameters of interest were uncertain. Direct measurements of the values were not possible so the CVC hypothosis was used to fix F_V in the following manner:

$$|F_V(0)| = \frac{1}{\alpha}\sqrt{\frac{2\Gamma_{\pi^0 \to \gamma\gamma}}{\pi m_{\pi^0}}} = 0.0259 \pm 0.0009. \tag{6.7}$$

Using that value as an input the value of F_A could be calculated by exploring the $F_V + F_A$ region of the phase space. However that term actually appears in second order in the formalisms so the determination of the sign of $\gamma \equiv F_A/F_V$ was not possible. There is the additional question of the momentum dependence of the form factor. The literature parameterization is as follows [14]:

$$F_V(q^2) = F_V(0) \cdot (1 + aq^2). \tag{6.8}$$

Where q^2 represents the momentum transfer and is equivalent to $1-x$. The parameter a represents the slope of this dependence and will be fixed for the different analyses to come[6]. Additionally no momentum dependace is given for F_A. The parameter in question is a and it represents the slope in this expansion. For comparison to historical results we varied γ while keeping the value of F_V and a fixed at 0.0259 and 0.041 respectively. Shown below in Figure 6.17 is the χ^2 value for a range of γ.

This figure clearly demonstrates that the proper sign for F_A is the same as for F_V, which is to say, positive. We now focus the region of study and recalculate for a more

---

[6]The previous studies fix the value of F_V and a at different values using the best available at the time. Therefore when presenting results we will adopt the same values as those studies.
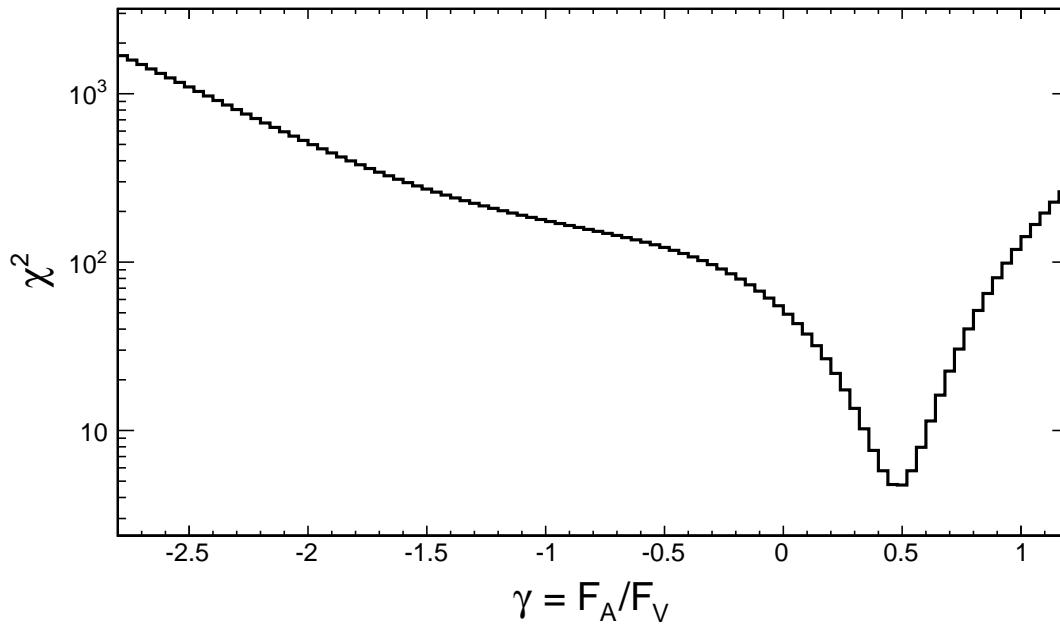
Figure 6.17: Result of the χ^2 test for various values of γ.

refined range. Additionally we note the precision used for binning the decay rate formula was 1,000 bins over the range of x and y from (0,1).

Fitting a quadratic function to the plot in Figure 6.19 produces a minimum χ^2 value for $\gamma = 0.459 \pm 0.057$. The comparison of this result with historical measurement is presented in Figure 6.19. The method for error determination followed the standard procedure of measuring the position of the objective function plus and minus 1 relative to the minimum value [45].

6.4.2 Fixed a

The most recent publication on the topic introduced a new method of evaluating the results [1]. The statistics of that experiment were such that an independent fit of F_V and F_A and a was now possible. In rather exciting fashion those results were presented alongside the traditional γ result and showed great agreement not only between them-
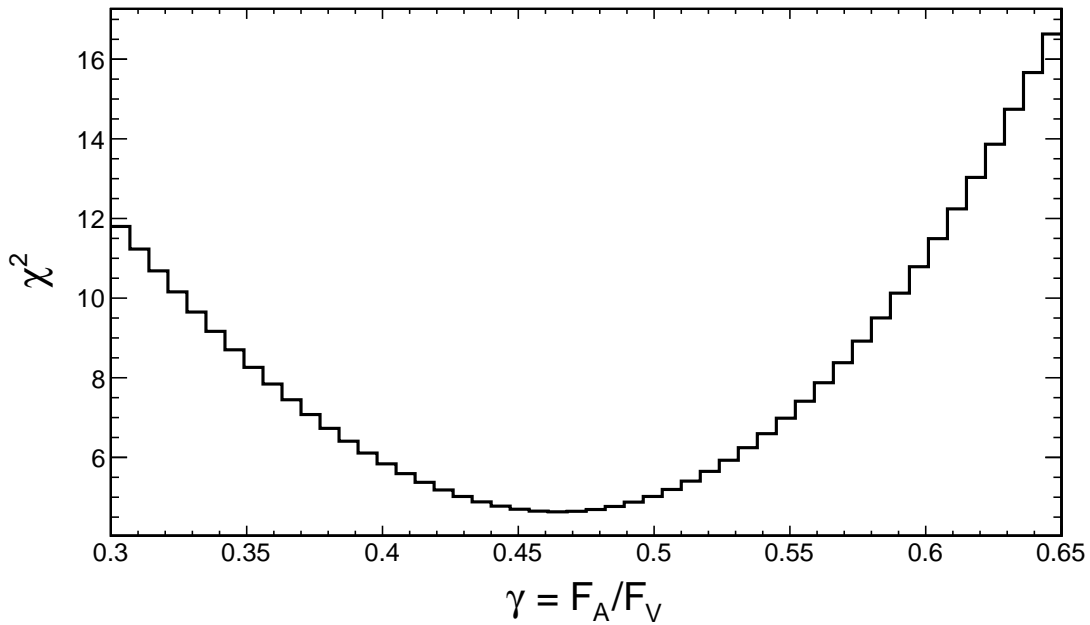
Figure 6.18: Result of the χ^2 test for various values of γ.

selves but also with the CVC hypothesis. Unfortunately the PEN 2008 data set does not provide enough statistics to study the behavior of a[7]. But not wanting to leave the stone unturned we proceeded with a study with a fixed value of $a = 0.1$ as opposed to $a = 0.04$ for the γ test. We then varied both F_V and F_A from (0.005,0.03) individually and the resulting χ^2 distribution is shown in Figure 6.20.

From this figure we see that the results of this analysis are compatible with previous results. From the nature of the decay rate we observe a greater sensitivity to the $F_V + F_A$ combination. The line of constant $F_V + F_A$ is a line with a slope of -1. The $F_V + F_A$ information constrains our fit transverse to that line. The contours of the objective function are therefore narrow in the direction perpendicular to the line of slope -1. Conversely the decay rate makes the $F_V - F_A$ information harder to access. That direction is the line of slope 1. Therefore we see less contraint perpendicular to that

---

[7]Inclusion of the PEN 2009 and 2010 data set should change that.
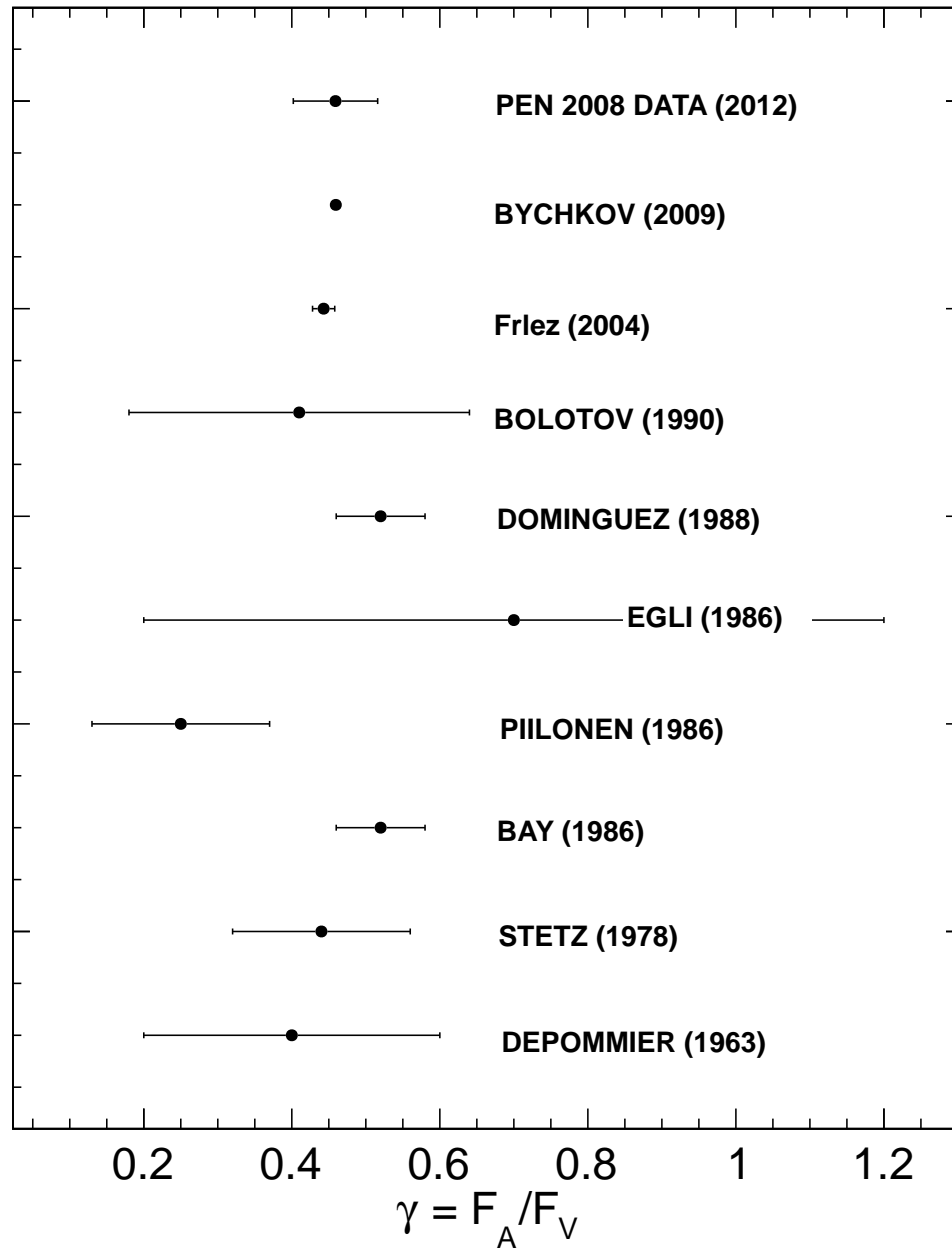
Figure 6.19: Comparison of this result to previous measurements. Citations are listed in order from top measurement to bottom: [1], [2], [3], [4], [5], [6], [7], [8], [9].
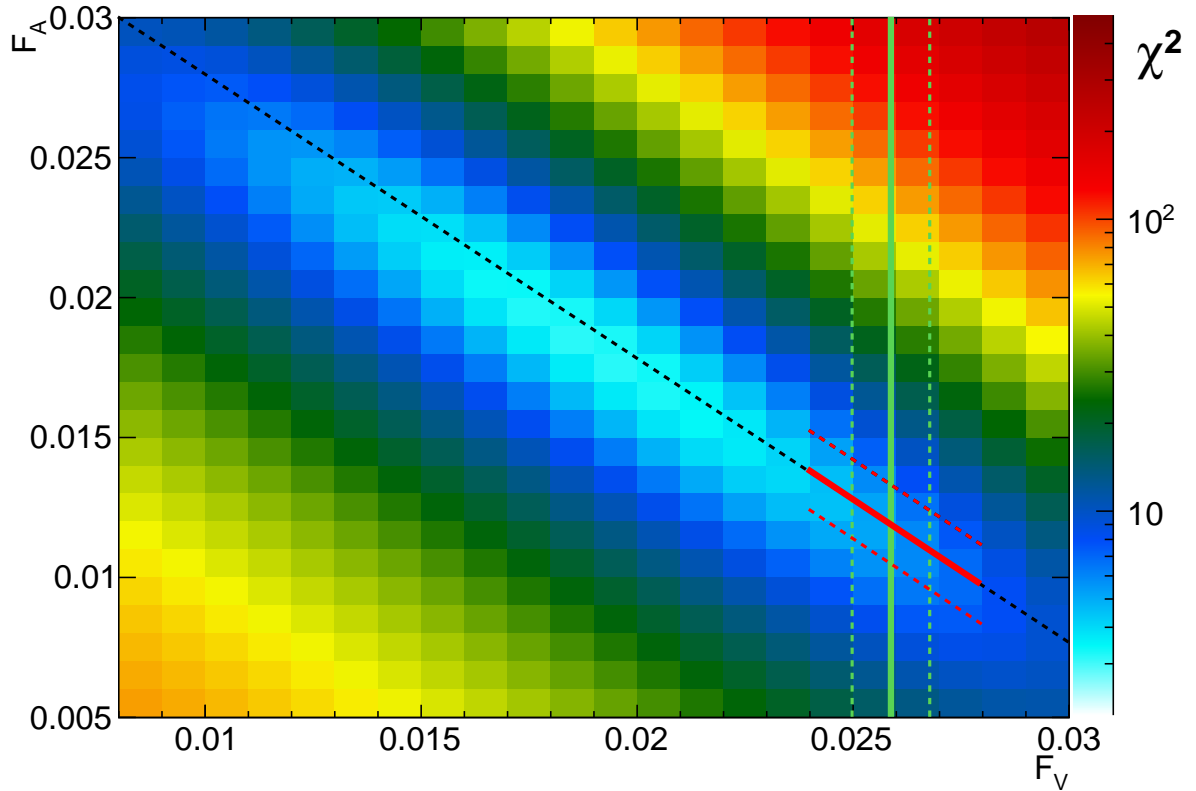
Figure 6.20: This plot shows the χ^2 objective function for ranging combinations of F_V and F_A. The value of a was held fixed at 0.1 for this study. The green line represents the CVC prediction along with its 1σ error band. The red line represents the results of the PIBETA experiment. The black dashed line is an extrapolation of the PIBETA relationship between F_V and F_A.

line. This result is similar to the previous PIBETA conclusion. That work characterized the relationship with the empirical linear dependence of:

$$F_A = (-1.0286F_V + 0.03853) \pm 0.00014. \tag{6.9}$$

That dependence is represented on the plot with a black dashed line. The green line represents the CVC hypothesis[8]. The minimum χ^2 fit yields values of $F_V = 0.0191 \pm 0.008$ and $F_A = 0.0193 \pm 0.008$ for this analysis.

---

[8]The dashed bands represents 1σ errors.

6.5   Error Analysis

To evaluate the quantifiable error in our measurement of F_V and F_A we must trace the uncertainty back from the final parameters used to their source. As such we begin by restating the objective function:

$$\chi^2 = \sum_{i=\text{A,B,C}} \frac{(B_i^{\text{the}} - B_i^{\text{exp}})^2}{\sigma_i^2}.$$

(6.10)

In this equation the very error we are describing is represented by σ_i. Therefore we must give the uncertainty region by region. There are two sources of error in this formalisim: the error in B_i^{the} and B_i^{exp}.

6.5.1   Statistical Uncertainty

B_i^{the}

The determination of the theoretical branching ratio is made by direct numerical integration of the differential decay rate function. As a result the error in the measurement of the branching ratio is just the simple numerical error resulting from the Riemann approximation. Those values are tabulated and presented Table 6.5 and relative summary form in Table 6.8.

Table 6.5: Table of Errors

Source	Region A	Region B	Region C
$B_{\pi \to e\nu_e\gamma}^{\text{the}}$	2.59e-08	1.453e-07	3.80e-07
$\sigma_{B_{\pi \to e\nu_e\gamma}^{\text{the}}}$	1.87e-10	6.13852e-10	1.60558e-09
σ/B	0.072%	0.042%	0.042%

This example is shown for a particular value of the input parameters but is representative of the full search range.

$B_i^{\mathbf{exp}}$

$$B_{\pi \to e \nu_e \gamma} = B_{\pi \to e \nu_e} \left(\frac{N_{\pi \to e \nu_e \gamma}}{A_{\pi \to e \nu_e \gamma}} \right) \left(\frac{A_{\pi \to e \nu_e}}{N_{\pi \to e \nu_e}} \right). \tag{6.11}$$

$B_{\pi \to e \nu_e}$

For this value we simply use the best data available from the Particle Data Group [46]. Therefore we have a value of 1.23e-4 and an uncertainty of 0.004e-4. For a total relative uncertainty of 0.0325%. That of course includes systematic effects as well.

$N_{\pi \to e \nu_e \gamma}$

Here we simply assume that the number of observed events is distributed normally. Thus the calculation of errors is handled in the traditional way by asuming an error proportional to the square root of the number of events.

Table 6.6: Table of Errors

Source	Region A	Region B	Region C
$N_{\pi \to e \nu_e \gamma}$	192.9	272.4	586.2
$\sigma_{N_{\pi \to e \nu_e \gamma}}$	14.0	18.6	32.3
σ/N	7.26%	6.83%	5.51%

From the values given in Table 6.6 it is clear that this measurement will be statistics limited.

$A_{\pi \to e \nu_e \gamma}$

For the determination of the acceptance the statistical error is deduced from the number of simulated events used in the acceptance calculation. Then the error is calculated in the same manner as the number of observed events. It is important to note that these values represent the unweighted statistical error on the acceptance measurement. Therefore the

acceptance numbers shown in Table 6.7 are not the actual acceptance of each region but rather the acceptance for unweighted events.

Table 6.7: Table of Errors

Source	Region A	Region B	Region C
$A_{\pi \to e\nu_e\gamma}$	0.308	0.366	0.381
$\sigma_{A_{\pi \to e\nu_e\gamma}}$	0.0018	0.0017	0.0018
σ/A	0.607%	0.485%	0.479%

$N_{\pi \to e\nu_e}$

For the final presentation of the radiative pion decay branching ratio the result of the PEN experiment main objective will be used for the $\pi \to e\nu_e$ information. For this study a short low precisions estimate was made of the $\pi \to e\nu_e$ signal. The regional dependence is the same because the $\pi \to e\nu_e$ signal is the normalization channel. In this study there were 2.05406 million events observed with an uncertainty of 1.433e3 events and a relative uncertainty of 6.976e−4.

$A_{\pi \to e\nu_e}$

For the statistical part of the acceptance calculation we simply compare the number of thrown simulation events with the number of observed simulation events. In the simulation there were 9.611800 million thrown events and 4.197588 detected events. That corresponds to an error of:

$$\sigma_{A_{pi2e}} = \sqrt{\frac{N_T}{N_T^2} + \frac{N_D}{N_D^2}} = 5.85e - 4, \tag{6.12}$$

or a relative error of 2.55e−4. For these purposes the statistical error on the π_{2e} measurement is negligible. However the systematic discrepancies in this region are not negligible and we will discuss them later on.

6.5.2 Systematic Uncertainty

The main discrimination variable for this analysis the the energy of the positron (y) and photon (x). Therefore most of the systematic uncertainty comes from our ability to accurately measure those quantities. Additionally the simulation of the trigger system is critical for the acceptance calculation. These sources of uncertainly make the largest contribution to the total systematic uncertainty of the experiment. Additionally the measurement of the π_{2e} branching ratio plays a role as well. Once the PEN goal is complete the value used for that branching ratio will be replaced. As such we will not discuss the details of that error here.

For each of the components mentioned we conduct the error analysis in the standard fashion. First we determine the uncertainty in the desired variable at the 1 σ level. Then we modulate the value in the analysis software by that amount. This modulation results in a modulation of the branching ratio equivalent to the 1 σ level. The results of this studies are summarized in Table 6.8.

CsI Calorimeter Energy

The calibration of the CsI calorimeter array was pushed to the limit and the overall uncertainty was on the order of $100\,\mathrm{keV}$. Therefore for the study of the CsI calorimeter systematic uncertainty we varied the values (for the positron and photon) by $\pm\,100\,\mathrm{keV}$. Upon reconstructing the data with the modulated values we observed a shift in the branching ratio of about half a percent. Region by Region details are given in Table 6.8. The effect for the different particles was combined into one overall uncertainty for the calorimeter.

Plastic Hodoscope Energy

The calibration of the plastic hodoscope was conducted taking into account the attenuation length effect. The overall uncertainty was on the order of 10 keV. Therefore for the study of the plastic hodoscope systematic uncertainty we varied the values (for the positron) by ± 10 keV. Upon reconstructing the data with the modulated values we learned that there was insufficient statistics to accurate measure the influence such a small uncertainty would produce. Therefore we neglect this uncertainty in the overall analysis.

Target Energy

The calibration of the target counter positron energy was very challenging. The energy measurement is the final result of several independent detector systems. As a result we were not able to achieve as low a level of uncertainty as the other detectors. The overall uncertainty was on the order of 300 keV. Therefore for the study of the target counter systematic uncertainty we varied the values (for the positron) by ± 300 keV. Upon reconstructing the data with the modulated values we observed a shift in the branching ratio of about one percent. Region by Region details are given in Table 6.8.

Simulation of Trigger

We are still very early in the process of modeling the 2008 PEN experimental trigger. Therefore we experience a rather large error in this kinematic region. The simulated data were processed under a variety of trigger conditions each varying the relevant parameters at the 1σ level. As a result we observed a difference in the acceptance in simulated data as large as about 2% in some regions of study. The details of each region are given in Table 6.8.

6.5.3   Compilation of Errors

All of the errors discussed in the previous sections are summarized in Table 6.8. The values quoted in this table are the relative errors to the branching ratio calculation. The last entry in the table is the value for the relative error in each region used in the objective funtcion (6.10). For this analysis we assume all of the errors in the table are uncorrelated. Having now produced the error estimates for each region of study we may recompute the χ^2 function and recalculate the results of this measurement with proper errors. Those results are presented in the Chapter 7.

Table 6.8: Table of Errors: The first section is the statistical error in the signal channel. The second section is the statistical error in the normalization channel. They are followed by a the total statistical error. The next section shows the systematic errors for the dominant effects, followed by the total systematic error. Finally the total overall error is presented. That total error is used for the denomenator of the objective function. All of the errors listed on this table are relative.

Source	Region A	Region B	Region C
$B_{\pi \to e\nu_e\gamma}^{\text{the}}$	0.00072	0.0042	0.0042
$N_{\pi \to e\nu_e\gamma}$	0.0726	0.0683	0.0551
$A_{\pi \to e\nu_e\gamma}$	0.00607	0.00485	0.00479
$B_{\pi \to e\nu_e}$	0.000325	0.000325	0.000325
$N_{\pi \to e\nu_e}$	0.0007	0.0007	0.0007
$A_{\pi \to e\nu_e}$	0.00025	0.00025	0.00025
σ_{stat}	0.0729	0.0663	0.0555
E_{CsI}	0.00518	0.00376	0.00542
E_{TGT}	0.0156	0.00562	0.0152
$\pi \to e\nu_e$	0.035	0.035	0.035
$\text{SIM}_{\text{trigger}}$	0.013	0.019	0.018
σ_{sys}	0.0408	0.0404	0.0425
σ	0.0835	0.0776	0.0699

Chapter 7

Result and Ramifications of the PEN 2008 Radiative Pion Decay Pilot Analysis

7.1 Synthesis of 2D χ^2 Fit with World Data

Combining the χ^2 minimization routines and the error estimates we present Figure 7.1. This figure beautifully captures the essence of this experiment. The image shows a valley. That valley lies along the line of constant $F_V + F_A$. To deviate from that value, i.e., climb out of the valley, would mean a change in the value $F_V + F_A$. The steeper the cliffs the more certain the measurement of $F_V + F_A$. However one could also walk along this valley. That direction represents changing values of $F_V - F_A$. Unfortunately in that direction there is little resistance. Therefore we interpret these results to represent a good measurement of $F_V + F_A$ but a poor measurement of $F_V - F_A$.

We can also view this valley from above as shown in Figure 7.2. Here we see the minimum of the χ^2 valley represented by an "X". We take that position to be the best
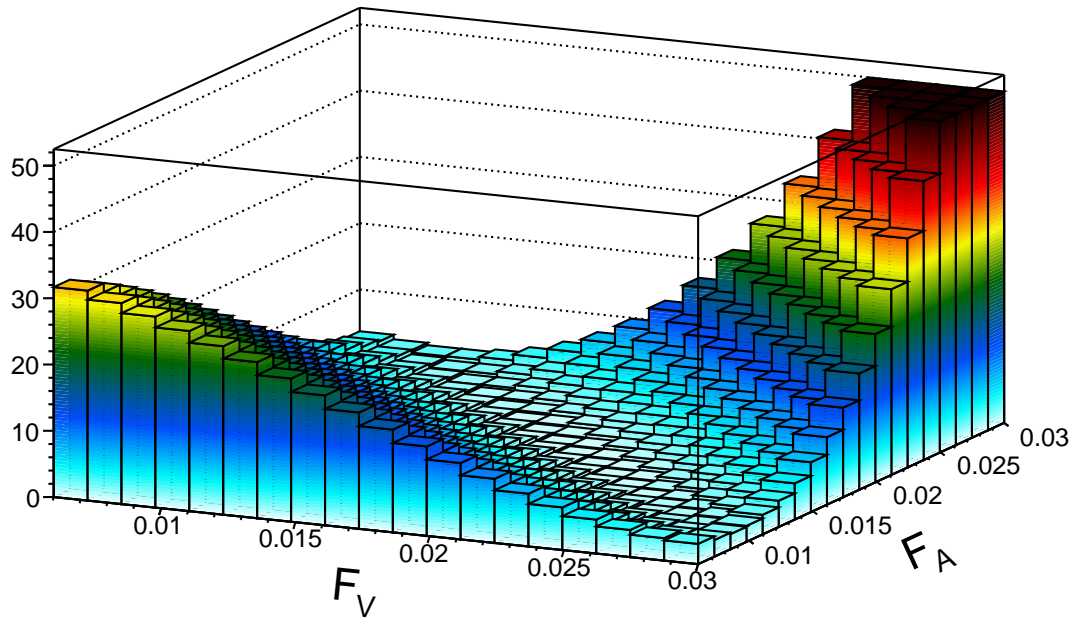
Figure 7.1: The value of the objective fit function is shown in the space of the two model parameters F_V and F_A. The valley lies along the line $F_V + F_A$ with steeply rising walls in the $F_V - F_A$ direction. That represents good confinement of the quantity $F_V + F_A$ but poor confinement of $F_V - F_A$.

estimate of F_V and F_A. Then using the standard technique we have drawn lines showing an increase in the χ^2 function by integers. The first ellipse represents $\chi_0^2 + 1$ and it is from the tangent planes of that ellipse we discern the error on the measurement of F_V and F_A [45] [47] [48]. It is important to understand that the $\chi_0^2 + 1$ ellipse is used to represent the uncertainty on a single paramater for all possibilities of the other parameter. If a simultaneous statement of both parameters is desired then the $\chi_0^2 + 2.3$ ellipse is required.

Figure 7.2 contains several lines showing the current world results. The green line represents the CVC hypothesis for the value of F_V and the dotted lines represent 1σ deviations. The result presented here is good agreement with the CVC value. Additionally there is a red line representing the 1σ ellipse from the PIBETA collaboration[1].

---

[1]This ellipse is very eccentric and the width in the $F_V + F_A$ direction is too narrow to show on this scale.
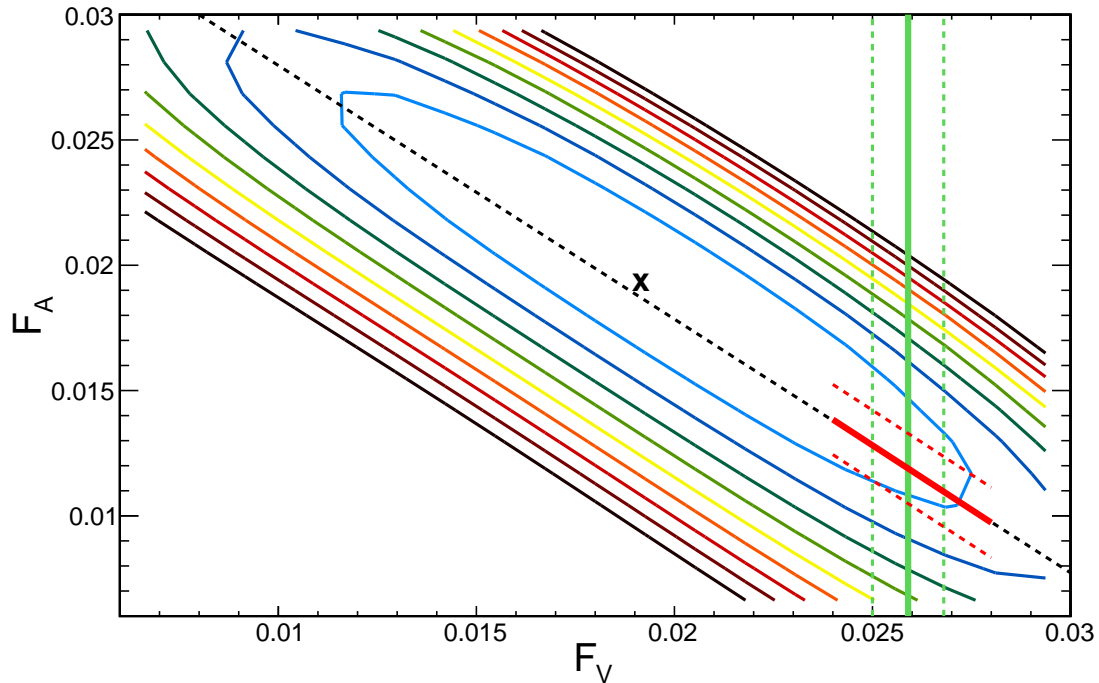
Figure 7.2: This plot represents the results of this dissertation along with current world leading results. The ellipses represent the confidence intervals of the measurement with the first ellipse corresponding to the $\chi_0^2 + 1$ level. Each subsequent ellipse is larger from the previous by a value of 1. The "x" represents the minimum of the objective function. The vertical solid line represents the Conserved Vector Current hypothesis value for F_V and the dashed lines represent the standard error in that determination. Finally the short red line represents the $\chi_0^2 + 1$ ellipse from the PIBETA measurement.

That result was published in 2009 and currently is the most precise measurement [1]. The statistics used for that measurement were an order of magnitude larger than what is contained in the PEN 2008 data set. We hope to be competitive with those statistics once the PEN experiment is fully analyzed. The PIBETA paper also gave a linear relationship between F_V and F_A which has been extended with the black dashed line on Figure 7.2. It is clearly in good agreement with our new result,

$$F_V = 0.0191 \pm 0.008 \qquad F_A = 0.0193 \pm 0.008. \tag{7.1}$$

So far we have seen no deviations from $V - A$ theoretical predictions within this

search. Concidering the possibility of interactions beyond the Standard Model is something we choose not to entertain at this time on account of any result being too speculative given the statistics in the PEN 2008 data set. Therefore we withold comment on that topic until the full PEN data set has been analyzed.

7.2   What's Next

The main limitations of this measurement come from two places. First, the 2008 data taking period was a developmental run for the PEN experiment. The true data production runs were conduced in 2009 and 2010. Once that data becomes available for analysis the statistics available are estimated to increase by at least a factor of five and most likely more. Second, the systematic effects are still in the early stages of analysis. The error budget shows room for improvement on the current systematic uncertainties. Currently, the calibration of the 2009 and 2010 data sets is being finalized. Once that is done the simulation can be further refined and the systematic uncertainties significantly reduced. These two enhancements will greatly improve the result of this analysis.

There are additionally two more pieces of physics that can be attacked. The first is the determination of a, the q^2 dependance of the vector form factor. That study will be possible once the 2009 and 2010 data add to the data set. Currently it was hampered by a lack of statistics but should be no problem to address with more data.

But even with everything listed above we do not show a great improvement over the previous experiment. What does PEN bring to the table that the PIBETA experiment did not? The PIBETA experiment ran with a very large pion stopping rate and therefore a lot of background. However the PEN experiment was quiet by comparison. That reduction in background gives us access to region D. Region D is a new area that includes more of the SD^- term than any other. Recalling from earlier that region of phase

space where SD^- makes the largest contribution is also along the low opening angle line which is also the location of the inner bremstrahlung background. The previous analysis used only the data collected above the Michel positron energy edge. However with our new waveform analysis technique to eliminate $\pi \to \mu e$ contamination and the reduced back ground of the PEN experiment we can push into new and unstudied areas of phase space, region D. The particular region for us will be low energy positrons and intermediate energy photons. This is a very exciting time!

7.3   A Final Thought

Before you can walk you must crawl. Before PEN can explore region D we must be sure of ourselves in regions A, B, and C. The analysis presented in this dissertation shows that we are on track. With an increase in statistics and the better understanding of the systematics of the system we are well on our way to making an important contribution. Region D is right there before us. In the near future we will have explored it and make what we hope is the best measurement of $F_V - F_A$ to date.

Bibliography

[1] M. Bychkov *et al.*, Phys. Rev. Lett. **103**, 051802 (2009).

[2] E. Frlež *et al.*, Phys. Rev. Lett. **93**, 181804 (2004).

[3] V. Bolotov *et al.*, Physics Letters B **243**, 308 (1990).

[4] C. Dominguez and J. Sol, Physics Letters B **208**, 131 (1988).

[5] R. Eichler *et al.*, Physics Letters B **175**, 101 (1986).

[6] L. E. Piilonen *et al.*, Phys. Rev. Lett. **57**, 1402 (1986).

[7] A. Bay *et al.*, Physics Letters B **174**, 445 (1986).

[8] A. Stetz *et al.*, Phys. Rev. Lett. **33**, 1455 (1974).

[9] P. Depommier, J. Heintze, C. Rubbia, and V. Soergel, Physics Letters **7**, 285 (1963).

[10] H. Yukawa, Proceedings of the Physico-Mathematics Society of Japan **17**, 48 (1935).

[11] CERN Courier (1997).

[12] R. E. Marshak and H. A. Bethe, Phys. Rev. **72**, 506 (1947).

[13] R. P. Feynman and M. Gell-Mann, Phys. Rev. **109**, 193 (1958).

[14] D. A. Bryman, P. Depommier, and C. Leroy, Physics Reports **88**, 151 (1982).

[15] D. J. Gross and F. Wilczek, Phys. Rev. D **8**, 3633 (1973).

[16] T. D. Lee and C. N. Yang, Phys. Rev. **104**, 254 (1956).

[17] C. S. Wu, E. Ambler, R. W. Hayward, D. D. Hoppes, and R. P. Hudson, Phys. Rev. **105**, 1413 (1957).

[18] M. Kobayashi and T. Maskawa, Prog.Theor.Phys. **49**, 652 (1973).

[19] N. Cabibbo, Phys. Rev. Lett. **10**, 531 (1963).

[20] E. Neother, Nachr. d. Koenig. Gesellsch. d. Wiss. zu Goettingen , 253 (1918).

[21] M. Finkemeier, Physics Letters B **387**, 391 (1996).

[22] D. P. et al., Physical Review Letters **93**, 181803 (2004).

[23] V. B. et al., (2006).

[24] V. N. Bolotov *et al.*, Physics Letters B **243**, 308 (1990).

[25] L. Michel, Nature **163**, 959 (1949).

[26] A. Einstein, Annalen der Physik **17**.

[27] S. G. Brown and S. A. Bludman, Phys. Rev. **136**, B1160 (1964).

[28] http://www.psi.ch, 2011.

[29] F. Foroughi, (1997).

[30] W. R. Leo, *Techniques for Nuclear and Particle Physics Experiments* (Springer–Verlag, Berlin–Heidelberg–New York, 1994).

[31] M. Bychkov, *title*, PhD thesis, University of Virginia, 2005.

[32] B. VanDevender, *title*, PhD thesis, University of Virginia, 2005.

[33] pen.phys.virginia.edu, 2012.

[34] midas.psi.ch, 2011.

[35] V. Karpukhin *et al.*, Nuclear Instruments and Methods in Physics Research Section A: Accelerators, Spectrometers, Detectors and Associated Equipment **418**, 306 (1998).

[36] E. Mathieson and J. Gordon, Nucl. Instr. Meth. Phys. Res. A **227**, 277 (1994).

[37] S. Agostinelli *et al.*, Nuclear Instruments and Methods in Physics Research Section A: Accelerators, Spectrometers, Detectors and Associated Equipment **506**, 250 (2003).

[38] C. Grab, *unknown*, PhD thesis, unknown, unknown.

[39] V. Kalinnikov *et al.*, Nuclear Instruments and Methods in Physics Research Section A: Accelerators, Spectrometers, Detectors and Associated Equipment **535**, 699 (2004).

[40] A. Palladino, *title*, PhD thesis, University of Virginia, 2012.

[41] Y. K. Lee, L. W. Mo, and C. S. Wu, Phys. Rev. Lett. **10**, 253 (1963).

[42] W. Li, *title*, PhD thesis, University of Virginia, 2004.

[43] E. Frlež *et al.*, Phys. Rev. Lett. **93**, 181804 (2004).

[44] http://anton.phys.virginia.edu/pen_cms/, 2012.

[45] K. N. et al. (Particle Data Group), J. Phys. G **37** (2010).

[46] pdg.lbl.gov, 2011.

[47] W. et. al., *Statistical Methods in Experimental Physics* (Elsevier, 1971).

[48] W. Metzger, *Statistical Methods in Data Analysis* (self published, 1991).